POLITECNICO DI TORINO

Master's Degree in Electronics Engineering

Master's Degree Thesis - July 2024

Neural prosthetics based on microelectrode arrays

Submitted by

Micah Rhea Miriam PINTO

At

ESIEE PARIS

2 Bd Blaise Pascal, 93160 Noisy-le-Grand

Under the Guidance of

Prof. Gaëlle LISSORGUES
Industrial Tutor
Deputy Managing Director
ESIEE Paris
gaelle.lissorgues@esiee.fr

Prof. Lionel ROUSSEAU
Industrial Tutor
Head of Department for MMS
ESIEE Paris
lionel.rousseau@esiee.fr

Prof. Matteo COCUZZA
Academic Tutor
Full Professor - DISAT
Politecnico Di Torino
matteo.cocuzza@polito.it

SUMMARY

This thesis presents a comprehensive analysis of Interdigitated Electrodes (IDEs), focusing on their fabrication, behavior under varying environmental conditions, and the influence of passivation layers on performance and longevity. Interdigitated Electrodes are fabricated using photolithographic techniques in a controlled cleanroom environment, with and without passivation layers such as SU-8, SiO_2, and SI_3N_4 of varying thicknesses. Experimental and simulated analyses are conducted across different mediums, including air and aqueous solutions (DI water, tap water, saline solutions), to assess IDE performance. Impedance data from experiments are utilized to characterize key parameters like geometric capacitance (C_g), double-layer capacitance (C_{dl}), capacitance due to the solution (C_{sol}), and solution resistance (R_{sol}). Theoretical models employing Finite Element Method (FEM) and conformal mapping techniques provide insights into IDE capacitance under ideal conditions, validating experimental findings.

Longevity tests assess IDE performance pre- and post-aging, highlighting significant differences between passivated and non-passivated IDEs. IDEs lacking passivation layers show increased impedance post-aging, indicative of potential corrosion and damage, while passivated IDEs demonstrate reduced impedance, suggesting enhanced stability. The study underscores the critical role of passivation layers—SU-8, silicon dioxide, and silicon nitride—in mitigating environmental degradation and ensuring long-term functionality in biomedical applications.

In conclusion, this research contributes to advancing the understanding of IDE behavior and its packaging(passivation), it's design optimization for improved performance and reliability in biosensing and biomedical device applications. Future directions include refining theoretical models to account for real-world imperfections and further experimental validation in clinical settings.

ACKNOWLEDGEMENTS

I am grateful to **God the Almighty** for all the blessings, and to several individuals whose support and encouragement were essential in completing this thesis.

First, I want to express my heartfelt thanks to **Professor Gaëlle Lissorgues**, my main supervisor. Her kindness, patience, and constant support have been invaluable throughout this journey. Her continuous encouragement and guidance pushed me to strive for my best at every stage. It was impossible to achieve what I did in this thesis without Gaëlle. Gaëlle's insightful feedback and unwavering dedication to my progress provided a solid foundation for my research. She was always available to offer her expertise, whether through detailed discussions or quick clarifications. Her ability to challenge my thinking while offering constructive advice significantly shaped my academic growth. Beyond her role as a supervisor, Gaëlle's empathy and understanding during challenging times were a source of immense comfort. I am profoundly grateful for her mentorship, which has been instrumental not only in the completion of this thesis but also in my development as a professional. Thank you, Gaëlle, for believing in me and for being a constant source of inspiration.

I also want to thank my company co-supervisor, **Professor Lionel Rousseau**. His kindness and patience during our collaboration created a productive and enriching work environment. Lionel's ability to clarify my doubts and provide precise corrections was crucial to my progress. His willingness to engage in thoughtful discussions and address my questions, no matter how complex or simple, demonstrated his commitment to my success. Lionel's supportive and approachable nature made it easy to seek guidance, and his encouragement motivated me to continually improve. I am deeply grateful for Lionel's mentorship and the significant role he played in the completion of this thesis.

A big thanks to **Professor Matteo Cocuzza**, my academic supervisor, for his insightful feedback and constant encouragement. His kind words and constructive insights greatly improved the quality of my work. His commitment to my development was evident through his detailed reviews and thoughtful suggestions.

I also want to thank **Professor Olivier Francais** and **Jordon Roy**, who were always willing to engage in discussions, share ideas, and provide assistance during the course of this thesis. Their collaboration enriched the quality of my research.

I am incredibly grateful to **my parents**, especially my mom, whose prayers and unwavering support have been a source of strength and inspiration. My spouse, **Presley Peter**, I owe immense gratitude. Presley's enduring encouragement, unwavering support, and infinite patience were indispensable. Without him, navigating this thesis would have been far more challenging.

Finally, to everyone who believed in me and supported me in various ways, thank you. Your contributions, no matter how small, made a meaningful impact on this journey.

TABLE OF CONTENTS

LIST OF FIGURES

LIST OF TABLES

ACRONYMS

AC – Alternating Current

AD2 – Analog Discovery2

AFM – Atomic Force Microscopy

Au – Aurum/Gold

BDD – Boron Doped Diamond

BIS – Bio-Electrochemical Impedance Spectroscopy

CF – Carbon Fiber

CM – Conformal Mapping

CNT – Carbon Nanotube

CPE – Constant Phase Element

DC – Direct Current

DI – De-Ionized

EEG – Electroencephalogram

EIS – Electrochemical Impedance Spectroscopy

EM – Electro Magnetic

FEM – Finite Element Method

HPM – High Power Microscope

IDE – Inter Digitated Electrode

IPA – Isopropyl Alcohol

MUT – Material Under Test

PBS – Phosphate-buffered saline

PECVD – Plasma Enhanced Chemical Vapor Deposition

PDMS – Polydimethylsiloxane

Pt – Platinum

PVD – Physical Vapour Deposition

RFID – Radio-frequency identification

Sccm – Standard Cubic Centimeters per Minute

SEM – Scanning Electron Microscopy

Si_3N_4 – Silicon Nitride

SNR – Signal to Noise ratio

SiO_2 – Silicon Dioxide

TiN – Titanium Nitride

Ti/W – Titanium-Tungsten Alloy

UV – Ultra-Violet

Chapter 1
Introduction

1.1. Neural Implants and Prostheses

Neuroprosthetic implants are man-made medical devices or technological systems, that are used to modify neural behavior in neuronal illnesses and restore sensory or motor capabilities following injury [2].They serve as an interface between the human body and the machinery that supports it. By stimulating or recording neurons, they aim to restore brain functioning. When no alternative treatments exist for illnesses like heart failure, deafness, blindness, or complete paralysis, this is an invaluable technical solution for alleviating severe disorders of the nervous system.

The main criteria for all medical prosthetic implants are availability, corrosion resistance, biocompatibility, bio-adhesion, bio functionality. Neural electrodes may be categorized into three types: those that record brain activity, those that stimulate tissue and those that do both. Stimulation electrodes attempt to trigger a functional response from neural tissue by inducing depolarization, whereas recording electrodes aim to produce a low SNR for detecting action potentials and low-frequency activity [3] . An ideal neural implant should minimize the damage to the tissue and perform reliably and accurately for long periods of time [4]. Figure 1.1 illustrates the process for detecting and suppressing seizures utilizing neural interfaces. It has three major components: brain recording, signal processing, and neural stimulation. Electrodes on the scalp capture EEG signals, which are subsequently sent to a signal processor for processing. If the processor recognizes seizure activity, it initiates neural stimulation by delivering electrical impulses to specified brain areas via the electrodes, stopping the aberrant neural activity and preventing the seizure. This continuous cycle ensures constant monitoring and prompt reaction to suspected seizures.

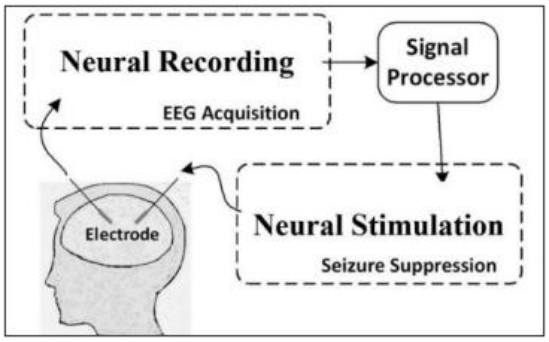

Figure 1.1: Concept of the epileptic seizure detection and suppression using neural recording and stimulation circuits [1].

1.2. Neuronal Communication

Understanding neuronal communication is vital given that it serves as the foundation for neural prostheses, allowing neural activity to be translated into functional commands. A neuron, an individual nerve cell that constitutes the nervous system, enables information to travel throughout the human body. Neurons communicate with each other by transmitting messages throughout our body, driving all our thoughts and actions. They interact with each other using both electrical and chemical signals. Messages begin as electrical signals travelling rapidly down a neuron, known as action potentials. When these signals reach the gap between two neurons, called a synapse, the information is converted into a chemical message to bridge the gap and continue the communication process [5]. The release of these chemical messengers can either trigger an action potential in the neuron on the other side of the synapse, allowing the message to continue, or it can inhibit the message. This process occurs repeatedly, and with continuous activity, the synapse becomes stronger, making it more likely that subsequent messages will be transmitted successfully. In this way, neurons learn to prioritize important messages and disregard less significant ones. This mechanism underlies how our brain learns and adapts to a changing world.

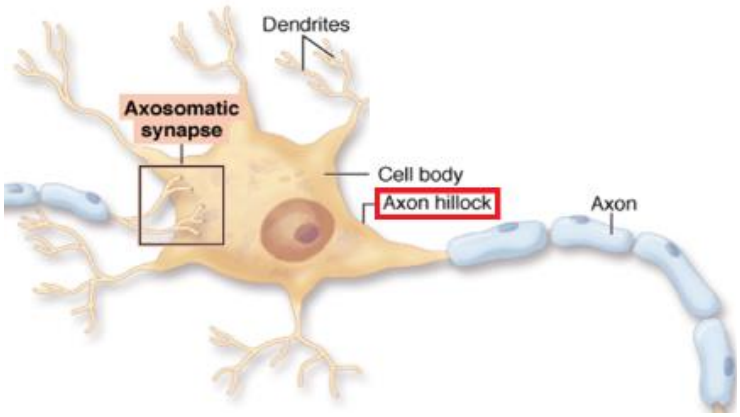

Figure 1.2 : Diagram of a Neuron[6].

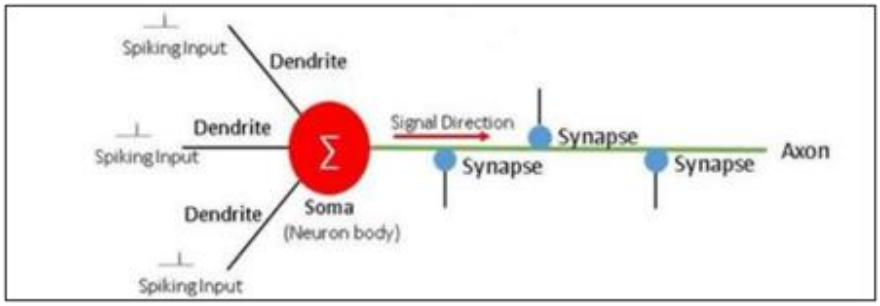

Figure 1.3 : Propagation of a signal in a neuron [7].

The action potential is triggered at the axon hillock that is shown in Figure 1.2, when the membrane potential reaches the threshold of –55 mV as illustrated in Figure 1.4, or higher from its resting potential of –70 mV. At this point, the axon fires, and the action potential travels down the axon. The amplitude reaches approximately +30 mV before re-polarizing. Each action potential lasts about 1-2 milliseconds. **Therefore, a frequency of 1000 Hz is significant because it represents the upper limit of the theoretical maximum firing rate of neurons, given the typical duration of action potentials of 1 millisecond.**

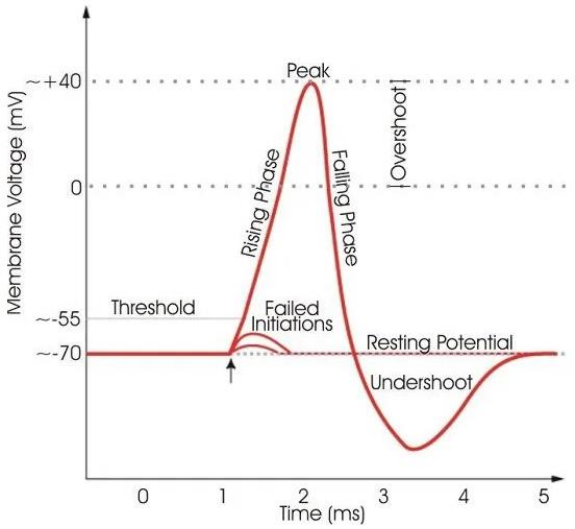

Figure 1.4: The action potential graph [8].

1.3. Project NEURODIAM (2018-2023)

The project NEURODIAM, developed at ESIEE Paris in 2018 sought to create and enhance a full diamond implant at a microscopic level. This involved using conducting Boron Doped Diamond (BDD) with intrinsic polycrystalline Diamond serving as passivation [9][10].Ultimately, this effort resulted in the development of the first ever full diamond implant. The researchers involved in this project focused on enhancing the NEURODIAM initiative, which sought to leverage Electro - Impedance Spectroscopy (EIS) measurements and data collection via wearable RFID technology. Within laboratory settings, they explored sample characterization techniques, with a primary emphasis on the BIS technique. Promising findings emerged with BDD and TiN-Pt-TiN stack models for recording and stimulation applications [11]. Additionally, they formulated an experimental protocol to assess integrity and performance over time, revealing the advantages of intrinsic Diamond over SU-8 passivation layers. These efforts laid the groundwork for both ongoing research and my thesis work.

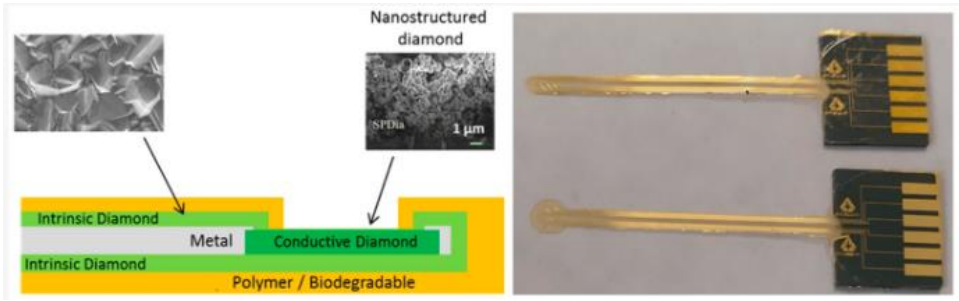

Figure 1.5: (Left)-2-D cross-sectional view of the Full Diamond implant proposed by NEURODIAM , (Right)- Full Diamond Implant [10].

1.4. Research Objective

The research work on the NEURODIAM project has provided a fundamental understanding of the micro implant model under research. A depiction of this model is presented in Figure 1.6. In a typical setup, micro implants consist of three main parts: a conductor responsible for transmitting signals from the implanted site to the electrical/electronic interface, where they can be stored, analyzed, or processed further, particularly for stimulation purposes. To protect this conductor from the harsh internal environment of the human body and to prevent potential data compromise caused by water insertion between the implant layers, a protective structure is crucial. This structure acts as a shield for the entire implant, except for the essential recording components (often called electrodes or openings) and the section that connects with the electrical/electronic interface (referred to as the contact pad). Ideally, all other elements are encased in a biocompatible, non-conductive material known as the passivation layer.

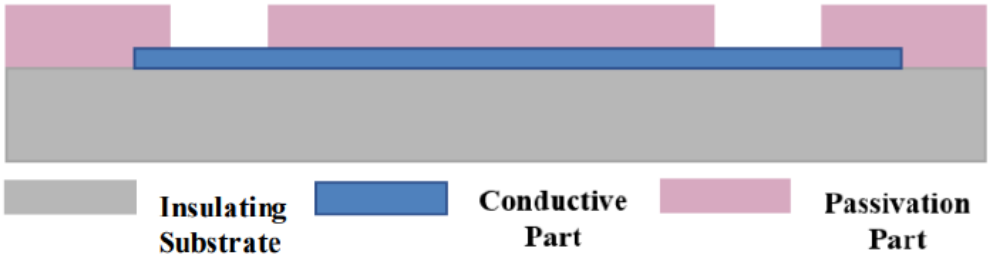

Figure 1.6: Simplified 2-D cross sectional view of an implant [11].

This thesis focuses on understanding the nature and function of conducting materials in this case specifically gold, along with various non-conducting parts also called passivation layers. The aim is to analyze different passivation layers to discern their impact on device behavior and performance. Multiple electrical and electrochemical tests are conducted to gather data for a comprehensive understanding of the device's performance.

Chapter 2
Key Materials & Techniques

2.1 Conducting and Non-Conducting Materials

Over the past forty years, implantable electrodes for neuromodulation have seen significant advancements [12]. The design and manufacture of implantable neural recording electrodes using different materials on a variety of substrates has been the focus of extensive research efforts to date [4]. The non-conductive component, known as the passivation layer or packaging, together with the electrode material, must endure corrosion from repeated electrical stimulation and the extremely wet physiological conditions of their environment. To enhance the quality and long-term stability of electrode implants, it is crucial to carefully design and select the electrodes, as well as the materials used for the substrate and packaging.

2.1.1 Electrode Material (Conducting)

An electrode is considered safe if, upon stimulation, no harmful byproducts emerge from surface reactions or compositional changes. All materials used must be completely harmless, bio-compatible, and irreversible faradic reactions must occur only at concentrations that will not harm the tissue [3], [13]. Electrodes have developed into tiny layers of micro-machined metal foils from large, hand-made pieces of metal that protruded from the skull. The electrodes must be thin enough to be both mechanically stable and flexible after implantation, which adds to the complexity of the situation. Because of this, electrode design is essential, which has resulted in the development of several new materials for electrode fabrication. Material failure in the implant might result in not just electrode breakdown but also breakdown in the packaging [12].

Although silicon-based materials and common metallic materials (like platinum or iridium) and their derivatives (like platinum black and iridium oxide) are widely used in the electrode manufacturing process, their hard, electronic, dry, and static nature opposes the soft, ionic, wet, and dynamic nature of biological tissue. Due to their advantageous features and ease of manufacture, non-conventional conducting materials that were not originally developed for neural implants have drawn a lot of attention. These emerging electrode materials include, for example, graphene, 3D carbon nanostructures, such as carbon fibers (CFs) and carbon nanotubes (CNTs), Glassy Carbon and Diamond [4]. Noble metals such as platinum, gold, and iridium are frequently selected as electrode materials because of their exceptional biocompatibility and strong resistance to corrosion.

For this thesis, gold was chosen as the electrode material due to its exceptional biocompatibility, high conductivity, and long-term stability, despite the growing interest in alternative materials. This decision was based on gold's proven track record in neural implant applications, which provides a balanced combination of essential properties for successful interfacing with biological tissues. In addition to this, it does not cause harmful or poisonous responses when it comes into contact with the skin, tissues, or internal organs when it is implanted into the body. This lowers

the possibility of surgical site infections following implant implantation as well. Gold implants are also malleable, making them an ideal material for manufacturing flexible implants [14]. Because of its numerous advantages, gold has been employed in the fabrication of bio-implants since the 16th century. The abundance of literature supports its status as the best choice for electrode material.

2.1.2 Passivation Material (Non- Conducting)

The past several decades have seen a rise in interest in thin-film electrodes because of their desirable characteristics, which include greater throughput, improved reproducibility, flexibility and stretchability. These thin films, sometimes referred to as a passivation layer, are usually non-conductive coating layers applied to the surface of a structure. They are used to treat or coat a metal surface to reduce its chemical reactivity, making it less susceptible to environmental effects or corrosion and also in order to significantly enhance its electrical properties [15][16]. The biocompatibility of packaging and substrate materials is a requirement for all implanted devices, not only for long-term stability but also for the safety of the user. A long-term in vivo study by Barrese et al. pointed out that the failure of the insulating material is the most important cause of the loss of both signal quality and impedance of implanted electrodes. Because the encapsulating material has a higher surface area than the exposed metal electrode regions, it often fails before the metallization layer [17]. In this thesis, two types of passivation were used over the gold electrode: organic and inorganic passivation.

- **Organic passivation**

  SU-8 : A popular epoxy-based negative photoresist called SU-8 is an organic polymer that is renowned for its high aspect ratio imaging, excellent chemical and temperature resistance, hydrophobic surface following cross-linking, and ease of incorporation into the fabrication process [18]. Its application as a material for substrate and encapsulation of electrode has been widely demonstrated by preliminary research. SU-8 exhibits excellent electrical and mechanical properties, including high isolation, low electrical loss, low Young's modulus, low stress, and biocompatibility [19].

- **Inorganic passivation**

In this thesis, silicon dioxide and silicon nitride are the two inorganic passivation layers employed.

Silicon Dioxide (SiO_2): Silicon dioxide films are typically employed in a variety of semiconductor devices such as intermetallic dielectric layers, gate insulators, and passivation. The substrate/SiO_2 interface quality and the deposition process parameters have a direct impact on the electrical characteristics of the films. In addition to having strong dielectric strength and low electrical conductivity, silicon dioxide is a superb insulator and has exceptional thermal stability. Because of this, it is the perfect material for minimizing leakage currents, lowering parasitic capacitance, and isolating various components inside an integrated circuit [20].

Silicon Nitride (Si_3N_4): With its exceptional mechanical strength, chemical stability, and advantageous electrical qualities including a high dielectric constant, low leakage current, and thermal stability, silicon nitride is a crucial material for passivation layers in semiconductor devices [21].

The materials mentioned above are all excellent for passivation, with the choice ultimately depending on the specific requirements of the device and its operating environment. For neural implants, the chosen material must offer optimal protection and longevity to endure the challenging conditions within the human body.

2.2 Interdigitated Electrode (IDE)

An advanced type of electrode design referred to as an Interdigitated Electrode (IDE) is commonly employed in electrochemical sensors, biosensors, and various analytical and sensing applications. It comprises of two electrodes that each have a number of distinct fingers, or digits, organized in a comb-like structure to create a micro-size gap between them [22]. A conventional IDE is presented in Figure 2.1. Applying a voltage, either AC or DC, to the interdigitated electrode creates an electric field between the digits and the resistance, and current are measurable. This field is higher as the number of fingers increases. The electric field lines generated by the electrodes penetrate the MUI and will change the impedance of the whole structure [23]. The signal acquisition is carried out by measuring changes in impedance and conductivity in the medium of the IDE's. This specific type of electrode was designed to understand and improve the quality of passivation. IDE's can be fabricated using the well-known technique of photolithography, which is discussed in section 3.2.

Figure 2.1:The conventional IDE [22].

The planar interdigital sensors offer several advantages, prominent among them being single-side access to the Material Under Test (MUT). The planar IDE shows the basic properties of two parallel plate capacitors, where the electrodes open to provide one-sided access to the MUT as shown in Figure 2.2. The electric field lines generated by the electrodes penetrate the MUT and will change the impedance of the whole structure. The sets of electrodes behave as a capacitor in which the capacitive reactance becomes a function of system properties [24]. The capacitance per unit length equals the capacitance between two electrode fingers of the IDE.

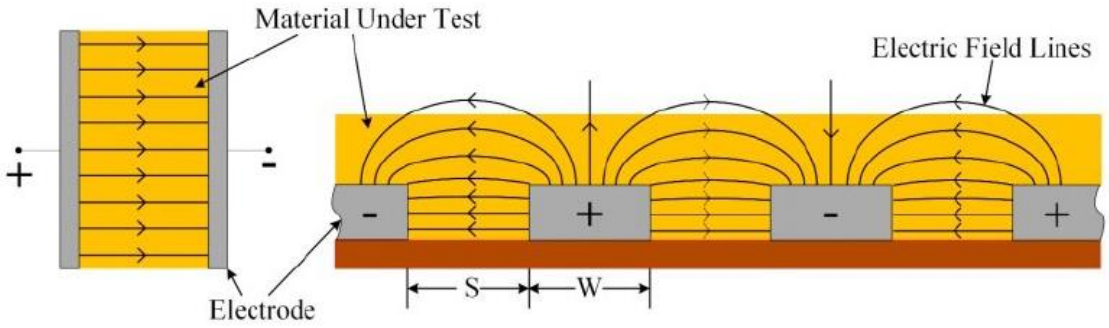

Figure 2.2: (Left)- IDE with a sensing membrane as a parallel plate capacitor.(Right)-Coplanar interdigital sensor [25].

Silver, gold, platinum, and palladium are the most commonly utilized novel metals for electrode materials [26]. For this thesis, as previously discussed in section 2.1.1, gold was utilized as the electrode material. The performance of the electrode material can be evaluated via electrochemical methods, namely, Cyclic Voltammetry, Electrochemical Impedance Spectroscopy, and Nyquist Analysis. Electrochemical measurements can provide information about the behavior and performance of electrode materials such as specific capacitance, phase response, resistance, and so on.

2.3 Electrochemical Impedance Spectroscopy (EIS)

Electrochemical impedance spectroscopy (EIS) is extensively used as a standard approach to analyze electrode/electrolyte interfaces, detecting adsorption processes, formation of surface layers, and so on [27]. Impedance Spectroscopy utilizes three distinct electrical stimuli. First, in transient measurements, a step function of voltage [$V(t) = V0$ for $t > 0$, $V(t) = 0$ for $t < 0$] can be introduced to the system at $t = 0$. The subsequent time-varying current, denoted as i(t), is then observed and measured. Second, A signal v(t) composed of random (white) noise can be applied to the interface, and the resultant current is then measured. In the first two approaches, we obtain time-varying results, generally, the results are Fourier or Laplace transformed into the frequency domain, yielding a frequency-dependent impedance. Third, the most common and standard one, also employed in this thesis, is to measure impedance by applying a single-frequency voltage or current to the interface and then measuring the resulting current's phase shift and amplitude, or its real and imaginary parts at that particular frequency [28]. In sensor applications and generally, the amplitude of this sinusoidal voltage perturbation is typically small. This electrical response is measured and analyzed as electrochemical impedance and is observed while varying the frequency [29]. In other words, Electrochemical impedance can be measured by applying a small AC signal and then measuring the phase shift in the current signal on the applied potential. In a linear system, this current response to a sinusoidal excitation potential will result in a sinusoidal current at the same frequency but shifted in phase as shown in Figure 2.3.

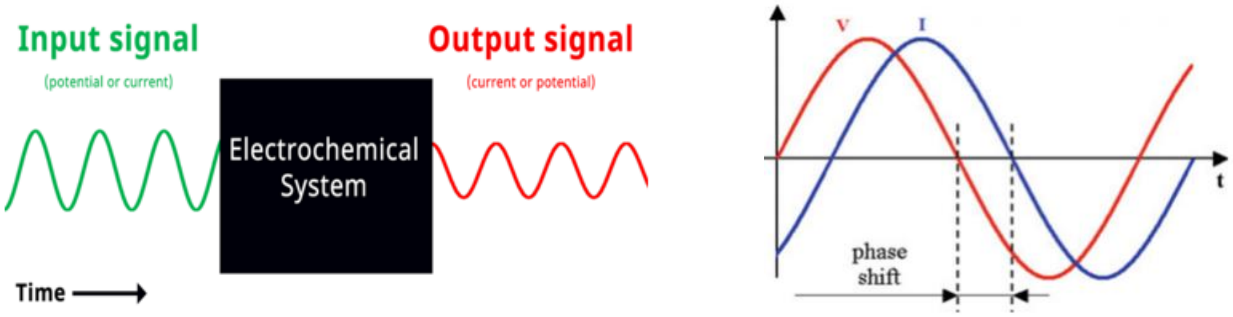

Figure 2.3: (Left Simplified EIS diagram. (Right)- Phase shift in current signal with reference to the applied voltage [30].

The excitation signal has the following form when expressed as a function of time:

$$E_t = E_0 \sin(\omega t) \quad \text{.....(2.1)}$$

Where E_t is the potential at time t, E_0 is the amplitude of this signal and ω is the radial frequency where $\omega = 2\pi f$.

The response signal I_t in a linear system has a different amplitude I_0 and is phase-shifted by ϕ. The phase difference is zero for purely resistive behavior [31].

$$I_t = I_0 \sin(\omega t + \phi) \quad \text{.....(2.2)}$$

To compute impedance, we can utilize a transfer function, which is simply a linear function that calculates the ratio of input potential to output current in the frequency domain. The system's impedance is determined by using this expression that is based on Ohm's law, According to Ohm's law, impedance (Z) is frequency dependent and equal to the complex ratio of the ac voltage (V) over the current (I) [32], which is

$$R = \frac{V}{I} \quad \text{..... (2.3)}$$

Here we replace R(resistance) with Z(impedance) for a system that has an alternating potential system.

$$Z = \frac{E_t}{I_t} = \frac{E_0 \sin(\omega t)}{I_0 \sin(\omega t + \phi)} = Z_0 \frac{\sin(\omega t)}{\sin(\omega t + \phi)} \quad \text{..... (2.4)}$$

Here Z_0 is the magnitude of the impedance that has a phase shift of ϕ. With the help of Euler's relationship (Equation 2.5) it is possible to represent impedance as a complex function; The potential and the current response is as shown in the following equations (Equation 2.6) and (Equation 2.7) respectively.

$$\exp(j\phi) = \cos(\phi) + j \sin(\phi) \quad \text{..... (2.5)}$$

$$E_t = E_0 \exp(j\omega t) \quad \text{..... (2.6)}$$

$$I_t = I_0 \exp(j\omega t + \phi) \text{ …..……..…..} \quad (2.7)$$

While the ratio is easily defined, it is not the typical impedance referenced in IS. Instead, time-varying outcomes are typically transformed into the frequency domain using Fourier or Laplace transformations, resulting in a frequency-dependent impedance. We apply a Fourier transform to our data, converting it from the time domain to the frequency domain. Therefore, the impedance as a complex function will be as follows:

$$Z = \frac{E}{I} = Z_0 \exp(j\phi) = Z_0(\cos(\phi) + j\sin(\phi)) \text{ …..……..…..} \quad (2.8)$$

which can be also written in the form:

$$Z = Z' + Z'' \text{…..……..…..} \quad (2.9)$$

where Z' and Z'' represent the real and imaginary parts of Z respectively. Various approaches exist for presenting impedance data, with two commonly employed methods being the Bode Plot and the Nyquist Plot that is depicted in Figure 2.4. The Bode Plot is obtained by separately plotting the magnitude and phase against frequency. Alternatively, when magnitude and phase data are plotted on Cartesian coordinates (the (x, y) plane), the result is the Nyquist Plot, illustrating Real and Imaginary impedances. Where,

$$Z_x = Z_0 \cos(\phi) \text{ (real)}$$

and

$$Z_y = Z_0 \sin(\phi) \text{ (imaginary)}$$

and the magnitude of impedance Z_0 is the vector sum of the real and imaginary impedances:

$$Z_0 = \sqrt{Z_x^2 + Z_y^2}$$

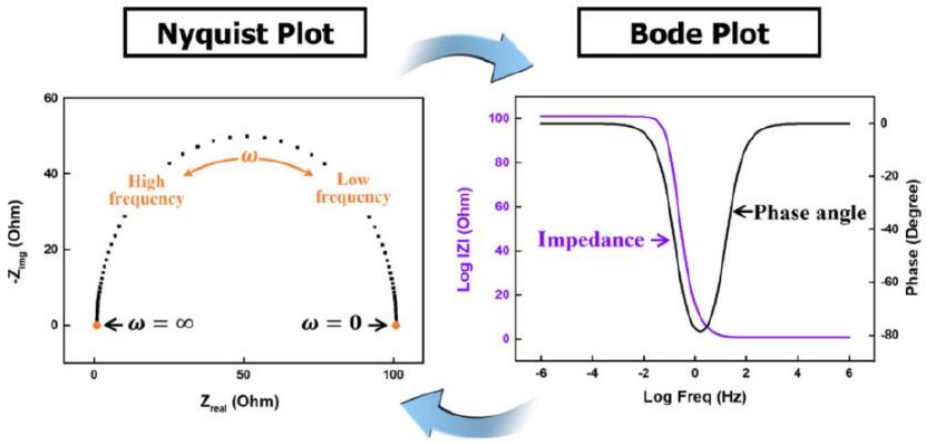

Figure 2. 4: A generic Nyquist Plot and Bode Plot [33].

Throughout this thesis, bode plots are employed to facilitate the assessment of how various circuit parameters influence the frequency response of IDEs.

Chapter 3

Design and Fabrication of Interdigitated Electrode

This chapter presents a comprehensive overview of CLEANROOM fabrication and optimization approaches. The fabrication of the characterized electrodes was done in ESIEE Paris Cleanroom.

3.1 Mask of IDE

The initial phase in the fabrication process is designing the mask. The stencil used to repeatedly generate a desired pattern on resist-coated substrates is called a mask. Transferring the appropriate electrode shape and size from the 2-D design to the substrate is done. For this thesis, the mask designed using CoventorWare 10.4, during prior research, was utilized. The mask was used to fabricate the Interdigitated electrodes with gold as the conductive layer and SU-8/Silicon dioxide/Silicon nitride as the passivation layer. IDEs with varying pairs of fingers were fabricated, i.e., IDE-25, IDE-50 and IDE-100. Figure 3.1 shows a layout of the mask with different pairs of fingers as viewed in KLayout, an open-source layout editor and viewer for electrical designs, including integrated circuits (ICs).

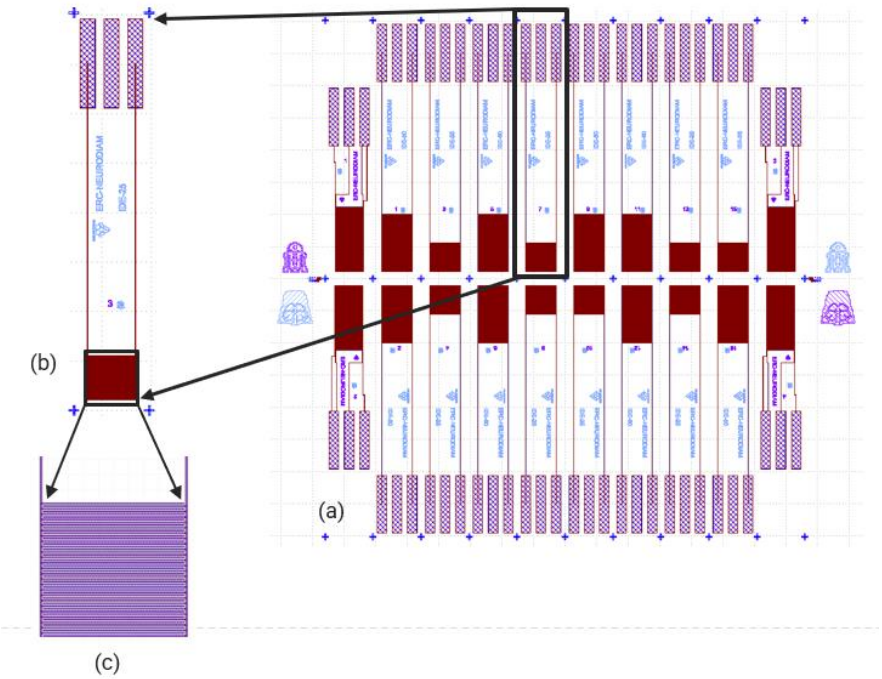

Figure 3.1: (a) The mask designed for fabrication of IDE with different pairs of fingers as viewed in Klayout.(b)Zoomed-in vision of a single strip with 25 pairs of fingers.(c) Zoomed-in view of the finger-like structures.

The mask specifies the exact dimensions and geometric patterns for the IDE. The measurements include the overall dimensions of the IDE array, the width and length of each electrode finger, and

the distance between adjacent fingers. To achieve optimal performance, the mask makes sure that each electrode finger is precisely positioned and equally spaced.
Using the mask illustrated in Figure 3.1, the IDE was fabricated with the following specific dimensions:

- Electrode Finger Length: 4724µm
- Electrode Finger Width: 30µm
- Spacing Between Fingers: 60µm

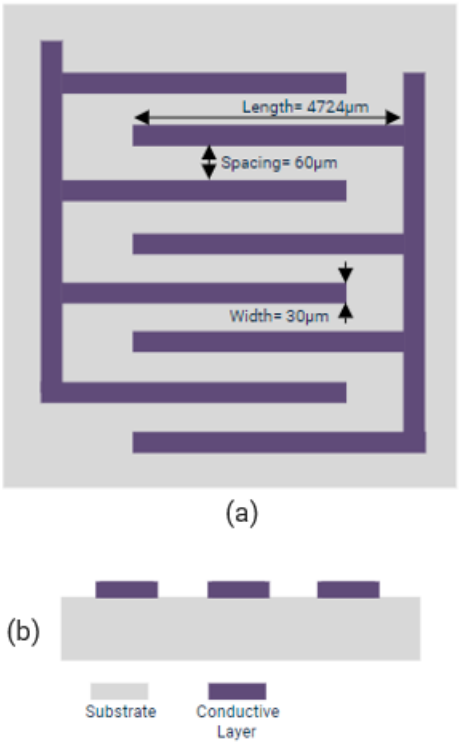

Figure 3.2:(a) Top view depicting the dimensions of the IDE with respect to the mask used. (b) 2D- cross sectional view of the IDE without passivation layer.

Three types of Interdigitated Electrodes (IDEs) were fabricated to investigate different passivation strategies and their effects on performance:

- **IDE without Passivation:** The first type of IDE was fabricated without any passivation layer, leaving the electrodes exposed to directly interact with the surrounding environment.

- **IDE with Full Passivation:** For the second type, a passivation layer (here, inorganic passivation) was applied over the entire surface of the IDE, covering both the electrodes and the spaces between them. This complete coverage aims to protect the electrodes from environmental factors, such as moisture and contaminants, though it might influence the IDE's sensitivity and performance characteristics.

- **IDE with Selective Passivation:** The third type featured a selective passivation layer (here, organic passivation), with the material deposited only on top of the electrodes while leaving the spaces between them unpassivated. This selective approach is designed to mitigate the effect of water retention while maintaining protection for the electrodes. By leaving the spaces unpassivated, the IDE can potentially achieve better performance in humid environments by reducing the impact of moisture accumulation.

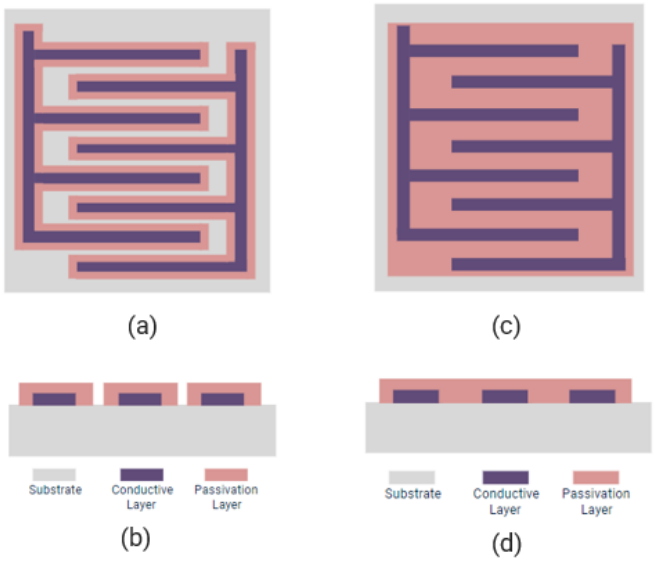

Figure 3.3:(a),(c)- 2D representation of the top view of the IDE with passivation layer.(b),(d)- 2D cross-sectional view of an IDE with passivation layer. In (a),(b)- The passivation is deposited only on top of the electrodes leaving spaces to avoid the effect of water retention.

3.2 Microfabrication Process

The manufacturing process of the chosen electrode material must be reproducible, scalable, and have a high resolution. Interdigitated electrodes were patterned on 4-inch glass substrates using photolithography and metal deposition techniques. We start with glass wafers that have a P-type <111> orientation. The substrate material used as the device's base must be biocompatible, biostable, chemically inert, have suitable dielectric qualities, provide mechanical integrity, and adhere to the metal electrodes. Glass is a good electrical insulator with a relative permittivity of 4 [34].

1. **Deposition of Adhesion Layer + Gold:**
Sputtering, a PVD process, was conducted to deposit gold (Au). A Ti/W adhesive layer was used to enhance the adhesion between the substrate and the gold layer, preventing separation or delamination. The reactor's pressure was maintained at 1.05e-2 hPa, with argon gas introduced at a flow rate of 80 sccm (standard cubic centimeters per minute). After stabilizing the plasma, the DC supply was activated and set to 202W and 414V to maintain the plasma in the chamber. Initially, a 20 nm thick Ti/W adhesion layer was deposited over 20 seconds,

followed by a 500 nm thick gold (Au) layer deposited over 5 minutes. This concludes the PVD process.

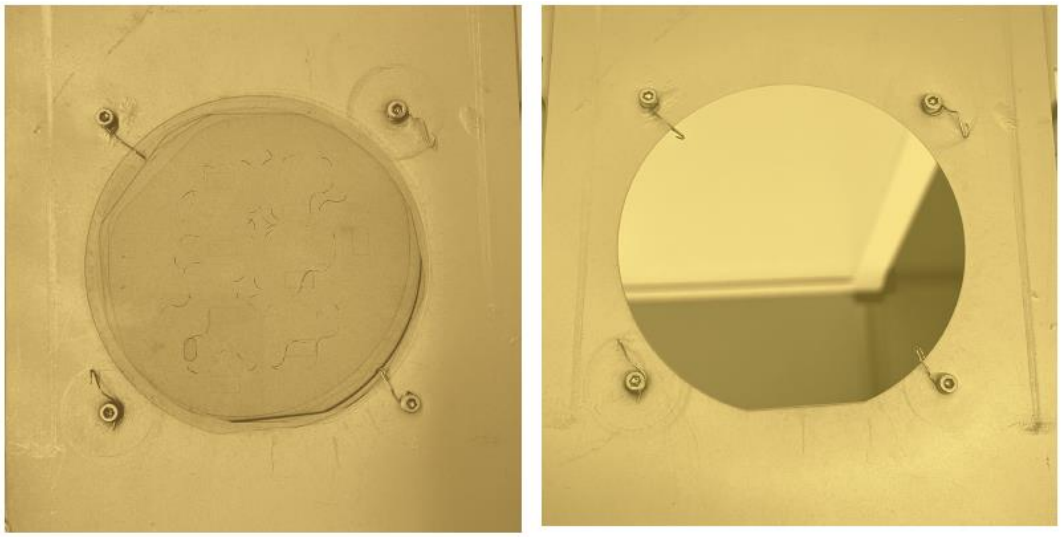

Figure 3.4: (Left)-Before,(Right)-After Sputtering Ti/W + Gold on the Glass Substrate.

2. **Deposition of Photoresist:**
   The photoresist was deposited by spin coating. PFR7790- a negative photoresist was spun onto the wafer to create a thin layer, targeted to be ideally 1 µm thick, achieving a thickness of 1.1 µm in this case. The photoresist was spun for 30 seconds at a speed of 3125 rpm with an acceleration of 500 m/s2. Following this, the wafer was cleaned using acetone.

3. **Soft Bake:**
   The soft bake process is done in order to dry the substrate surface, partially harden the photoresist (PR) layer, and remove excess solvent from the wafer. This is achieved by heating the wafer to approximately 110°C for three minutes.

4. **Exposure:**
   The mask, designed as detailed in section 3.1, was manufactured and imprinted onto an industrial chrome mask. This mask was placed in direct contact with the coated photoresist to transfer the IDE pattern onto the sample's surface. UV light from a mercury lamp was used to expose the photoresist through the mask, transferring the pattern onto the photoresist layer. The exposure time was set to approximately 3.65 minutes, with a separation distance of about 50 µm.

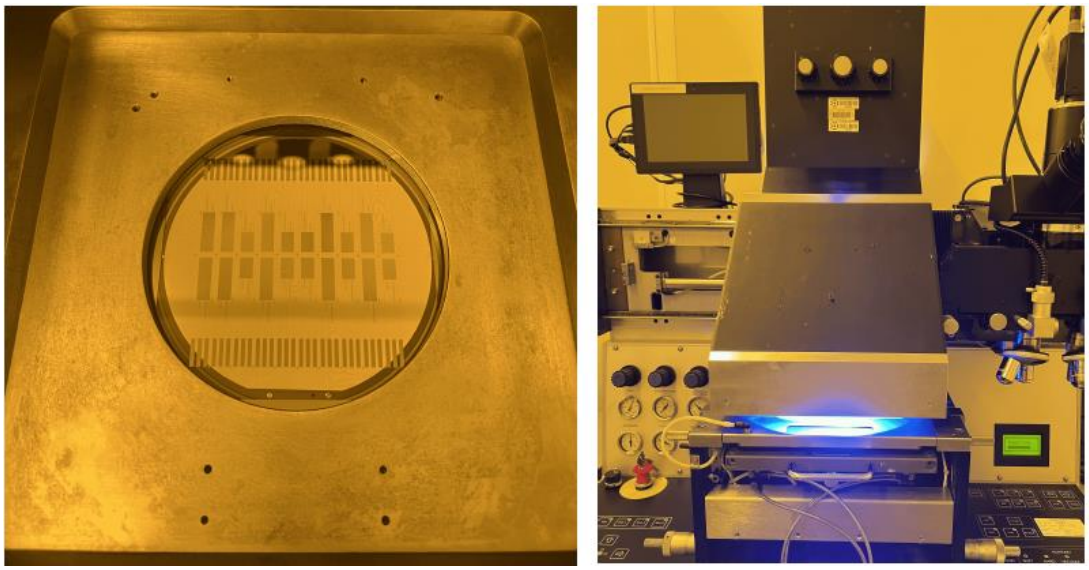

Figure 3.5 : Exposure :(Left)-Substrate aligned to the mask before exposure. (Right)-Exposure to UV light.

5. Development of photoresist:

The wafer was then dipped in PRD238 developer, a solution specifically for developing photoresist, for 45 seconds. This process dissolved the exposed areas of the photoresist. Consequently, the photoresist that was not exposed to UV light was dissolved. Following development, the wafer was rinsed with DI water and cleaned by blowing the wafer surface with a nitrogen gun.

6. Hard Bake:

This step is performed to remove excess moisture and enhance adhesion between the gold layer and the photoresist. The wafers are heated to 110°C for 3 minutes in this subsequent stage. Following this, the wafer undergoes inspection using a high-power microscope (HPM) to assess the clarity and distinctiveness of the pattern.

7. Etching and removal of photoresist:

Wet etching is employed in this process. First, gold is etched, followed by the etching of Ti/W using ACI2 etchant. Subsequently, the remaining photoresist is removed using acetone. The result is an IDE structure featuring a micro-gap gold contact electrode.

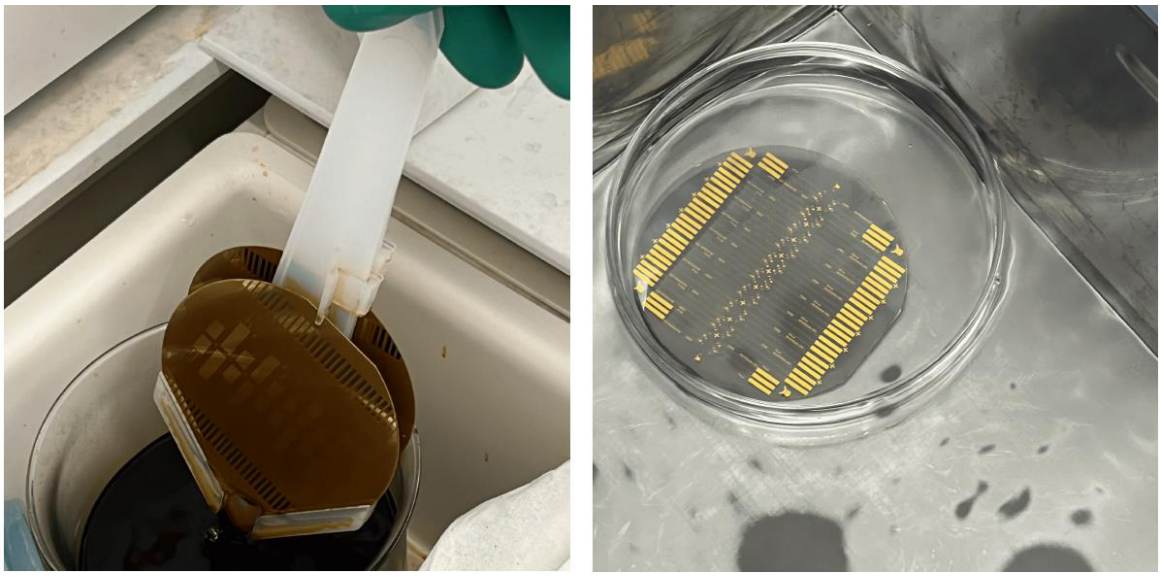

Figure 3.6: Wet Etching process: (Left)-Removal of Gold. (Right)-Removal of Ti/W.

8. Measuring the thickness :

Following etching, we measured the thickness of the wafer, including glass, Au, and Ti/W, using profilometer software called "Vision 64". The measured thickness ranged between 545-565 nm, which meets our application requirements as thickness is not the primary consideration.

9. Hard Bake :

Heat the wafers to 110°C for 5 minutes to eliminate any residual water or solvent.

10. Deposition of Passivation Layer

a) Deposition of Photoresist-SU8 :

A passivation layer of SU-8 photoresist was deposited on the gold surface, with a targeted thickness of 2 µm. The photoresist was spin-coated at 2000 rpm for 30 seconds and underwent a Soft Bake process. This process included heating the wafer to 65°C for 2 minutes, ramping up to 95°C over 2 minutes, and then returning to 65°C for 1 minute. The mask was then used to expose the photoresist-coated wafer to UV light for approximately 32 seconds. Post-exposure bake involved controlled heating to facilitate chemical reactions, following a similar temperature profile as the Soft Bake. The developed wafer was immersed in SU-8 developer for 2 minutes, rinsed in isopropyl alcohol for 1 minute, water for 3 minutes, and cleaned with a nitrogen gun. The passivation layer allowed for inspection using a high-power microscope to verify pattern clarity.

b) Deposition of Silicon Nitride / Silicon Dioxide:

On different substrates that had been prepared, silicon dioxide (SiO_2) and silicon nitride (Si_3N_4) were deposited using a technique called plasma enhanced chemical vapor deposition, or PECVD. The thickness of the deposited passivation layers were 500 nm and 1 um. The chamber was stabilized at 300°C and 1.07 Torr of pressure prior to deposition. RF energy at 13.56 MHz was used to generate plasma, which then reacted with precursor

gases to form the desired thin films on the heated substrates. Specific gas mixtures, also called precursors, were used in the deposition of Si_3N_4 and SiO_2. The resulting film thickness was directly proportional to the deposition time. Following deposition, the substrates underwent a purging step to remove residual gases and contaminants.

After deposition, a positive photoresist was spin-coated onto the wafers and subsequently soft-baked. Precise alignment was performed to ensure the formation of a desired pattern on the photoresist. The photoresist was then patterned using a combination of light exposure and a developer solution. Finally, the substrates were subjected to dry etching with plasma to remove material in the desired regions, creating the final patterned structures.

11. Measuring the thickness:

After the deposition of the passivation layer over the electrode, we measured the thickness of the wafer constituting of passivation layer, Gold, adhesion layer and substrate using a profilometer software-Vision 64 and an Ellipsometer, which gives us a measure of thickness and refractive index. The thickness that we found was somewhere around 2.17µm for SU-8 passivation and about 1.1µm and 520nm for Si_3N_4/SiO_2. We also measured the thickness of the contact pad which is made of only gold substrate and Ti/W, which was about 0.6µm. The wafers are then diced, and its individual electrodes separated. After this, the electrodes were cleaned in Acetone for about 2mins and then cleaned in IPA and dried.

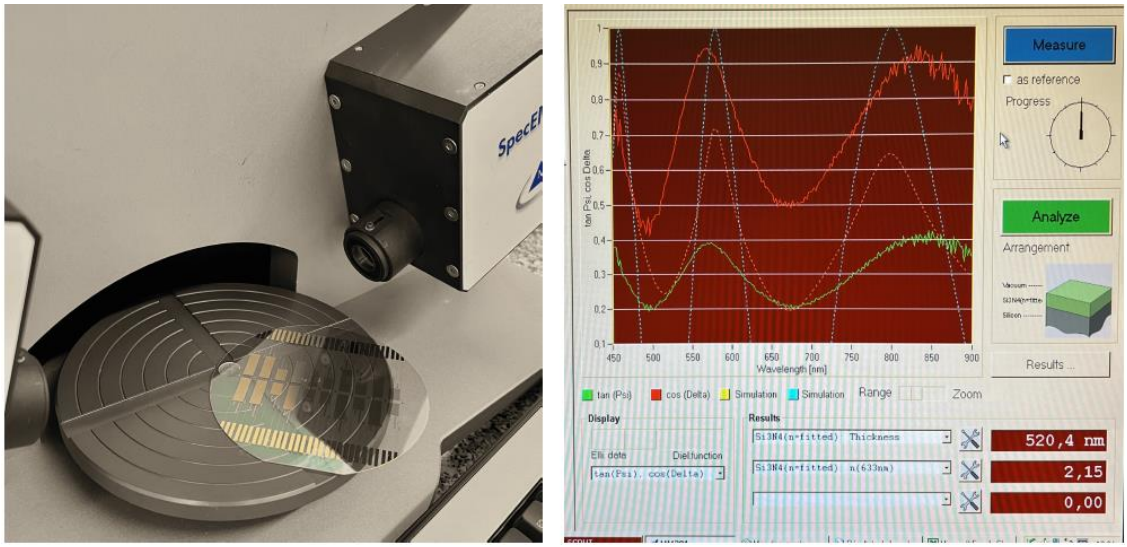

Figure 3.7: (Left)-Measuring the thickness of the fabricated electrode. (Right)- Output from the Ellipsometer.

The results of the fabrication process as shown in Figure 3.8 yielded various samples designated as IDE-25, IDE-50, and IDE-100, each with different passivation layers and thicknesses. These included samples without any passivation layer, samples with a 2 µm thick SU-8 passivation layer, and samples with Silicon Nitride passivation layers of 1 µm and 500 nm. Additionally, samples were fabricated with Silicon Dioxide passivation layers of 1 µm and 500 nm. These samples were checked for defects and then subjected to impedance analysis using the HP 4194A impedance analyzer, which is discussed in the next chapter, section 4.2.

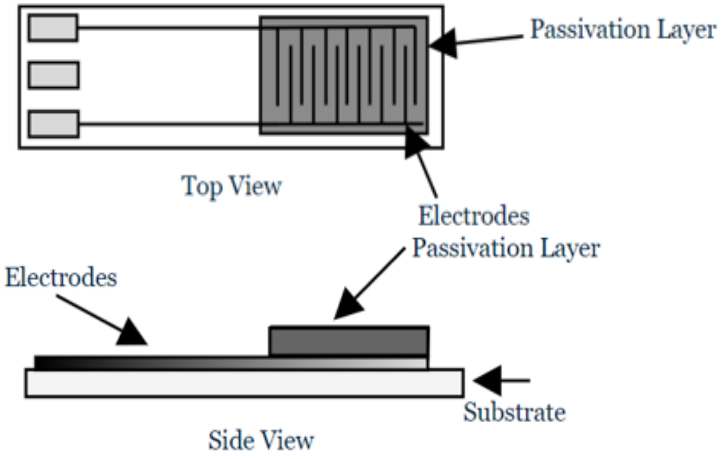

Figure 3.8: Top and Side view of the fabricated Interdigitated Electrode.

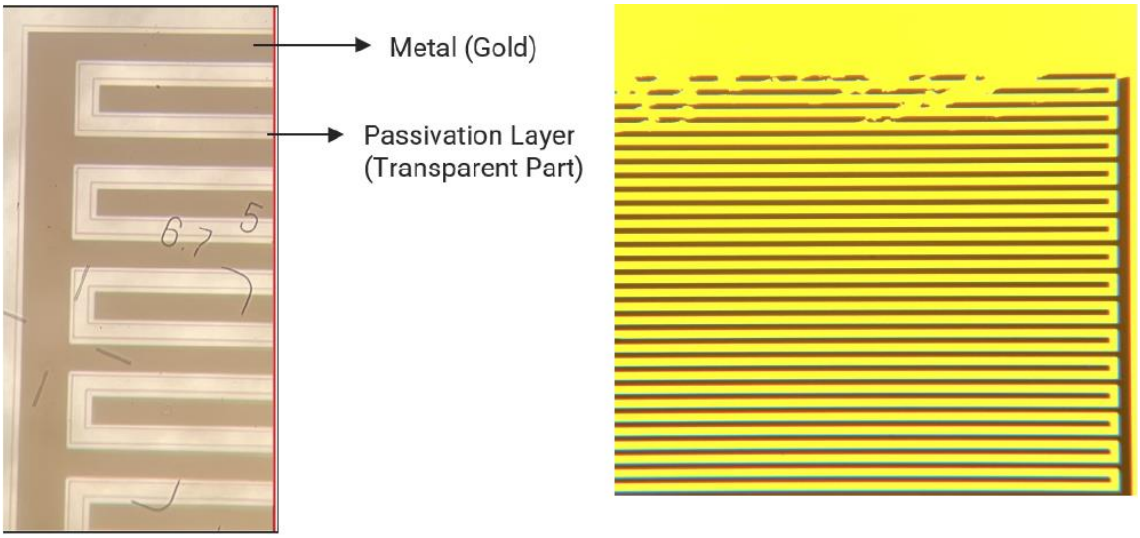

Figure 3.9: (Left)-: Microscopic view of gold covered with passivation (Right)- Defected sample as seen under the EVOS microscope.

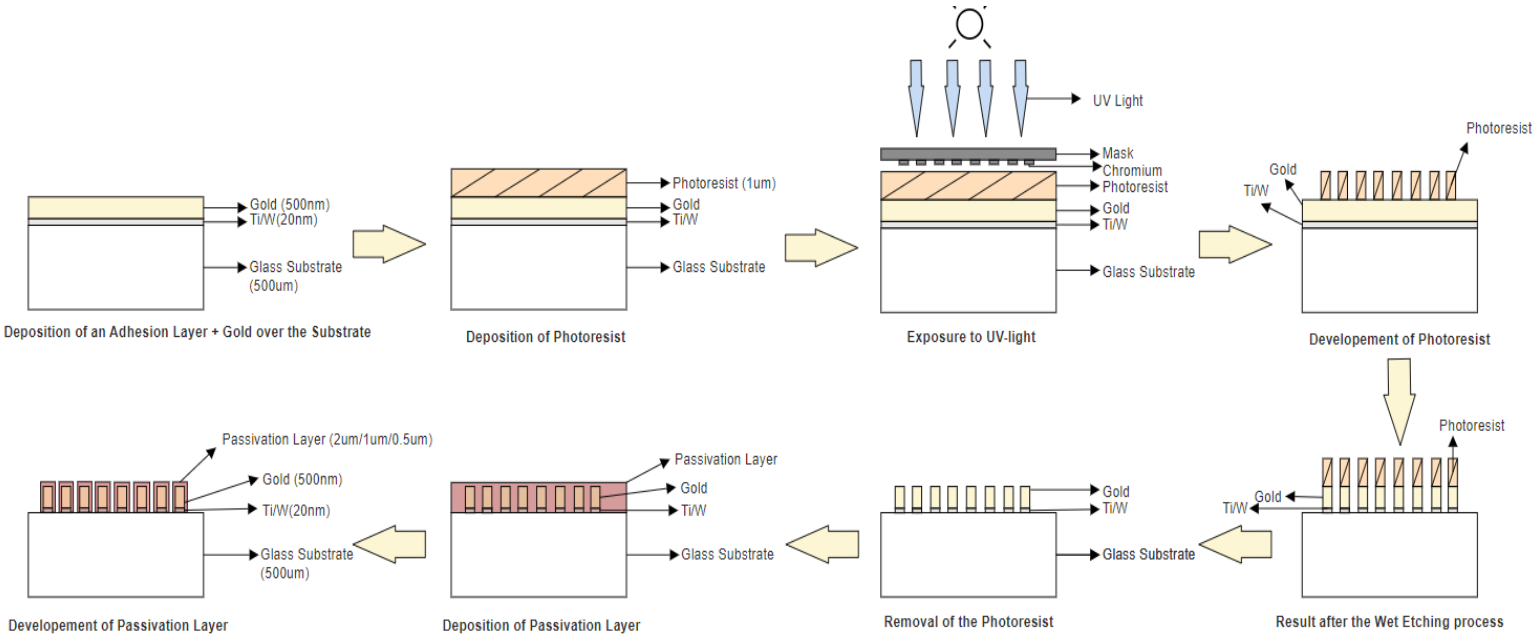

Figure 3.10: Microfabrication process for fabrication of IDE.

Chapter 4

Simulation, Analysis and Comparative Study of IDEs

4.1 FEM design and simulation

The primary objective of utilizing COMSOL Multiphysics simulation software is to simulate the impedance of Interdigitated Electrodes in various mediums. This simulation is crucial for validating and ensuring the accuracy of experimental results obtained using the impedance analyzer HP 4194A. By accurately modeling the impedance of IDEs in different environments, researchers can compare the simulated data with experimental measurements to confirm their reliability and precision. COMSOL Multiphysics provides a complete framework for modeling and simulating complex interactions inside IDE structures. This includes the medium, electrode shape, frequency range, and other factors influencing impedance. The software's Multiphysics features allow for the integration of electrical, electrochemical, and mechanical processes, resulting in a full and comprehensive knowledge of the system being studied. Simulating impedance with COMSOL can help in detecting and limiting potential sources of inaccuracy in experimental settings. By comparing simulation findings to experimental data, differences may be identified and remedied, resulting in more precise and reliable measurements. This procedure not only confirms the experimental data, but also improves our general knowledge of the system's behavior.

4.1.1 Simulation Setup and Parameters

COMSOL Multiphysics is a finite element analysis program that provides geometric meshing, modeling, designing, simulating, and analysis capabilities. It is utilized to simulate the IDE. In this section, we model and simulate the structure of an IDE, along with its geometrical parameters, using finite element simulations in COMSOL Multiphysics. The comprehensive process of modeling using COMSOL software is outlined in the appendix.
We have three kinds of IDE based on the number of pairs of fingers, IDE-25, IDE-50 and IDE-100. The major goal here is to design the IDEs with and without a passivation layer, examine the relationship between parameters and performance and ensure the accuracy of experimental results obtained using the impedance analyzer HP 4194A.

The IDE 2D layout is first sketched with its dimensions and then modeled and simulated using the software. To model the IDE, we consider a cross-sectional area (A-A') that symmetrically divides the IDE structure at its center, as illustrated in Figure 4.1. To simplify the model, we represent it with two electrodes (refer Figure 4.2). To extrapolate the impedance (as observed in the Bode plot) to all fingers, we divide the impedance by the number of fingers minus one (N-1), assuming they function as resistors connected in parallel. In Figure 4.2, we present the model to be simulated in COMSOL, using appropriate dimensions that reference the actual mask dimensions detailed in Figure 3.2.

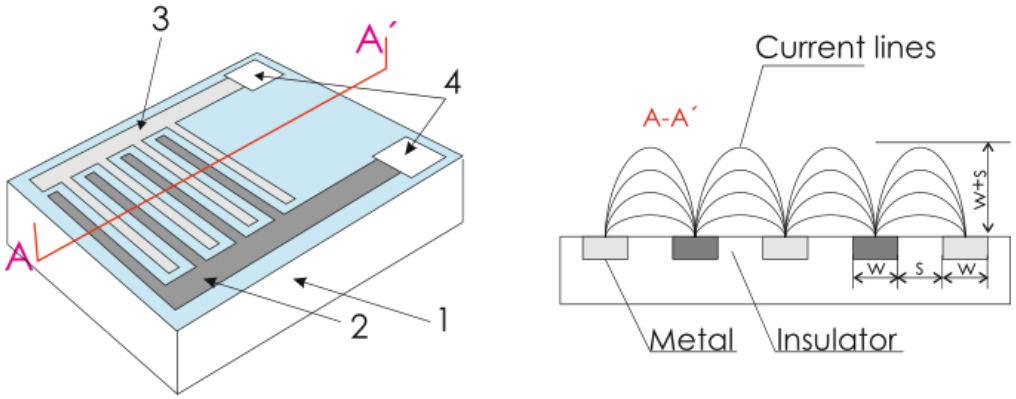

Figure 4.1: Planar interdigitated electrode array (IDEA) device and its cross-section. 1 – insulating substrate; 2, 3 – electrodes collector bars; 4 – contact pads, w – electrode digit width, s – separation between the digits and w + s – depth of the electric current penetration [35].

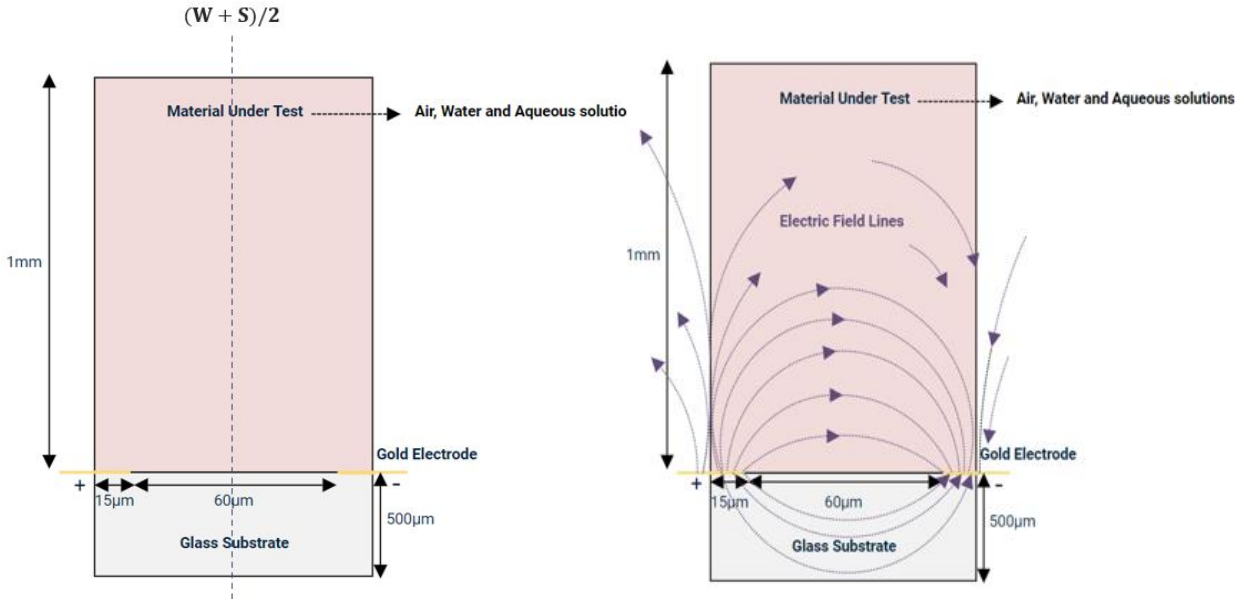

Figure 4.2: (Left)- Model simulated using COMSOL. (Right)- Electric field lines penetrating the MUT.

COMSOL Multiphysics is a simulation software that lets one virtually test and explore different physical systems. Whether it's electrical circuits, heat transfer, fluid flow, or structural mechanics, COMSOL allows one to create computer models to mimic real-world situations. Here, IDEs with and without passivation are modeled in various media (MUT), one at a time. The media used includes air, DI water, tap water, PBS 0.01M and low and high concentrations of saltwater. The freedom of constraints we have is in relative permittivity (ϵ_r) and electric conductivity (σ), derived from the analysis presented in literature review papers. The strength of electric field is generated using Electrostatics study under the AC/DC module of COMSOL for IDE simulation. Simulations were performed to demonstrate how electrical screening develops over time for IDEs in a medium, as well as the electric field between individual digits of electrodes. As previously stated, the

freedom of constraints we have is in relative permittivity (ϵr) and electric conductivity (σ) which are discussed here. The relative permittivity and conductivity of air and aqueous mediums are presented in Table 4.1.

- **Varying the Relative permittivity (ϵr) :** The value of the total impedance due to the MUT can be evaluated using the following equation

$$Z = \frac{1}{C_\omega} = \frac{d}{\varepsilon_r \varepsilon_0 A \omega} \quad \text{.....(4.1)}$$

Any changes in ϵr affects capacitance, which, in turn, influences impedance. That is, higher the ϵr value, lower the impedance and lower the ϵr value implies higher the impedance.

- **Varying the Electric conductivity (σ)** : When considering water as the medium, both Di-water and Tap water are examined. Di-water has lower conductivity and hence we see more resistive behavior in the magnitude plot, This can also be known from the equations 4.2 and 4.3 :

$$R = \frac{\rho l}{A} \quad \text{.....(4.2)}$$

$$\rho = \frac{1}{\sigma} \quad \text{.....(4.3)}$$

When the conductivity is high like in tap water, The resistivity of the system decreases significantly. This is also reflected in the phase plot; we expect a curve at the same frequency where there is a variation due to the conductivity of the medium.

Material	ε_r	σ[S/m]
Air	1	0.0000012μ
DI Water	80	0.055μ
Tap water	80	50μ
Low Saltwater Conc.	69	250μ
High Saltwater Conc.	45	50000μ
PBS 0.01M	80	1.5
SU-8	4	0
Si_3N_4	7.5	0.000001μ
SiO_2	4.5	0.0000000007μ
Diamond	5.7	0.16μ
Glass	4	0.00000001μ

Table 4.1: Relative permittivity and conductivity of materials used in COMSOL.

Table 4.2 presents another vital parameter, the knee point or relaxation frequency denoted by f_c , which is calculated using the formula in equation 4.4. This frequency is crucial as it indicates the point where the material's behavior changes, i.e., from being resistive to capacitive. It is directly proportional to the conductivity and hence we notice for materials with higher conductivities,

clearly the f_c falls in the higher end of the frequency spectrum. As shown in Table 4.2, the f_c of materials such as air, DI water, and PBS solution occur at frequencies outside our frequency range of 100 Hz – 40 MHz.

$$f_c = \frac{1}{2\pi}\left(\frac{\sigma}{\varepsilon_0 \varepsilon_r}\right) \text{ ……(4.4)}$$

Material	f_c
Air	21.5 mHz
DI Water	12.36 Hz
Tap water	11.24 kHz
Low Saltwater Conc.	65.16 kHz
High Saltwater Conc.	19.98 MHz
PBS 0.01M	337.21 MHz

Table 4.2: Relaxation frequency of the media.

Using Figure 4.2 as a reference, a first-order direct conversion of the system is depicted in Figure 4.3, without and with a passivation layer. In the model without the passivation layer, the effects that need to be considered include the resistance at the contacts, the double-layer capacitance that arises at the interface between the electrode and the electrolyte, and the resistance due to the solution. Additionally, the capacitance of the substrate and any other parasitic capacitances that may arise should be taken into consideration. Analyzing these electrical parameters is crucial because the total impedance is dominated by different circuit elements at different frequencies. In the model with a passivation layer, an additional capacitance needs to be considered due to the passivation. The expected behavior is a result that is predominantly capacitive. Additionally, at certain frequencies, the resistive effect due to the solution, known as the solution resistance, can still be observed.

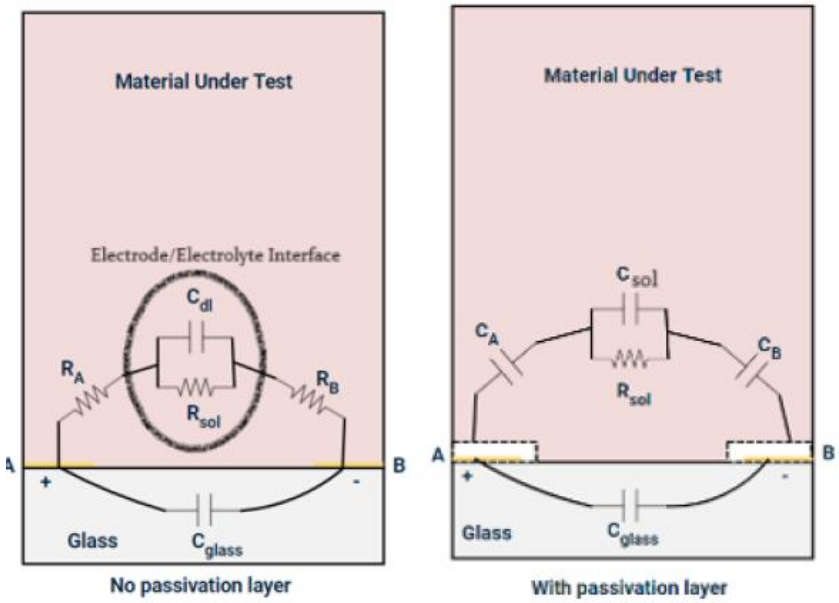

Figure 4.3: First Order circuit equivalent.(Left)-Without passivation layer (Right)- With a passivation layer.

4.1.2 Simulation Results

The plots obtained from the simulation shows the frequency response of various materials. The materials are air, deionized (DI) water, tap water, low saltwater concentration, high saltwater concentration, and PBS 0.01M.

- **Without a passivation layer:**

The blue line representing air has a uniform slope across the frequency range. This slope implies capacitive behaviour. The phase plot for air reveals a phase angle of around -90 degrees over the entire frequency range, which is consistent with pure capacitive behaviour. Among Aqueous solutions, DI water has the lowest conductivity due to the lack of ions. In comparison with air, DI water (green line) also exhibits capacitive behaviour within the observed frequency range. Although it starts with some resistive behaviour at the lowest frequencies observed, it shows lower resistivity due to being more conductive than air.

Among the aqueous solutions, PBS 0.01M exhibits low resistivity, as indicated by its low impedance in the magnitude plot across the observed frequency range. This is due to its high conductivity of 1.5 S/m. Because its knee point (f_c) is at the higher end of the frequency spectrum, it shows predominantly resistive behaviour with the phase angle close to 0 degrees for almost the entire frequency range. Tap water exhibits higher resistivity compared to saltwater and PBS solutions because it contains fewer dissolved ions. This is evident in the impedance plot, where the line representing tap water lies above those for saltwater and PBS, indicating higher impedance and therefore higher resistivity. Saltwater and PBS, which contain higher concentrations of ions, display lower impedance, reflecting their lower resistivity.

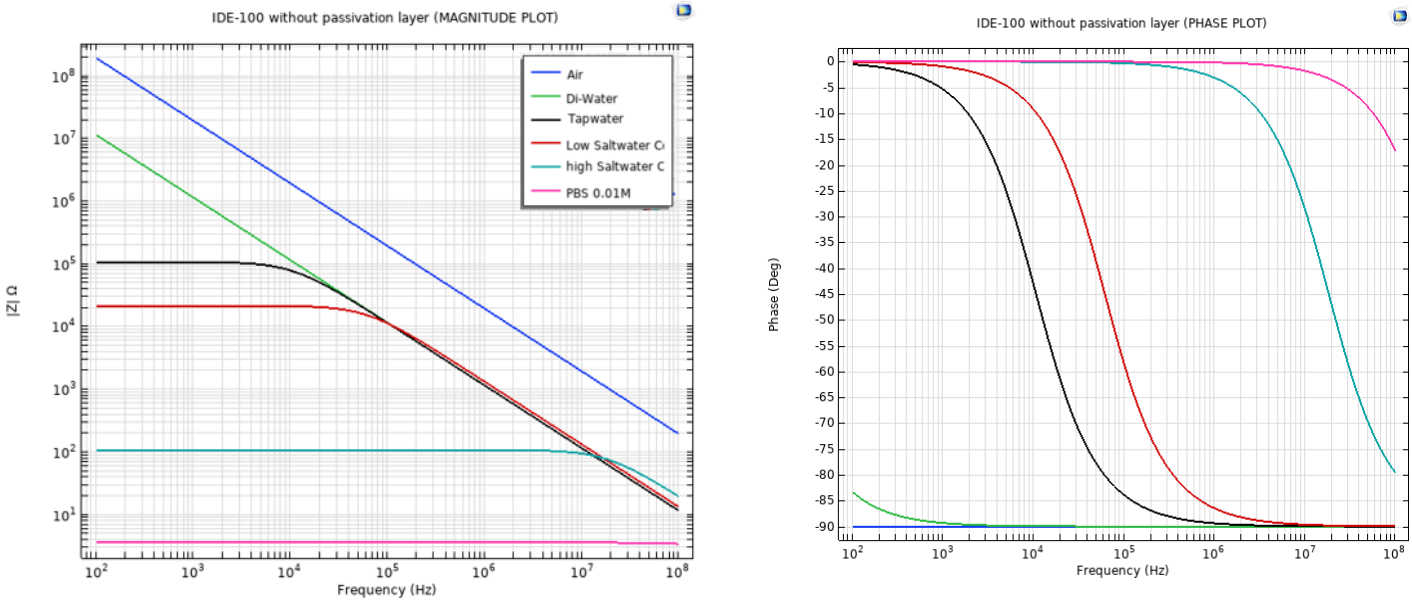

Figure 4.4: Bode Plot of IDE without passivation. (Left)-Modulus. (Right)-Phase.

- **With a passivation layer**

With the addition of a passivation layer, the impedance and phase response of the IDE when exposed to different materials are significantly affected. The passivation layer introduces an additional capacitance, resulting in increased impedance and distinct phase transitions for each material. This added capacitance causes the curves to exhibit predominantly capacitive behaviour, except at frequencies near the relaxation frequency where notable phase shifts occur.

Comparing all the graphs with different passivation layers, we can observe that the frequency of these phase peaks remains constant, indicating that the type of passivation layer does not significantly alter the fundamental capacitive and resistive properties of the materials. The peaks in the phase plots for the same materials occur at roughly the same frequencies. However, the exact amplitude of these phase peaks may vary slightly due to the differing dielectric properties of the passivation layer. The materials with higher conductivity have their phase peaks at higher frequencies, while materials with lower conductivity exhibit peaks at lower frequencies. This behaviour is consistent across all passivation layers.

The varying amplitudes of the phase peaks, such as those for tap water and low saltwater concentration, as well as other materials, are influenced by their specific conductivities, permittivities, and interactions with the passivation layer. Higher conductivity and permittivity typically lead to more pronounced phase shifts, while the dielectric properties of the passivation layer and the material's relaxation frequency further modulate these amplitudes.

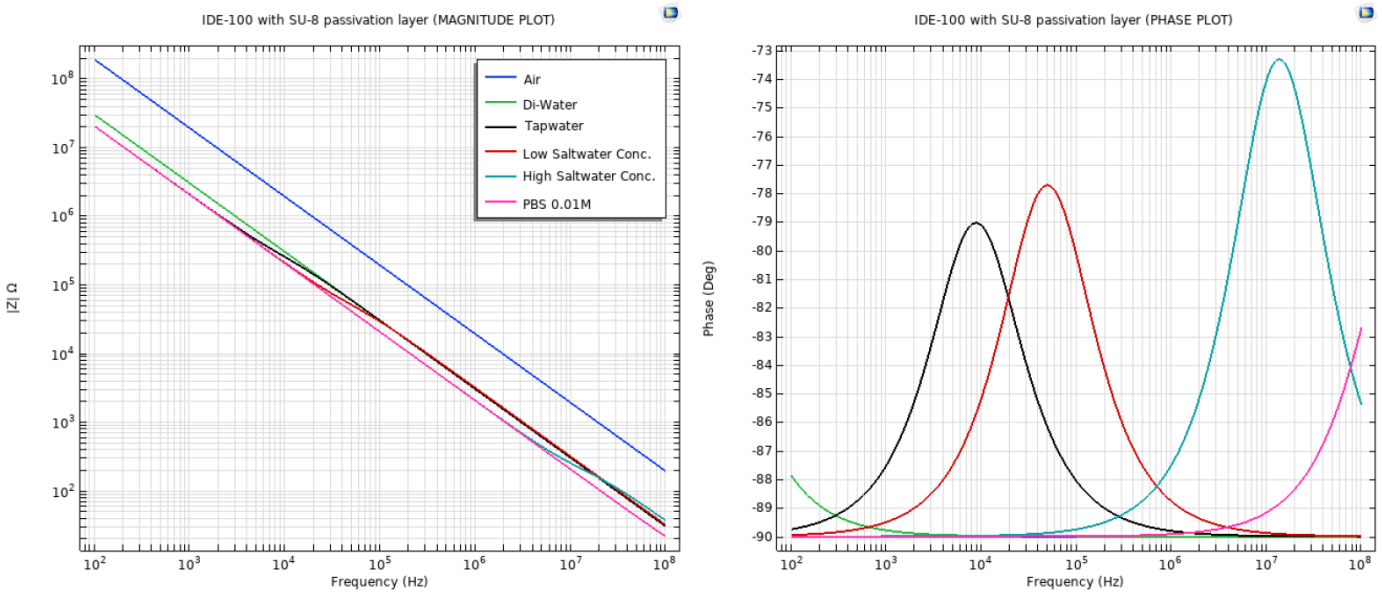

Figure 4.5: Bode Plot of IDE with SU-8 passivation layer. (Left)-Modulus. (Right) - Phase.

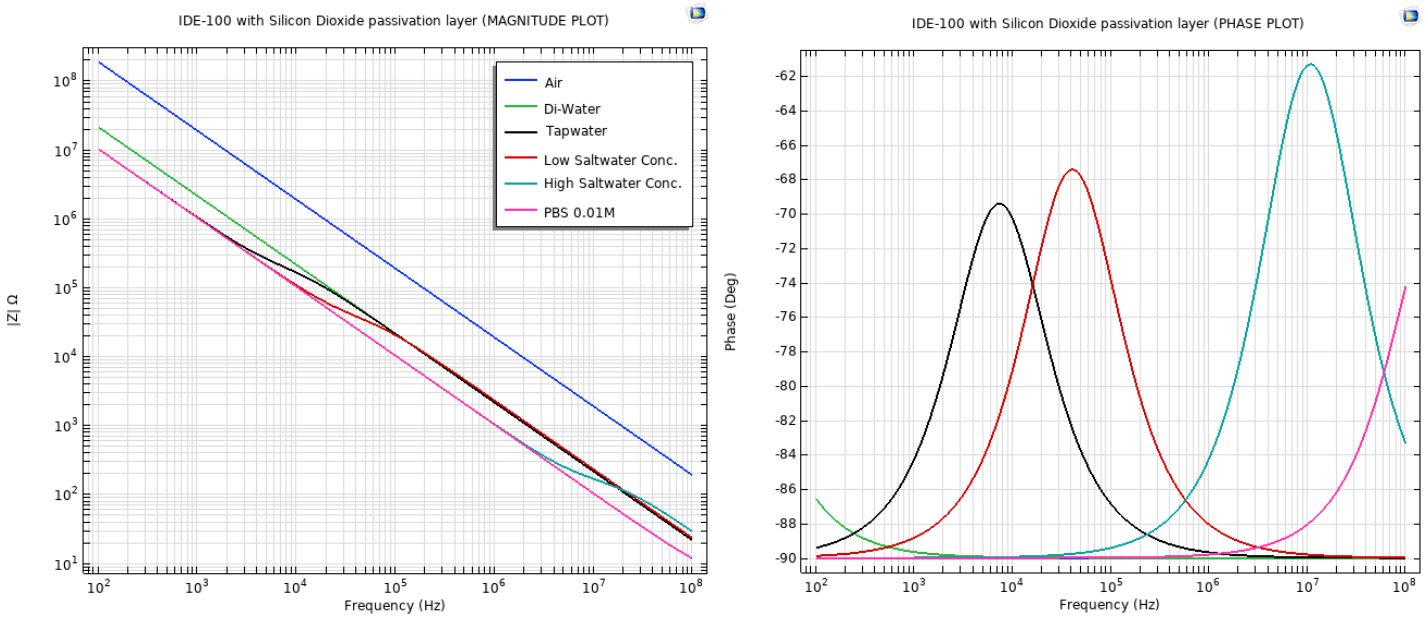

Figure 4.6: Bode Plot of IDE with Silicon Dioxide passivation layer (1um thickness). (Left)-Modulus. (Right)-Phase.

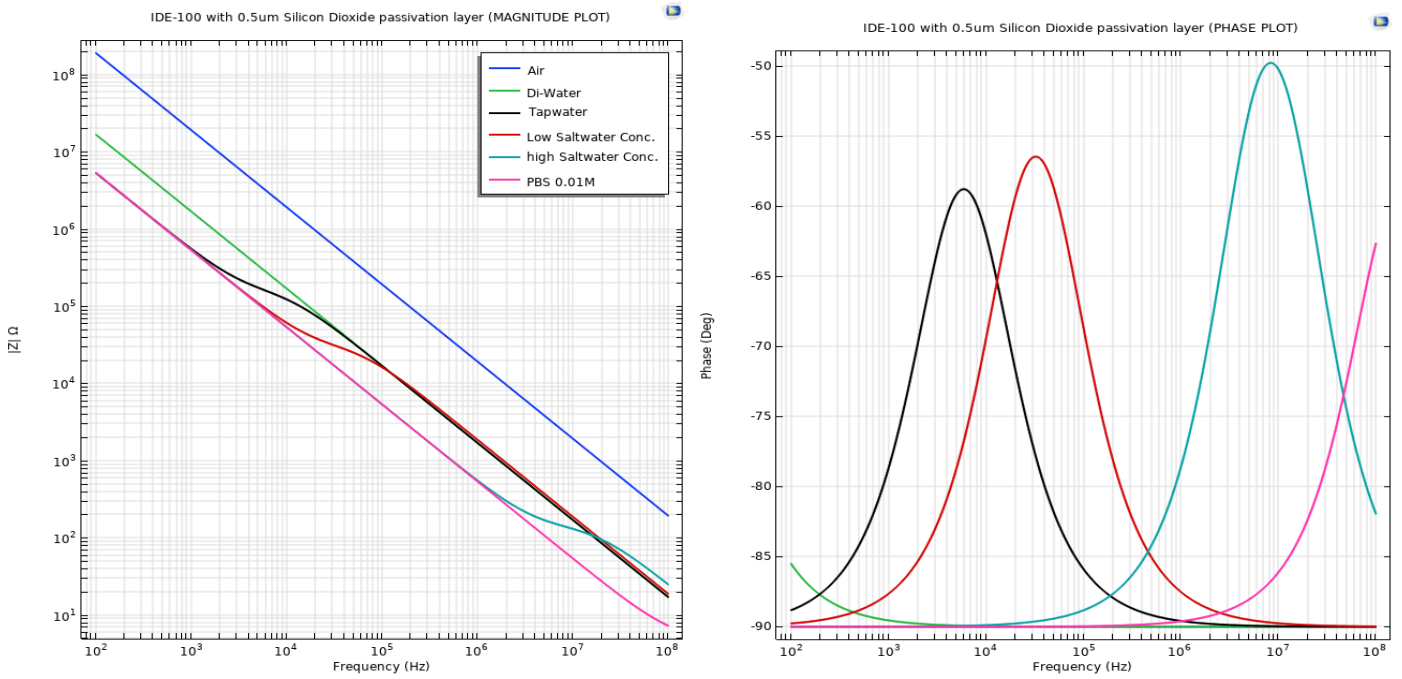

Figure 4.7: Bode Plot of IDE with Silicon Dioxide passivation layer (500nm thickness). (Left)-Modulus. (Right)-Phase.

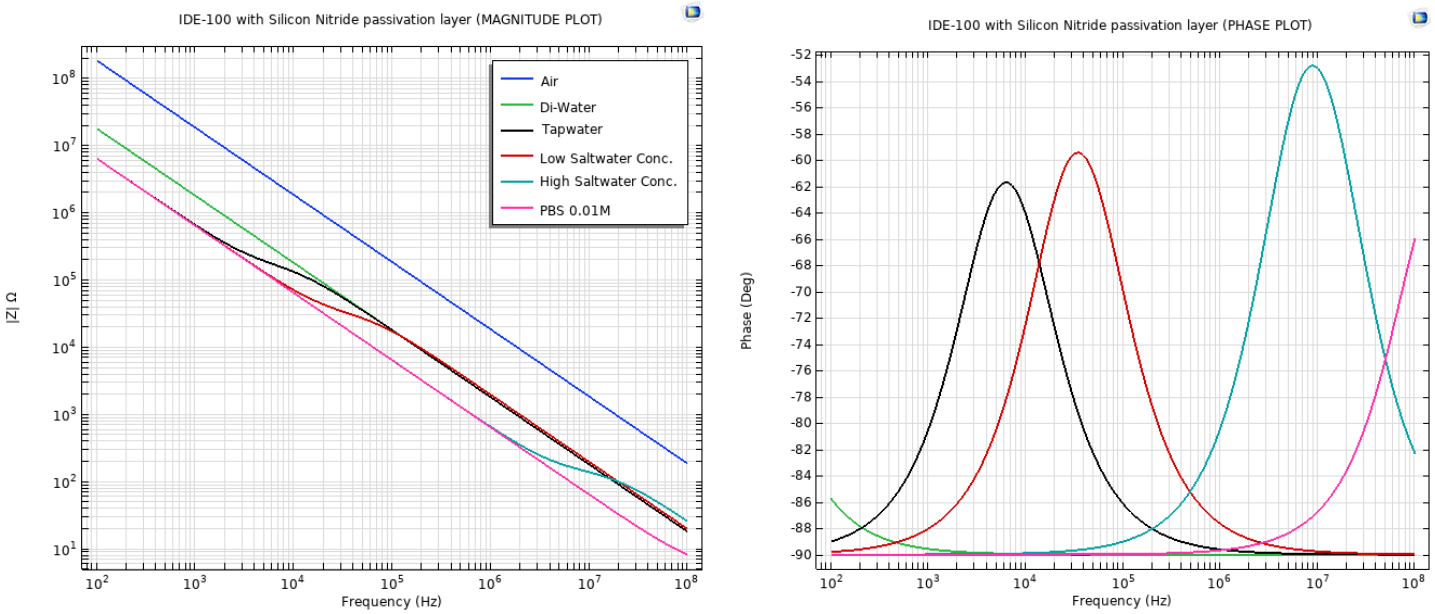

Figure 4.8: Bode Plot of IDE with Silicon Nitride passivation layer (1um thickness). (Left)-Modulus. (Right)-Phase.

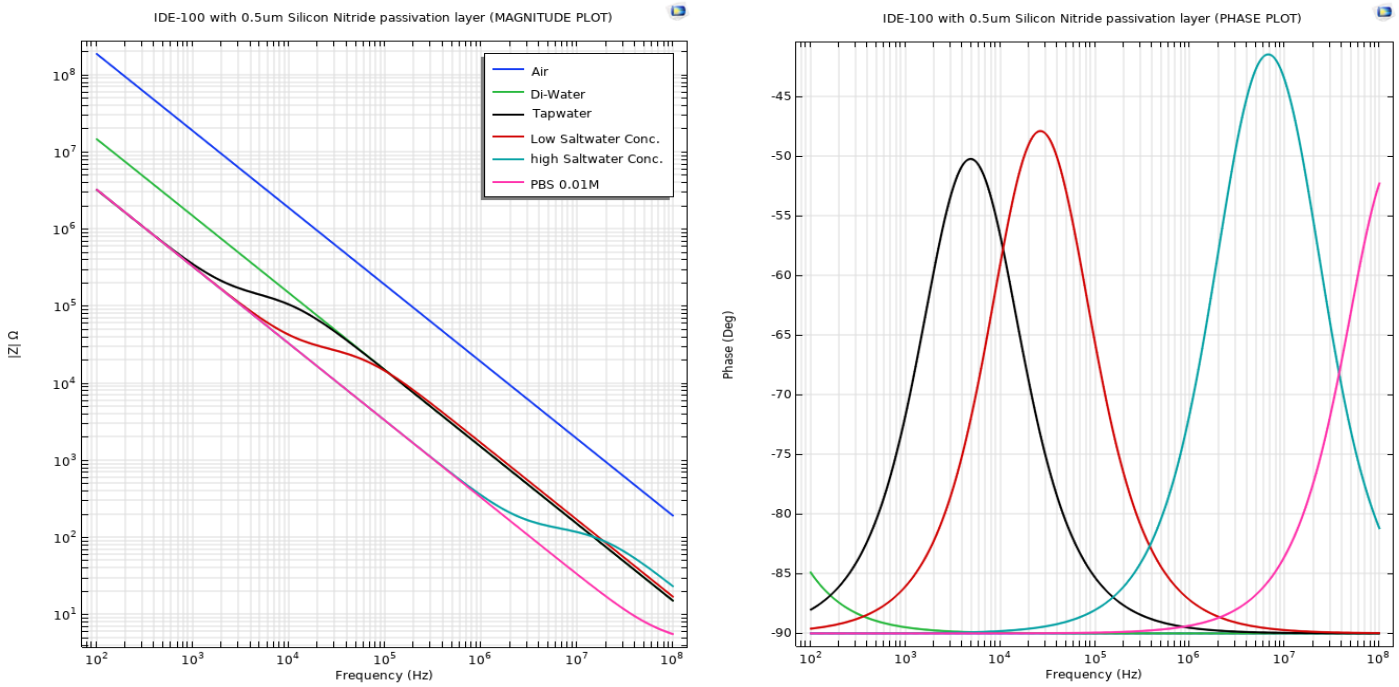

Figure 4.9: Bode Plot of IDE with Silicon Nitride passivation layer (500nm thickness). (Left)-Modulus. (Right)- Phase.

4.1.3 Diamond as a passivation layer

In this thesis, the initial plan involved using intrinsic diamond as a passivation material. However, due to technical issues, this was not feasible. Nevertheless, simulating the effect of diamond as a passivation layer using COMSOL was interesting, which is discussed in this section.

Intrinsic diamond, characterized by a conductivity of 1.6e-7 S/m and a permittivity of 5.7, was simulated to understand its behaviour as a passivation layer. Diamond has a very low surface energy and different surface chemistry compared to other materials used as passivation. This can influence the accumulation of charges at the interface, affecting the phase response. Surface conduction, low conductivity, and potential EM transmission contribute to the observed behaviour in the Bode plots. At low frequencies, the Bode plot shows that the system behaves in a predominantly resistive manner. The effect of surface conduction becomes more pronounced. Impurities, adsorbed species, and ions on the diamond surface can provide pathways for conduction, contributing to resistive losses.

To understand more comprehensively why diamond exhibits such unique behaviour at low frequencies, further investigation into the intrinsic characteristics and surface properties of diamond is essential. Additionally, studying the interaction mechanisms between diamond and the surrounding environment will provide deeper insights into the observed impedance responses.

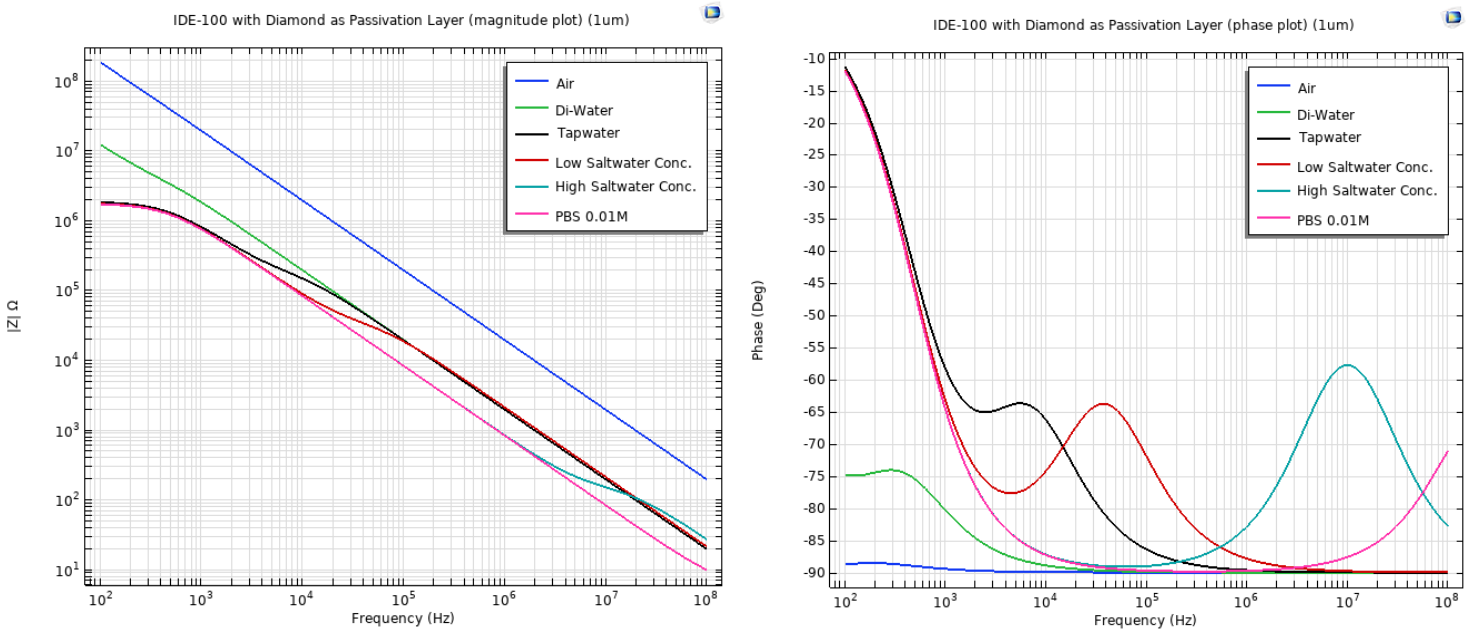

Figure 4.10: Bode Plot of IDE with Diamond as a passivation layer. (Left)-Modulus. (Right)- Phase.

4.2 Experimental Analysis

Experimental analysis of Interdigitated electrodes, particularly using Electrochemical Impedance Spectroscopy (EIS), is pivotal for comprehending the electrical characteristics and performance of IDE structures. EIS offers invaluable insights into the intricate relationship between resistive and capacitive components within an electrical circuit over a spectrum of frequencies.

4.2.1 Test setup and Conditions

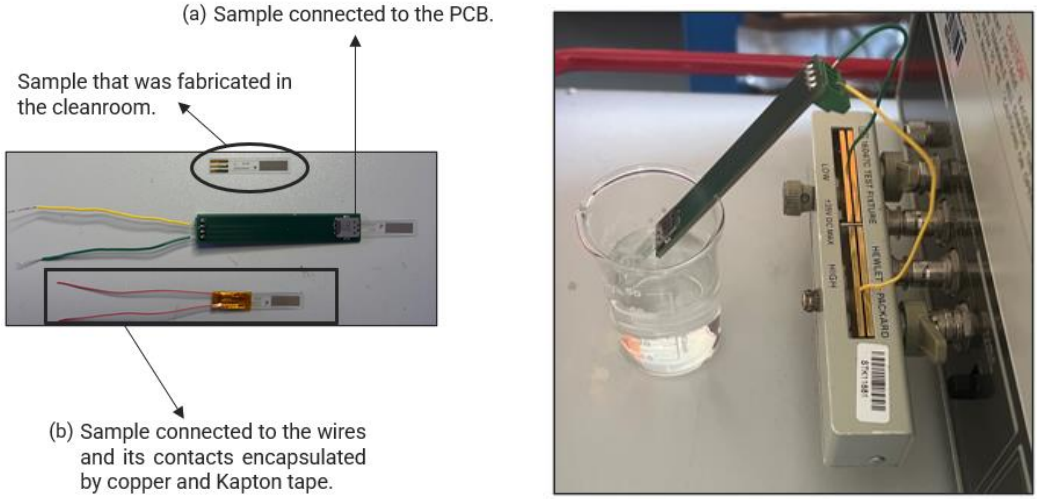

Figure 4.11: (Left)-Fabricated IDE connected via PCB or wires for Impedance Analysis. (a)-Sample that was fabricated in the cleanroom. (b)-Sample connected to the PCB. (c)-Sample connected to the wires and its contacts encapsulated by copper and Kapton tape. (Right)-Sample connected to the PCB immersed in aqueous solution.

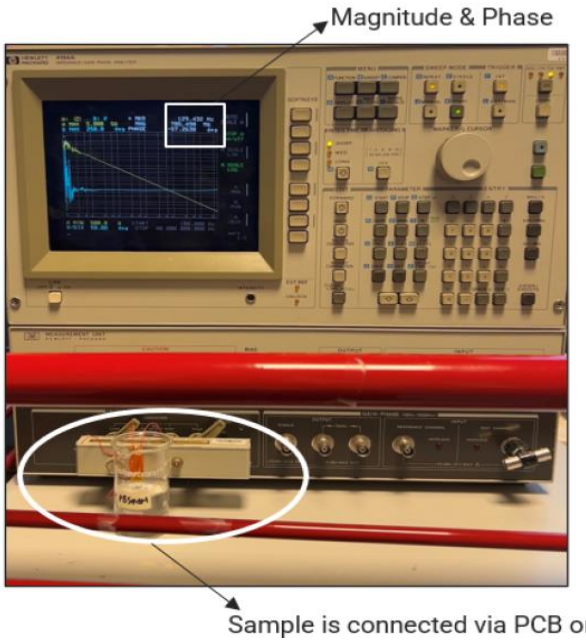

Figure 4.12: Impedance Analyzer 4194A used for impedance analysis. Input= 1V, Freq range=(100-20M) Hz.

The HP-4194A analyzes impedance by scanning a specified frequency range, measuring the admittance and the phase, and then transmits this information to the computer [12]. Standard calibration of the system was done using protocol from the manufacturer. In this section the experimental setup and test conditions are discussed. The impedance analyzer HP-4194A that is shown in Figure 4.12 was used, which analyzes impedance by scanning a specified frequency range, here, from 100Hz to 20MHz in order to compare the results of the behavior of the electrodes and also to determine parameters like the capacitance and parallel resistance. In our instance, we evaluated the magnitude and phase of the IDE electrodes that have 25, 50, and 100 pairs of interdigitated fingers with and without a passivation layer. A 1V perturbation input was applied and the measurements were taken with the shortest integration time available for the impedance analyzer. The fabricated IDE sample was connected to the impedance analyzer via PCB or wires, as shown in Figure 4.11, the impedance spectroscopy was first done with air as the medium, and then subsequently in aqueous solutions. The HP-4194A automatically measures the impedance at each frequency point and plots the Bode plots on the screen. Once the sweep is complete, one can save the measurement data by data transfer to a connected PC using an appropriate interface.

Most often, BIS is represented by a bode plot as the simplest tool to understand the performance of the samples at different frequency ranges. The use of Bode plots makes it easier to identify the contribution of different circuit parameters to the frequency response of IDEs. The impedance magnitude (magnitude of the complex impedance) will provide information about the resistance of the IDE, and the impedance phase angle will provide information about the capacitance of the IDE. The bode plots show the magnitude and phase response of the system that is plotted on MATLAB and the behaviors of the electrodes can be differentiated as shown in the following sub-sections.

4.2.2 Test Results

Impedance measurements were first carried out in air in order to determine the total capacitance of the system. This capacitance would include any parasitic capacitances in parallel, for example, due to the cables connecting the IDEs to the impedance analyser [36]. This was followed by measurements in aqueous solutions of varying conductivity. The solutions add additional impedances in the system. For mediums with varying conductivities, saturation was observed at different frequencies. This saturation occurred at progressively lower impedance values and at progressively higher frequencies, as the solution conductivity was increased. Multiple measurements were conducted, and the plotted data represents the average value derived from these measurements at each frequency.

The experimental analysis results are shown in the Bode plots for IDE-100 in the figures below. To ensure the accuracy of our experimental results, we conducted a COMSOL simulation. This simulation, detailed in the previous section, section 4.1.2, allowed us to validate our findings. When we compared the experimental data with the simulation results, The experimental results were consistent with the simulation results, i.e., we observed a significant similarity between them. This is further analysed in the comparative plots in the subsequent sections.

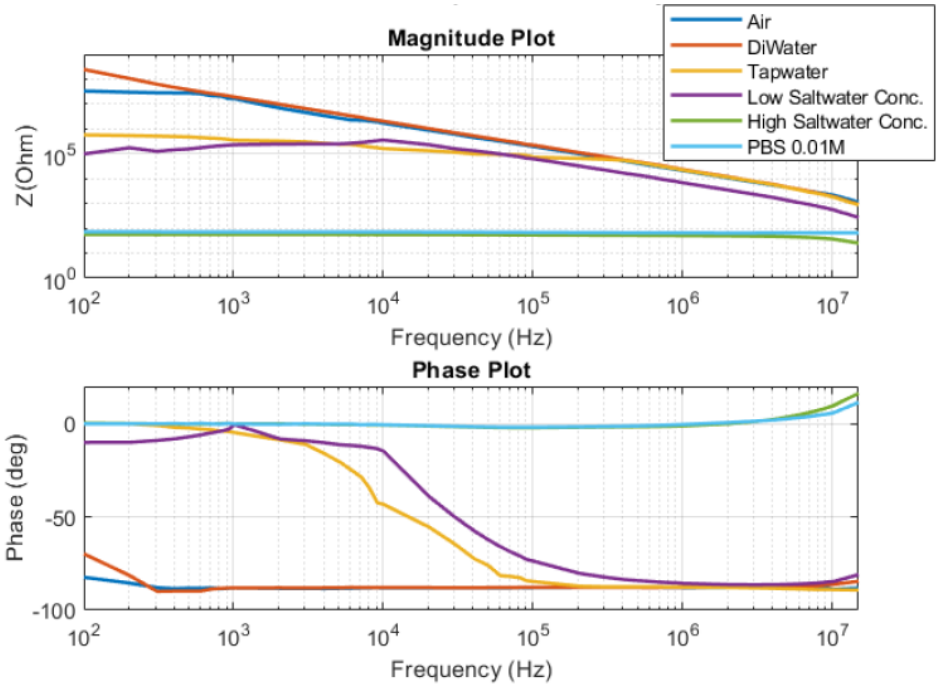

Figure 4.13: Bode Plot of IDE-100 with no passivation.

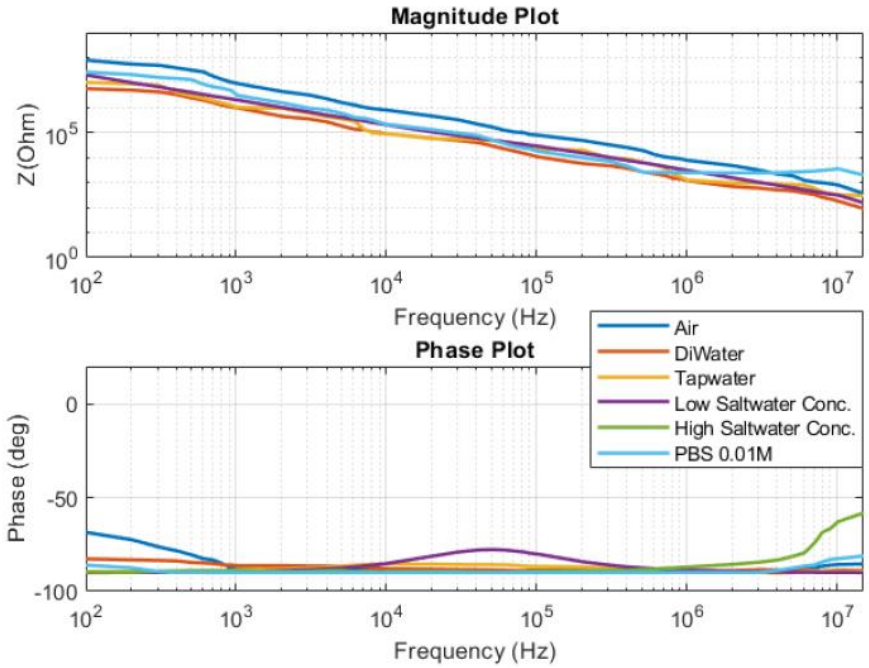

Figure 4.14: Bode Plot of IDE-100 with SU-8 as a passivation layer.

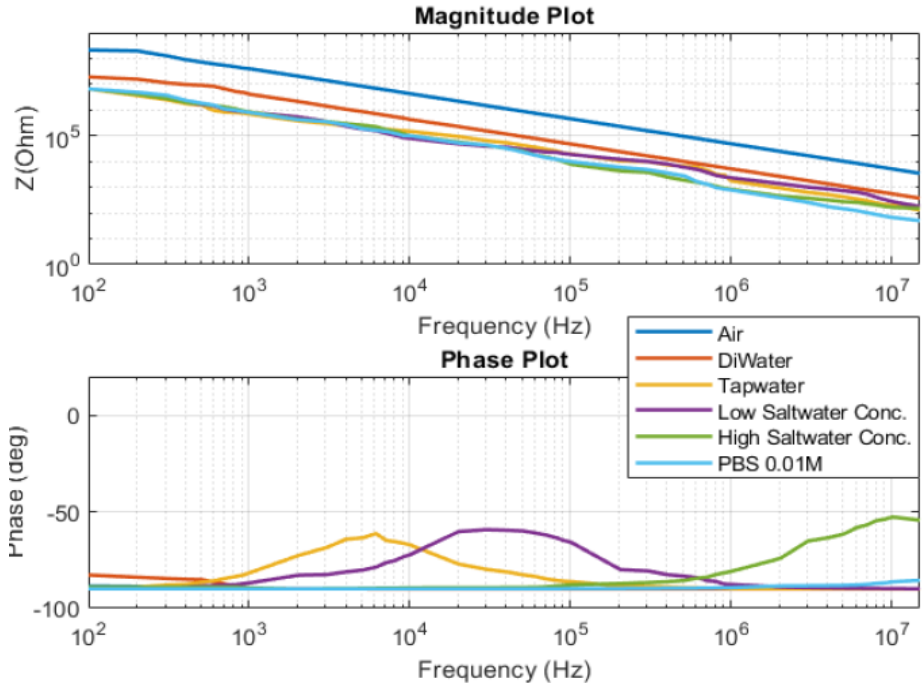

Figure 4.15: Bode Plot of IDE-100 with silicon nitride of thickness 1µm as a passivation layer.

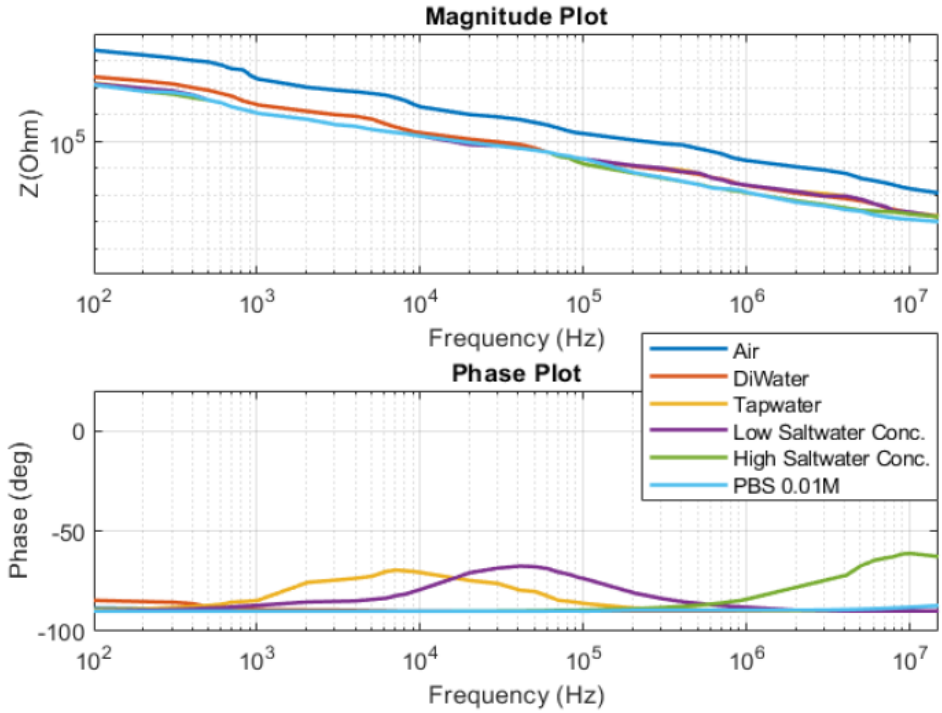

Figure 4.16: Bode Plot of IDE-100 with silicon dioxide of thickness 1µm as a passivation layer.

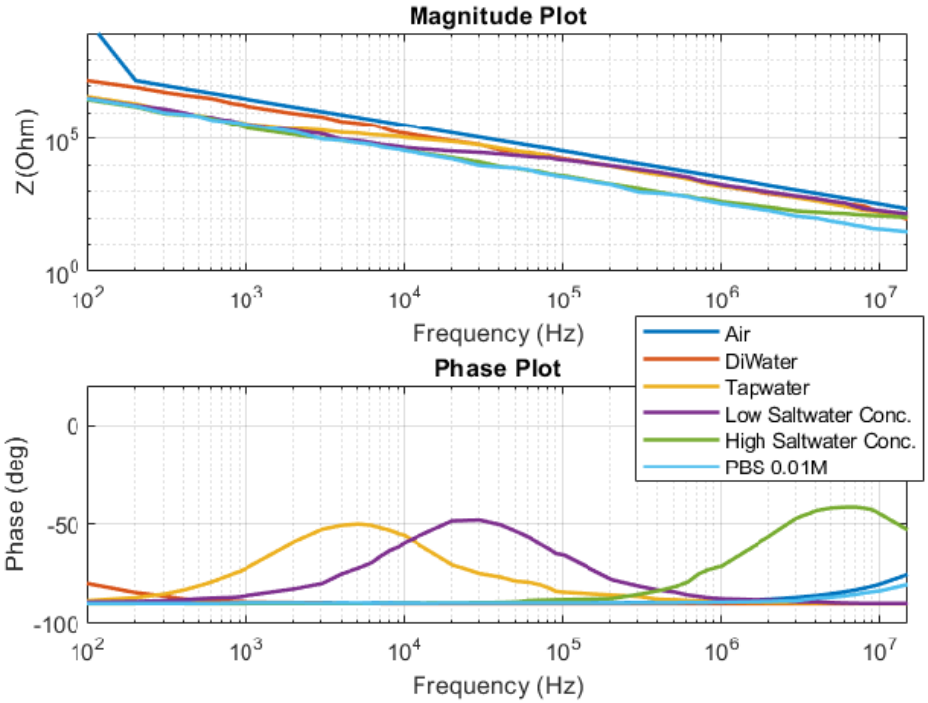

Figure 4.17: Bode Plot of IDE-100 with silicon nitride of thickness 0.5µm as a passivation layer.

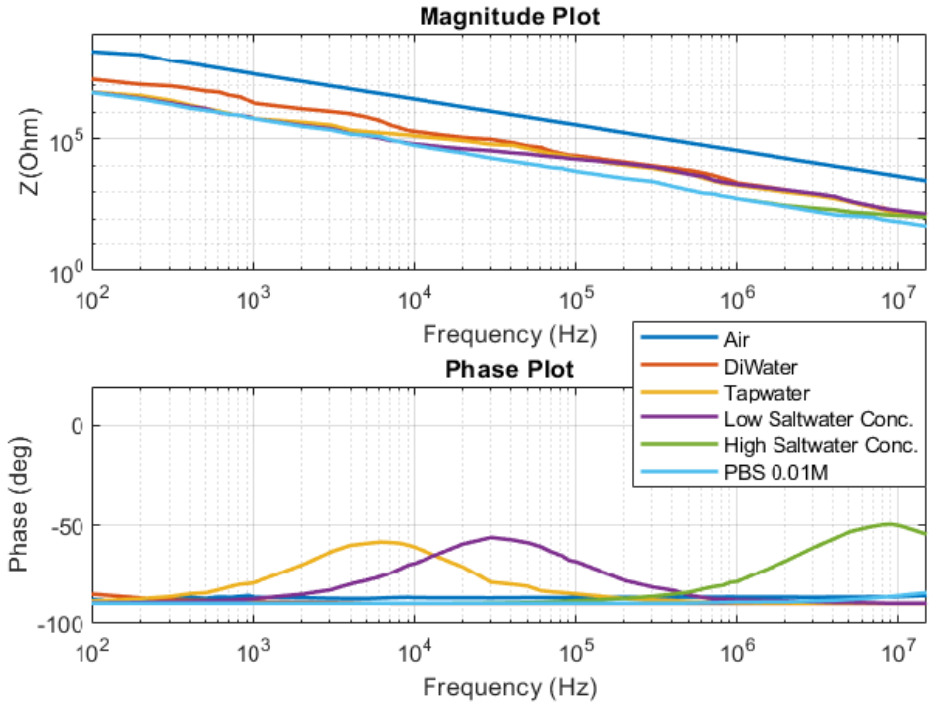

Figure 4.18: Bode Plot of IDE-100 with silicon dioxide of thickness 0.5µm as a passivation layer.

4.2.3 Other Impedance Analysis Methods

Impedance analysis can be performed using various tools such as the HP 4194A Impedance Analyzer, PSTrace, and the Longevity Test Bench (Includes an analog discovery+custom multiplexer, discussed in section 6.2). While the HP 4194A is a reliable and standard method for a wide range of frequencies, PSTrace is particularly effective for analyzing impedance at very low frequencies(<100Hz). The plots for methods other than the HP 4194A show an offset when compared to COMSOL simulations, which could be attributed to differing input conditions during the experiments.

Impedance analysis can be performed using various tools such as the HP 4194A Impedance Analyzer, PSTrace, and the Longevity Test Bench. While the HP 4194A is a reliable and standard method for a wide range of frequencies, PSTrace is particularly effective for analyzing impedance at very low frequencies. The plots for methods other than the HP 4194A show an offset when compared to COMSOL simulations, which could be attributed to differing input conditions during the experiments.

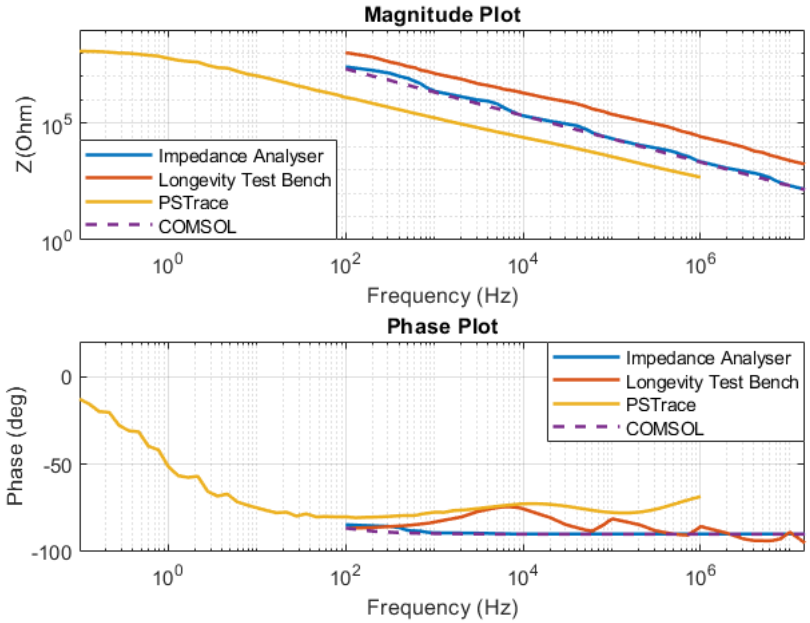

Figure 4.19: Comparative Analysis of IDE-100 (SiO2 passivation) in DI water.

4.3 Comparative Analysis

In this section, we compare and contrast the features and performance of various materials and combinations using comparative analysis. This involves examining results in order to find trends, similarities, and contrasts by methodically analyzing the impedance responses under various conditions. Through the analysis of these variations, we may gain a deeper understanding of the ways in which various aspects, including material qualities, electrode configurations, and environmental factors, impact overall performance. In addition to offering insights into prospective

enhancements and applications, this comparison method aids in determining the best configurations.

4.3.1 Simulated Data V/S Experimental Results

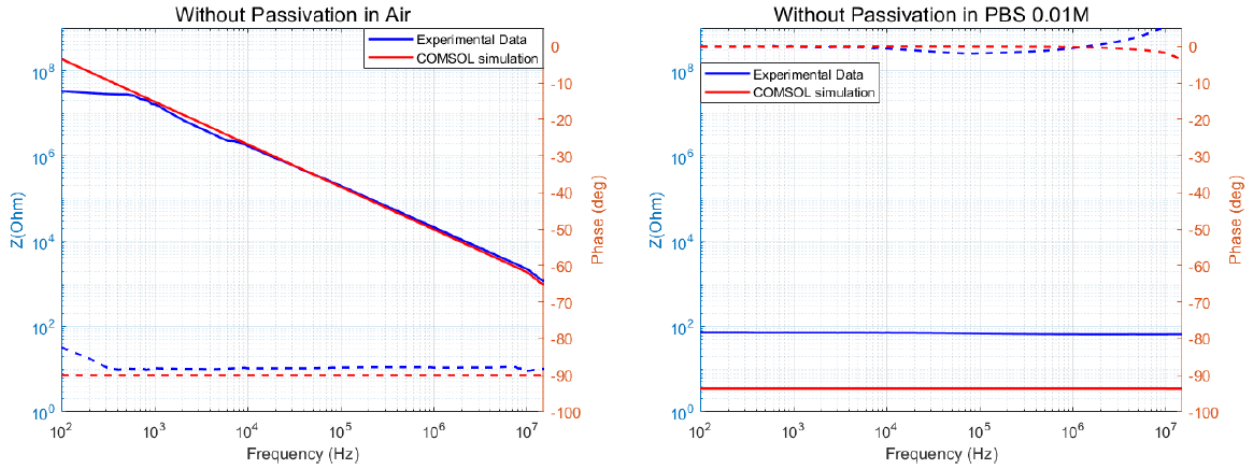

Figure 4.20: Simulated data V/s experimental data of IDE without passivation layer. (Left)-In Air. (Right)-In Phosphate- buffered saline solution.

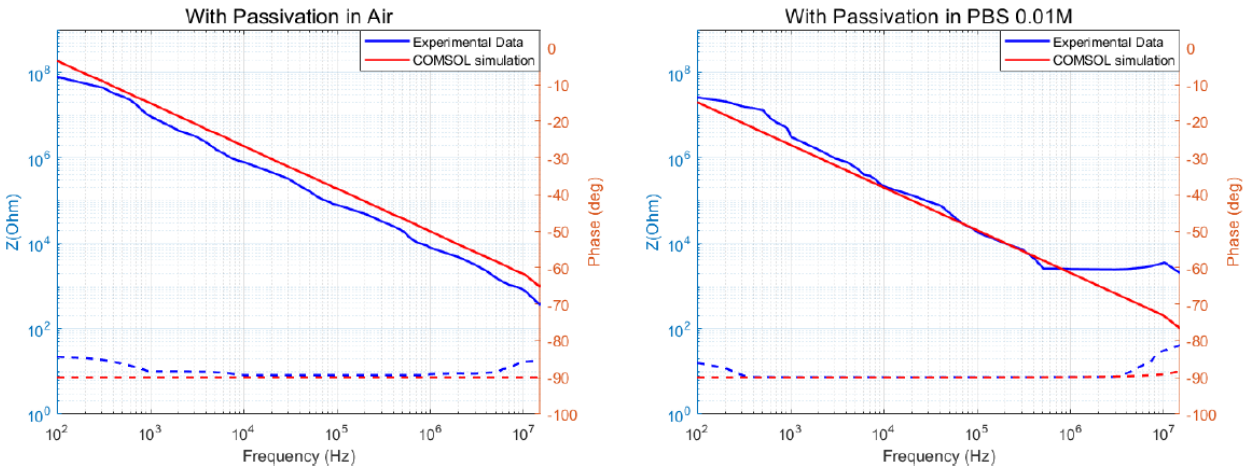

Figure 4.21: Simulated data V/s experimental data of IDE with passivation layer. (Left)-In Air. (Right)-In Phosphate- buffered saline solution.

The COMSOL simulations and real-world results show numerous significant differences when comparing the impedance of IDEs with and without passivation.
Analyzing results of IDE without passivation, experimentally we observe some deviations due to real-world imperfections such as electrode surface roughness, impurities, and measurement noise. In addition, the experimental data might show other capacitive and resistive components—such as parasitic effects from the measurement setup—that are not taken into consideration in the simulation. Analyzing the results of IDEs with passivation, variations in the thickness, uniformity and material properties of the passivation layer may vary, leading to differences between simulation and experiment. In addition, imperfect or defective passivation layers in the actual

world might have an impact on the impedance that differs from that of an idealized simulation model.
Figure 4.20 displays a comparison plot of IDE with passivation in air. The low-frequency region's differing impedance slope can be attributed to the real sensor's defective electrode surface as opposed to the simulation model. We acquire a capacitive element CPE for the observed sensor owing to the surface roughness and impurities, as opposed to a real capacitance C in the FEM simulations [34]. Analyzing the graph with PBS solution as the medium, specifically at a frequency of 1 kHz, one can observe that the experimental impedance exceeds the COMSOL simulation result which indicates that there may be factors not fully captured or accounted for in the COMSOL simulation that influence the experimental results.

4.3.2 IDE with Varied Finger Configurations

In this section, we perform a comparative analysis of impedance measurements obtained from fabricated IDE configurations: IDE-100, IDE-50, and IDE-25. Varying the number of these finger-like digits in the IDE configurations is crucial for optimizing their performance in sensing and electrochemical applications. When compared to configurations with more fingers, IDE-25 usually has a greater impedance due to fewer fingers. This is due to reduced surface area and capacitance, resulting in less interaction with the surrounding medium and higher resistive properties. As a result, the capacitance is said to decrease with a decrease in the number of fingers and vice versa [37].

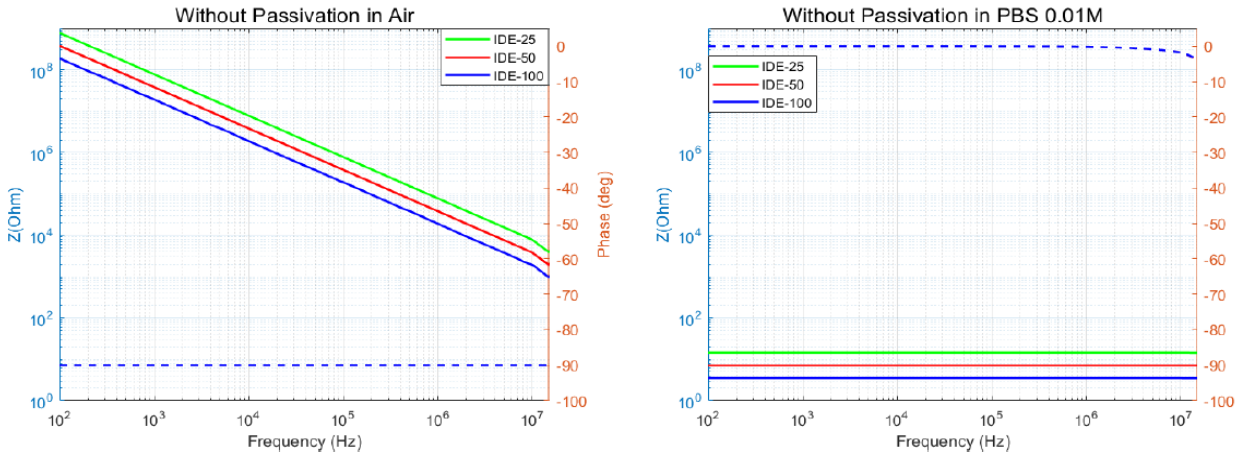

Figure 4.22: IDE-25, IDE-50 and IDE-100 without passivation layer. (Left)-In Air. (Right)-In Phosphate-buffered saline solution.

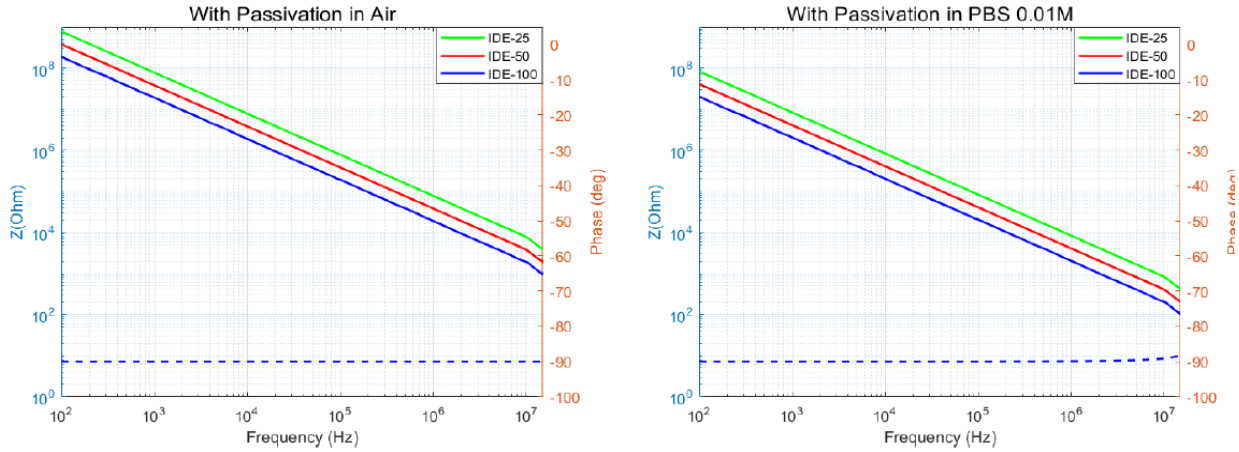

Figure 4.23: IDE-25, IDE-50 and IDE-100 with passivation layer. (Left)-In Air. (Right)-In Phosphate- buffered saline solution.

4.3.3 With Passivation V/S Without Passivation layer

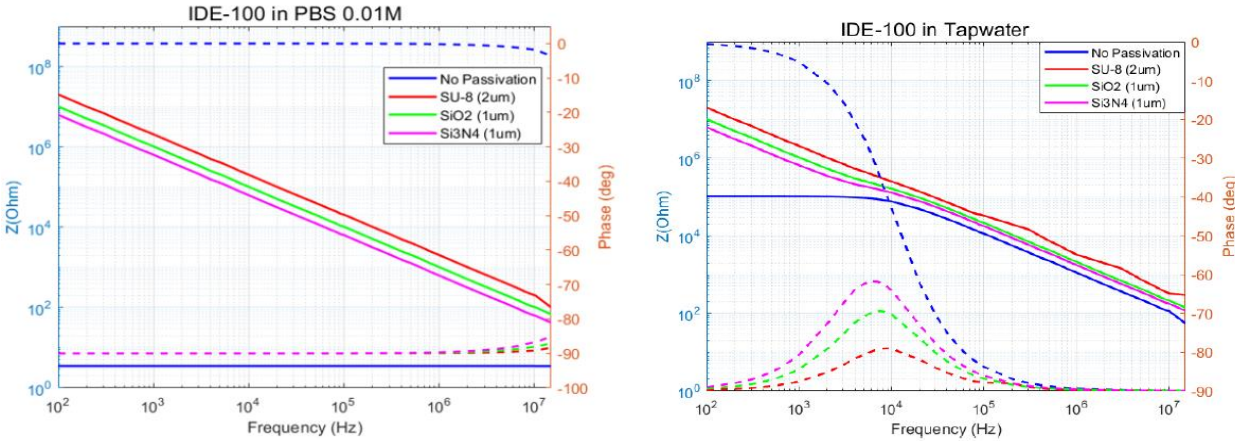

Figure 4.24: Comparison of IDEs with and without Passivation, Highlighting Differences Across Various Passivation Materials. (Left)-In Phosphate- buffered saline solution. (Right)-In Tap water.

In this comparative analysis, we investigate the influence of passivation on the impedance characteristics of Interdigitated Electrodes (IDEs). We compare IDEs without passivation with IDEs with different kinds of passivation layers, including SU-8, silicon nitride, and silicon dioxide. This thorough method investigates how different passivation arrangements and materials affect electrical characteristics, especially impedance. Understanding this is crucial for improving passivation techniques to improve sensor sensitivity and reliability in a variety of applications, such as electrochemical and biosensing.

- **Without Passivation:** IDEs without passivation typically exhibit a high capacitive behavior across a wide range of frequencies. This is because of the configuration of the IDE as a parallel plate capacitor and also due to the electrode surface directly interacting with the surrounding medium, leading to significant capacitance due to the electrode-electrolyte interface. As observed in the phase plot, at lower frequencies, the impedance of

IDEs without passivation is primarily resistive, influenced by factors such as electrode material and solution conductivity.

- **With Passivation:** The specific passivation material (e.g., SU-8, silicon nitride, silicon dioxide) influences impedance characteristics. Each material may introduce additional capacitance or alter resistive properties, impacting impedance measurements differently. Analyzing the behavior in Tap water, it is observed that the difference in the amplitudes of the peaks in the phase plot are due to a combined effect of the relative permittivity, conductivity and thickness of the passivation material itself.

4.3.4 Si_3N_4(1µm) V/S Si_3N_4 (0.5µm)

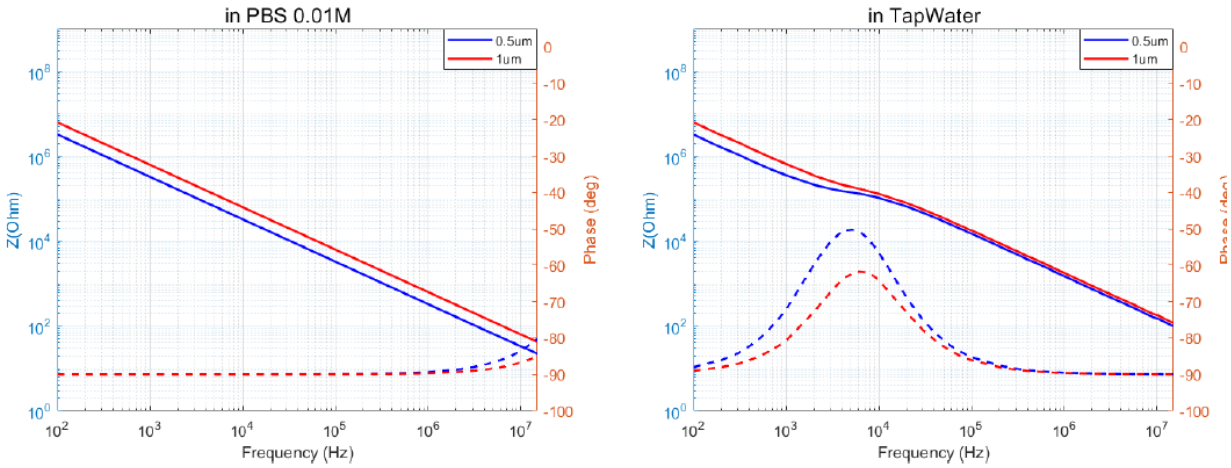

Figure 4.25: Comparison of IDEs with the Same Passivation Material but Varying Thicknesses. (Left)-In Phosphate- buffered saline solution. (Right)-In Tap water.

In this subsection, we explore the impedance characteristics of Interdigitated Electrodes (IDEs) coated with silicon nitride (Si_3N_4) passivation layers of varying thicknesses: 1 µm and 500 nm. By examining IDEs with these different thicknesses of silicon nitride, we aim to understand how variations in passivation layer thickness influence impedance behavior. This investigation is essential for optimizing sensor performance by identifying the most effective passivation thickness for the desired application.

While both silicon nitride passivation layers have the same electrical properties, the impedance modulus typically decreases with increasing thickness of the passivation layer. This is because a thicker passivation layer reduces the capacitance between the electrodes and the surrounding medium because the electric field lines are more confined within the passivation material, leading to a lower capacitive reactance and thus a higher impedance modulus. A thinner passivation layer might exhibit a higher phase peak (approaching zero phase angle) due to its higher capacitive reactance at specific frequencies compared to a thicker layer. As the thickness of the passivation layer varies, so does the capacitance, and hence the system's RC time constant. The RC time constant influences the frequency of impedance peaks. As a result, the resonance frequency changes as the capacitance fluctuates with the thickness of the passivation layer. This difference

in resonance frequency, despite identical material characteristics and other parameters, demonstrates the importance of passivation layer thickness in IDE impedance behavior.

Chapter 5

Equivalent Circuit Fitting

Electrochemical impedance spectroscopy (EIS) is an effective means for understanding the processes at the electrode-electrolyte interface. One of the key advantages of employing impedance spectroscopy (IS) is to investigate the electrical and electrochemical characteristics of materials and systems is the direct association often observed between the behavior of a real system and that of a simplified model circuit composed of discrete electrical components. Here, one can compare or fit the impedance data to an equivalent circuit, that represents the actual processes in the system. Analyzing the impedance spectrum provides information about the electrical properties of the IDE and its surroundings: This data can be used to investigate the material's qualities, the presence of faults, and their impact on the material's attributes. It can also be used to optimize materials and enhance their performance in a variety of applications.

5.1 Fitting Basics

Electrochemical cells can be modeled as a network of passive electrical circuit elements. This network is called an equivalent circuit. The electrical equivalent circuit is created by arranging electrical elements such as resistors (R), capacitors (C), and inductors (L), as well as ad-hoc elements like constant phase element (CPE) and Warburg (W), to represent the data obtained using EIS. Every element has an impedance $Z(\omega)$ that may be varied throughout the fit and is represented by a complicated function that is frequently frequency dependent. This impedance response of an equivalent circuit is fitted to the electrochemical impedance data to extract the values of the circuit components. Generally speaking, an arrangement of electrical components in series, parallel, or a combination of both series and parallel can provide an electrical equivalent circuit.

Randle's equivalent circuit is the commonly addressed circuit model employed for interpreting EIS experimental outcomes in electrical representation, as illustrated in Figure 5.1 [1].

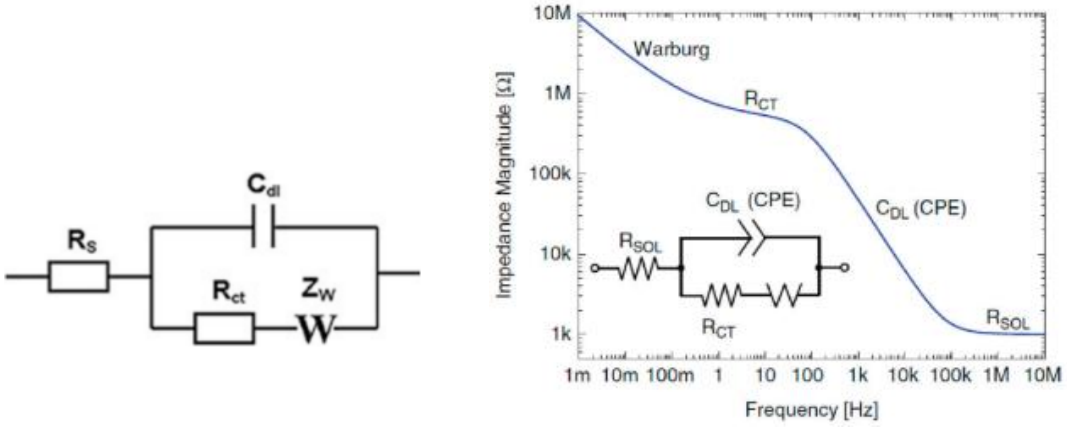

Figure 5.1: (Left)Randles equivalent circuit model [38]. (Right) Bode Plot of the impedance magnitude of the Randle's equivalent model of an electrochemical interface comprising of both faradaic and non-faradaic processes [39].

The circuit consists of solution resistance Rs in series connected to a parallel combination of double layer capacitance C_{dl} to the charge transfer resistance R_{ct} in series with Warburg impedance Z_W [40]. In the invasive situation when there is direct contact between the metal electrode and liquid it is equivalent to a circuit consisting of a capacitor C_{dl} in parallel with a resistor R_{ct} both in series with the resistance R_s. In this analysis R_s is the resistance of the main bulk of the liquid, R_{ct} is the resistance of the fluid bridge due to its conductivity effect, and C_{dl} shows its capacitance as a result of its permittivity in addition to the double-layer charging [41]. The current in this case is carried across the interface of a metal-to-electrolyte system in two ways, known as faradaic and non-faradaic methods. The Faradaic Process uses an electrochemical reaction, such as the reduction or oxidation of the samples or certain ions, to move current over the interface. Charged particles cannot pass through the interface during the non-faradaic operation. Instead, the electrical double layer, which functions as a capacitor in series with the solution's ohmic resistance (R_{sol} or R_s), carries the current through its charging and discharging.

In other words, the capacitance depends on the Double-layer charging. So, for the Ions to be attached to the electrode surface (Assuming positive input) as seen in Figure 5.2, they have to be transferred from the bulk or the near-surface in order to be attached to the surface of the electrode –This will depend on the ohmic drop R_s in the electrolyte which is present in series in this circuit. R_{ct} also known as the Charge transfer resistance is dependent on the faradaic current- the electric current that is produced when the negative ions are transferred from the bulk or the near-surface to the electrode surface.

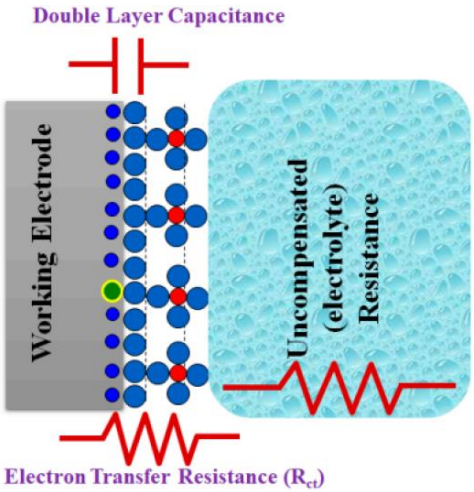

Figure 5.2: Electro chemical reactions at the electrode/electrolyte surface [39].

On the solution side of the interface, the electrons align themselves in opposition to a layer of cations with equal and opposite charges. The generated electric field is called a double layer because it is made up of two layers of charges [42]. It is widely recognized that the capacitance originating from the double layer is not purely capacitive; instead, it is better described as a Constant Phase Element (CPE). For a non-ideal capacitor, the equation is as follows:

$$CPE = -\frac{1}{(J\omega C)^{\alpha}} \dots\dots\dots\dots (5.1)$$

The parameter α, termed the CPE exponent, ranges from 1.0 for a conventional capacitor to 0.5 for a porous electrode. Within this model, the impedance associated with a faradaic reaction comprises of an active charge transfer resistance (R_{ct}) which was previously discussed and a specialized electrochemical component related to diffusion, referred to as the Warburg element [38]. The diffusion of molecules or redox species can produce an impedance called the Warburg impedance (W), which is an additional resistance. This Warburg impedance varies with varying frequencies. That is, the diffusion of reactants to the electrode surface is a slow process that occurs exclusively at low frequencies and hence at low frequencies the Warburg impedance will be relatively high. Conversely, at higher frequencies, the reactants lack sufficient time for diffusion to take place resulting in a low Warburg impedance. A phase shift of 45◦ is observed on the Bode plot referring to the Warburg effect [39]. Mathematically Warburg impedance is given by,

$$Z_w = \frac{2\sigma}{\sqrt{J\omega}} \dots\dots\dots\dots (5.2)$$

The initial step involves the development of a model for the electrode– solution interface and the corresponding electrode process deemed justifiable; this is discussed in the following sections. Subsequently, software accompanying electrochemical impedance instrumentation is utilized to fit all circuit parameters. This fitting process is initiated with reasonably chosen initial values for the circuit parameters. Software tools ZView4 by Scribner, EC Lab (demo version) and EIS spectrum Analyzer were utilized to fit an equivalent circuit to the experimental curves.

5.1.1 Initial Value Measurement

Two methods were used to obtain the initial values of the ohmic resistances in order to start the fitting process:

- **By Direct measurement:** R_S can be directly measured using a multimeter as illustrated in Figure 5.3. As R_S indicates the ohmic resistance of the electrode it can be directly measured.

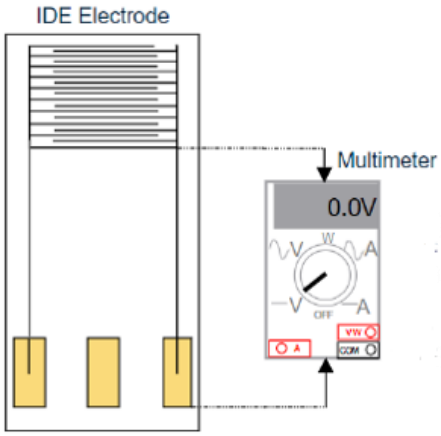

Electrode	Measured $R_S(\Omega)$ (One side)
IDE-100	14.4-15.4Ω x 2 = **30Ω**
IDE-50	21.5-22.2Ω x2 = **43Ω**
IDE-25	25.2-25.8Ω x2 = **51Ω**

Figure 5.3: Rs measurement using a Multimeter.

- **By Referring to the mask:** In Figure 5.4, the resistances of the contact pads and the line connecting them to the electrodes are estimated using equation 4.2. Here, resistivity of gold at room temperature is obtained from literature and is ρ_{gold}=2.44e-8. The thickness of the contact pads and the line was about 0.5µm as estimated during the microfabrication process. The variation in the number of electrodes for the IDE causes the line's length to vary; as the number of electrodes increases, the line's length decreases.

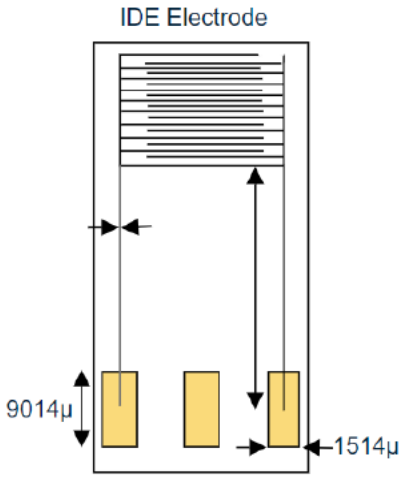

$R_{Contact\ Pad} = (\rho_{Gold}\ L)/A = (\rho_{Gold}\ L)/wt$

$R_{Contact\ Pad} = (2.44e\text{-}8 \times 9014\mu)/(1514\mu \times 0.6\mu)$

$R_{Contact\ Pad} = \underline{0.242\Omega}$

$R_{Line} = \rho_{Gold}\ L/A = \rho_{Gold} L/wt$

$R_{Line(100)} = (2.44e\text{-}8 \times 16046\mu)/(78\mu \times 0.6\mu) = \underline{8.36\Omega}$

$R_{Line(50)} = (2.44e\text{-}8 \times 25046\mu)/(78\mu \times 0.6\mu) = \underline{13.058\Omega}$

$R_{Line(25)} = (2.44e\text{-}8 \times 29546\mu)/(78\mu \times 0.6\mu) = \underline{15.40\Omega}$

$R_S = (R_{Contact\ Pad} + R_{Line}) \times 2$

Electrode	Calculated $R_S(\Omega)$
IDE-100	8.602Ω x2 = **17.204Ω**
IDE-50	13.30Ω x2 = **26.60Ω**
IDE-25	15.642Ω x2 = **31.284Ω**

Figure 5.4: Rs calculated by referring the mask.

By comparing the Direct measurement results with the mask, we can see that there is a ±15Ω difference. This difference is within a reasonable range and serves as a good foundation for the equivalent circuit fitting. Table 5.1 provides a summary of the range of acceptable values.

Electrode	R_s Range
IDE-100	17.2 - 30 Ω
IDE-50	26.6 - 43 Ω
IDE-25	31.2 - 51 Ω

Table 5.1: R_s range for curve fitting.

The values of R_s obtained are very low, and despite determining these values using these methods, in theory it is recommended to ignore R_s as gold IDEs (presented here) exhibit low resistance [37].

As discussed thus far, two types of strips are evaluated using Electrochemical Impedance Spectroscopy (EIS): Interdigitated Electrodes (IDEs) without passivation and IDEs with a passivation layer. The mechanisms involved and the equivalent circuit modeling of these electrodes in both air and aqueous media are examined in the following sections.

5.2 Fitting for IDE without Passivation

In this section, the analysis of Interdigitated Electrodes (IDEs) without a passivation layer in air and aqueous media is presented, along with the modeling of their appropriate equivalent circuits.

In Air

Figure 5.5 shows a First order equivalent circuit for IDE without passivation in air, which consists only of the substrate capacitance C_{sub} and the capacitance of air C_{air}. Since both the capacitances are in parallel, the smaller capacitance C_{air} can be neglected, and the circuit can be simplified to C_g. Any parasitic effects (C_p), which are minimal, are included in C_g as $C_g \gg C_p$. Due to the very low conductivities of air and the substrate, we did not include any resistances between the electrodes. The behavior is purely capacitive and dominated by the capacitance of the substrate.

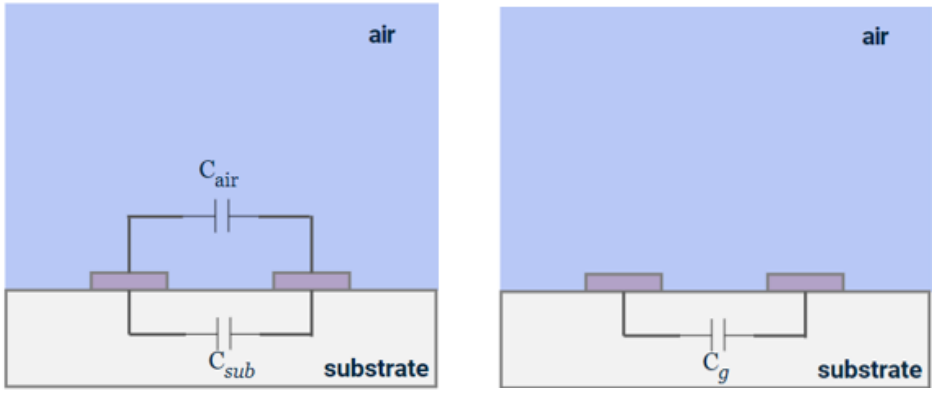

Figure 5.5: First order equivalent circuit of IDE without passivation layer in air. (Right)- further simplified configuration [37].

Figure 5.6: Simplified circuit in air.

The simplified circuit that is used to fit in Zview is shown in Figure 5.6. Zview, a software tool designed for fitting impedance data to equivalent circuit models, was used to determine the capacitance values (C_g) for IDE-25, IDE-50, and IDE-100 based on the model shown in Figure 5.6. This process involves fitting the experimental impedance data to the theoretical model to extract the parameter values that best represent the system's behavior.

IDE without passivation in Air	
Sample	**C_g**
IDE-25	2.07 pF
IDE-50	4.49 pF
IDE-100	8.85 pF

Table 5.2: Capacitance of IDE with varying fingers in air.

In Aqueous media

As discussed in the previous section when faradaic impedance is considered, a charge transfer resistance is present which indicates the presence of redox ions, (usually $[Fe(CN)_6]^{(3/4)}$) in the solution. Figure 5.7 illustrates an equivalent circuit model for an IDE array immersed in a solution containing redox ions. In this model, C_p, C_g and C_{dl} represent the parasitic capacitance (caused by the sensor substrate and electrical cables), the geometric capacitance between the electrode digits (with the aqueous solution acting as the dielectric medium), and the double layer capacitance at the electrode-solution interface, respectively. Additionally, R_{sol}, R_{ct} and R_o denote the solution resistance, the charge transfer resistance (due to oxidation-reduction reactions at the electrode surface), and the ohmic resistance in the wiring and electrode tracking, respectively. In our case, in the absence of redox species in the solution, the equivalent circuit model simplifies since the Faradaic and Warburg impedances can be neglected. A simplified equivalent circuit model for IDEs in a redox-ion-free electrolytic solution is illustrated in Figure 5.9.

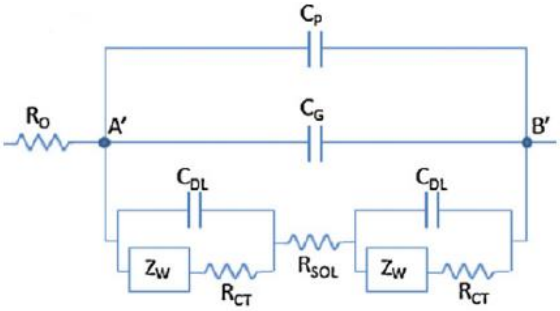

Figure 5.7: Analogous circuit model for IDEs in a solution with redox ions [36].

When a liquid, such as DI water, tap water, low/high concentration saltwater, or PBS solution, is added on top of the electrodes, the circuit complexity increases as depicted in Figure 5.8. The

electrolyte introduces a capacitance C_{sol} and a resistance R_{sol} due to charge mobility in the solution. The double layer capacitance C_{dl} that forms at the electrode-solution interface is considered for both electrodes since they are identical [43]. Instead of using an ideal C_{dl}, a constant phase element (CPE) is often used to model the double layer effect, as described in equation 5.3.

The impedance of a CPE is calculated using equation 5.3,
where $0 < \alpha < 1$. For $\alpha = 1$, it acts like an ideal capacitor and $Y_0 = C$, while for $\alpha = 0$ it becomes a resistor with $Y0 = R$.

$$Z_{CPE} = \frac{1}{Y_0(j\omega)^{\alpha}} \dots\dots\dots\dots (5.3)$$

To simplify the circuit in Figure 5.8 (Left), the parallel capacitances C_{sol} and C_{sub} can be combined into the background capacitance C_g. Here, C_p is incorporated into C_g (assuming $C_g \gg C_p$), and the series combination of two double layer capacitors is represented by C_{dl}. Because of their parallel configuration, C_g is predominantly influenced by the larger solution capacitance C_{sol}. This equivalent circuit is consistent with other literature that discusses electrodes in direct contact with the electrolyte [43], [44].

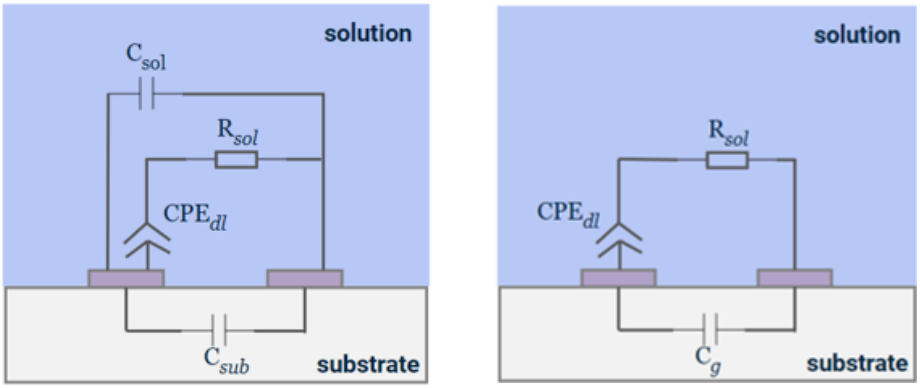

Figure 5.8: First order equivalent circuit of IDE without passivation layer in aqueous media [37]. (Right)- Further simplified configuration.

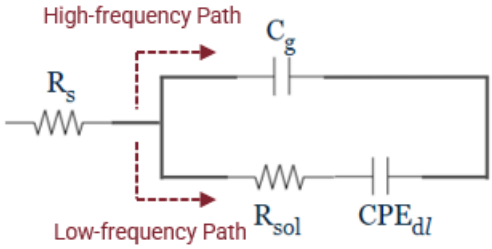

Figure 5.9 : Simplified circuit in solution without redox ions.

In a circuit, the current takes the shortest path to travel. At low frequencies, the impedance of C_g is high, causing the current to predominantly flow through the R_{sol} and C_{dl} path. This is because the impedance of the series combination of R_{sol} and C_{dl} path is relatively low compared to the high

impedance of C_g, where charges are accumulated due to the rate of charging and discharging being low and its behavior is almost like an open circuit. The equivalent impedance in this case is predominantly due to R_{sol}. For even lower frequencies (<100Ω) C_{dl} surpasses R_{sol} and starts actively limiting the current. At high frequencies, the capacitance C_g behaves like a wire and its impedance decreases significantly. The low impedance of C_g shunts the current through its path, effectively bypassing the R_{sol} - C_{dl} path as R_{sol} still contributes to the impedance, making this path less favorable compared to the low impedance of C_g. The equivalent impedance at high frequencies is dominated by C_g. With the increase in solution conductivity, the knee point or relaxation frequency, below which R_{sol} starts to dominate shifts towards higher frequencies, which may imply that for solutions with very high conductivity the R_{sol} may dominate for the entire frequency range.

By using Zview to fit values to the model shown in Figure 5.9, we obtained the values of the circuit elements in various media, depicted in Table 5.3. It is worth noting that the frequencies below 100 Hz are where the contribution of C_{dl} can be visualized.

IDE-100 without passivation layer			
Medium	**C_g (F)**	**R_{sol} (Ω)**	**C_{dl} (F)**
Air	8.85 e-12	1.10 e+09	-
DI Water	8.21 e-12	8.58 e+08	-
Tap water	3.92 e-11	3.14 e+05	-
Low Saltwater Conc.	2.65 e-11	2.38 e+05	-
High Saltwater Conc.	3.25 e-10	3.20 e+01	-
PBS 0.01M	3.52 e-11	3.59 e+01	-

Table 5.3: Values of circuit elements in various media.

5.3 Fitting for IDE with Passivation

In this section, the analysis of Interdigitated Electrodes (IDEs) with a passivation layer in air and aqueous media is presented, along with the modeling of their appropriate equivalent circuits.

In Air

IDEs with a passivation layer, when compared to those without, exhibit enhanced stability and reliability in capacitive behavior and measurement lifespan in air. This enhancement is achieved by shielding the electrodes from environmental influences. Considering the model depicted in Figure 5.5 of IDE without passivation that is subjected to air, in addition to the substrate capacitance, this time, we also have a capacitance due to the passivation (C_{pass}), both operating in parallel. Given their parallel configuration, capacitance C_{pass} can be combined with the substrate capacitance C_{sub} thereby having a measurable effect on the overall capacitance. Again, here we consider C_g as the background capacitance that includes the capacitance of the substrate and any other capacitance that may arise whose effects are small.

Using Zview, we derived the values of C_g for an IDE-100 model with passivation layers including SU-8, silicon nitride, and silicon dioxide of varying thickness.

IDE 100 in Air	
Material	**C_g**
SU-8 (2µm)	8.43 pF
Silicon Nitride (1µm)	8.81 pF
Silicon Nitride (500nm)	8.81 pF
Silicon Dioxide (1µm)	8.53 pF
Silicon Dioxide (500nm)	8.39 pF

Table 5.4: Capacitance variations in IDE-100 with different passivation materials.

In Aqueous media

With the deposition of a passivation layer over IDE, the structure is fully insulated. This insulation alters the behavior of the IDE when it is immersed in a liquid. The passivation layer adds an additional capacitance C_{pass} to the circuit. The model should account for the capacitance and resistance introduced by the liquid.

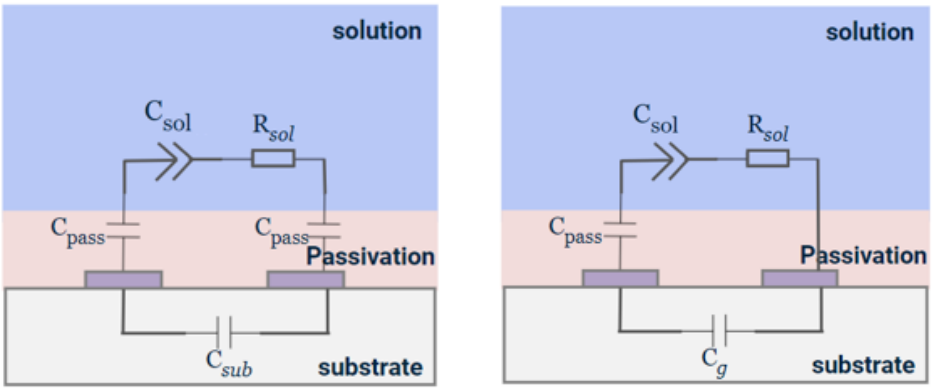

Figure 5.10: First order equivalent circuit of IDE with passivation layer in aqueous media [37]. (Right)- Further simplified configuration.

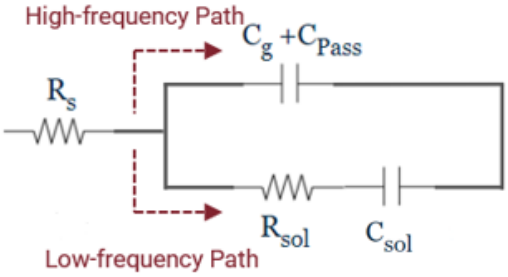

Figure 5.11: Simplified circuit in solution.

The behavior of circuit elements can be seen in different regions. If the graph is divided into three regions- Region1, Region2 and Region3 for low frequency, mid-range frequency and high frequency respectively. We observe the following: At low frequencies, the combined effect of the impedances of C_g and C_{pass} is high, causing the current to predominantly flow through the R_{sol} and C_{sol} path.

This is because the impedance of the series combination of R_{sol} and C_{sol} path is relatively low compared to the high impedance of the path with capacitances whose behavior is almost like an open circuit. Two knee points exist, and on the Bode plot we observe one where the capacitance due to the solution C_{sol} starts to have a significant effect on the impedance. In solutions with low conductivity (more resistive solutions), the impact of C_{sol} can be ignored because the knee point occurs at very low frequencies (<100Hz), which is below our frequency window.

At mid-range frequencies, above the C_{sol} knee point, the effect of R_{sol} becomes dominant. The influence of R_{sol} depends on the conductivity of the medium. As the solution's conductivity increases, the knee point shifts to higher frequencies. This is clearly seen in the phase plot, where the phase shifts from capacitive (-90 degrees) to resistive (zero degrees). When a passivation layer is present, this shift towards zero appears as a sharp peak. As a result, we see R_{sol} dominating for a little while until certain frequencies are reached where the combined capacitive effect of C_g and C_{pass} starts to dominate and that causes the phase to quickly shift back towards -90 degrees. It is interesting to note that, in solutions with higher conductivity, the resistive region is pushed towards higher frequencies.

At high frequencies, the combined effect of the capacitances is very high. The low impedance of C_g / C_{pass} shunts the current through its path, effectively bypassing the R_{sol} - C_{sol} path. From the knee point, we see a rapid shift from the previous resistive effect to a very capacitive effect (-90 degrees). For solutions with higher conductivity this effect may not be seen as the knee point shifts out of the frequency sensing/analysing range. The equivalent impedance at high frequencies is dominated by the combined effect of C_g / C_{pass}.

The impedances for R_{sol} (Z_R), C_{sol} (Z_{Csol}) and Cg (Z_{Cg}) are R_{sol}, $1/j\omega$ C_{sol} and $1/j\omega C_g$ respectively, where ω represents the angular frequency. The total impedance Z_T is given by:

$$Z_T = R_E(Z_T) + j\,\mathrm{Im}(Z_T) \dots\dots\dots\dots (5.4)$$

where the real part of the impedance Re(ZT) is:

$$\mathrm{Re}(Z_T) = \frac{R_{Esol}C_{sol}^2}{(C_g + C_{sol})^2 + (\omega R_{sol}C_gC_{sol})^2} \dots\dots\dots\dots (5.5)$$

and the imaginary part of the impedance Im(ZT) is:

$$I_m(Z_T) = \frac{C_g + C_{sol} + (\omega R_{sol}C_gC_{sol})^2}{\omega(C_g + C_{sol})^2 + (\omega R_{sol}C_gC_{sol})^2} \dots\dots\dots\dots (5.6)$$

By using Zview to fit values to the model shown in Figure 5.11, we obtained the values of the circuit elements in various media.

IDE-100 with SU-8 passivation layer			
Medium	**C_g (F)**	**R_{sol} (Ω)**	**C_{dl} (F)**
Air	8.43 e-12	-	-
DI Water	1.46 e-11	4.46 e+07	-
Tap water	1.46 e-11	7.23 e+04	5.94 e-11
Low Saltwater Conc.	1.26 e-11	1.22 e+05	3.68 e-11
High Saltwater Conc.	-	8.8 e+08	8.21 e-12
PBS 0.01M	-	6.74 e+08	1.46 e-11

Table 5.5: Values of circuit elements in various media. For IDE-100 with SU-8 as a passivation layer.

IDE-100 with Si_3N_4 passivation layer (thickness=1µm)			
Medium	**C_g (F)**	**R_{sol} (Ω)**	**C_{dl} (F)**
Air	8.81 e-12	-	-
DI Water	9.05 e-11	2.35 e+08	-
Tap water	8.13 e-11	2.45 e+05	1.78 e-10
Low Saltwater Conc.	6.65 e-11	4.37 e+04	1.92 e-10
High Saltwater Conc.	-	2.72 e+10	3.02 e-10
PBS 0.01M	-	1.19 e+14	2.54 e-10

Table 5.6 : Values of circuit elements in various media. For IDE-100 with Silicon nitride of thickness 1µm.

IDE-100 with Si_3N_4 passivation layer (thickness=500nm)			
Medium	**C_g (F)**	**R_{sol} (Ω)**	**C_{dl} (F)**
Air	8.22 e-12	-	-
DI Water	1.77 e-10	1.63 e+08	-
Tap water	1.76 e-10	1.79 e+05	3.90 e-10
Low Saltwater Conc.	9.56 e-11	3.43 e+04	3.95 e-10
High Saltwater Conc.	-	2.57 e+13	5.73 e-10
PBS 0.01M	-	5.86 e+13	4.89 e-10

Table 5.7: Values of circuit elements in various media. For IDE-100 with Silicon nitride of thickness 500 nm.

IDE-100 with SiO_2 passivation layer (thickness=1µm)			
Medium	**C_g (F)**	**R_{sol} (Ω)**	**C_{dl} (F)**
Air	8.53 e-12	-	-
DI Water	7.52 e-11	3.49 e+08	-
Tap water	6.80 e-11	3.55 e+05	9.11 e-11
Low Saltwater Conc.	6.98 e-11	6.77 e+04	8.69 e-11
High Saltwater Conc.	-	5.47 e+20	1.69 e-10
PBS 0.01M	-	4.33 e+14	1.59 e-10

Table 5.8: Values of circuit elements in various media. For IDE-100 with Silicon dioxide of thickness 1µm

IDE-100 with SiO_2 passivation layer (thickness=500 nm)			
Medium	**C_g (F)**	**R_{sol} (Ω)**	**C_{dl} (F)**
Air	8.39 e-12	-	-
DI Water	9.83 e-12	1.97 e+08	-
Tap water	9.44 e-11	2.34 e+05	2.04 e-10
Low Saltwater Conc.	8.57 e-11	4.30 e+04	2.13 e-10
High Saltwater Conc.	-	8.79 e+13	3.47 e-10
PBS 0.01M	-	2.93 e+10	1.00 e-10

Table 5.9: Values of circuit elements in various media. For IDE-100 with Silicon dioxide of thickness 500 nm

5.4 Theoretical Capacitance of IDE

Understanding and accurately determining the capacitance of IDEs is crucial for optimizing their performance. Theoretical models provide a foundation for estimating the capacitance based on geometric and material properties, which can then be compared to experimental data obtained through fitting techniques.

The idea here is to model the structure on conformal mapping (CM) techniques used to evaluate closed form expressions for computation of capacitances of IDE, taking into account the capacitances between the fingers as well as the fringing capacitance in the outer fingers.

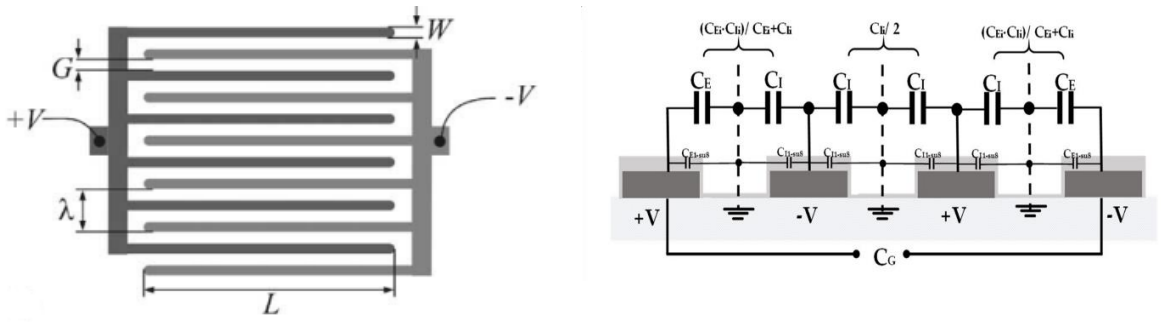

Figure 5.12: (Left)- Layout of the plane of the electrode [45]. (Right)-The equivalent circuit for the evaluation of the static capacitance of a semi-infinite top layer of an IDE containing 4 electrodes [46].

Figure 5.12(Left)- shows a layout of the electrode plane and a schematic diagram of the cross-section of an interdigitated electrode. with two interpenetrating comb electrodes. The gaps between electrodes have a width of G while the fingers have a width of W. Each comb electrode is connected to a fixed potential (either +V or -V) and has a number of fingers of length L. The electrodes, made of gold in general, are deposited on a substrate whose thickness is much greater than the spatial wavelength, λ=2(W+G). The effect of a passivation layer that is deposited over the electrodes is also considered. One can neglect the thickness of the electrodes (50 nm) since they are much thinner than their width, and thus, the electric potential of the electrodes is specified at the interface between the upper and lower half planes. For symmetry reasons, the capacitance can be evaluated as a function of two types of capacitances: (1) C_I — being half the capacitance of one interior electrode relative to the ground potential and (2) C_E — the capacitance of one outer

electrode relative to the ground plane next to it. Figure 5.12(Right)- shows the equivalent electrical circuit for a structure of six electrodes having a semi-infinite layer above the electrode plane. Using network analysis to evaluate the equivalent circuit one finds the total capacitance between the negative and positive electrodes to be equal to:

$$C_{IDE} = (N-3)\frac{C_{I,IDE}}{2} + 2\,\frac{C_{I,IDE}\;C_{E,IDE}}{C_{I,IDE} + C_{E,IDE}} \ldots\ldots\ldots\ldots (5.7)$$

where, N is the number of electrodes.

To determine the capacitance first conformal mapping is employed where, space region of the IDE is mapped onto a parallel plate capacitor geometry for which the capacitance value is known as well as the equipotential lines and the lines of the electric field. Once mapped, and the dimensions of the parallel plate in w plane are known, the capacitance in the x plane can be directly obtained as:

$$C_I = \varepsilon_0 \varepsilon_{rL} \frac{K(k_I)}{K(k'_I)} \ldots\ldots\ldots\ldots (5.8)$$

$$C_E = \varepsilon_0 \varepsilon_{rL} \frac{K(k_E)}{K(k'_E)} \ldots\ldots\ldots\ldots (5.9)$$

where ϵ_r is the relative permittivity of the dielectric layer, L is the length of the electrodes strips, K(k) is the complete elliptic integral of first kind with modulus k and k' the complementary modulus [42].

Using the above equations a typical IDE with a thick substrate of relative permittivity ϵ_s and one sensitive layer of relative permittivity ϵ_1, will have their total capacitances $C_{I,IDE}$ and $C_{E,IDE}$ given by :

$$C_{I,IDE} = C_{I,\text{air}} + C_{I,1} + C_{I,S} \ldots\ldots\ldots\ldots (5.10)$$

$$C_{I,IDE} = \epsilon_0 L\left(\frac{K(k_{I,\infty})}{K(k'_{I,\infty})} + (\epsilon_1 - 1)\frac{K(k_{I,1})}{K(k'_{I,1})} + (\epsilon_1 - 1)\frac{K(k_{I,\infty})}{K(k'_{I,\infty})}\right) \ldots\ldots\ldots\ldots (5.11)$$

$$C_{E,IDE} = C_{E,\text{air}} + C_{E,1} + C_{E,S} \ldots\ldots\ldots\ldots (5.12)$$

$$C_{E,IDE} = \epsilon_0 L\left(\frac{K(k_{E,\infty})}{K(k'_{E,\infty})} + (\epsilon_1 - 1)\frac{K(k_{E,1})}{K(k'_{E,1})} + (\epsilon_1 - 1)\frac{K(k_{E,\infty})}{K(k'_{E,\infty})}\right) \ldots\ldots\ldots\ldots (5.13)$$

In cases where the IDE does not have a passivation layer, that term can be neglected or considered zero. Thus, the total theoretical capacitance is calculated using equation 5.7. The theoretically obtained values are then compared to the values obtained from the equivalent circuit fitting to observe the differences in capacitance, as shown in the following Tables.

Without passivation layer – IN AIR		
Electrode	**Experimental Capacitance**	**Theoretical Capacitance**
IDE-25	2.07 pF	2.1 pF
IDE-50	4.09 pF	4.2 pF
IDE-100	8.85 pF	8.4 pF

Table 5.10: Capacitance of IDE with varying fingers without passivation layer.

IDE 100– IN AIR		
Passivation Type	**Experimental Capacitance**	**Theoretical Capacitance**
No Passivation	8.85 pF	8.4 pF
SU-8	8.43 pF	10 pF
Silicon Dioxide	8.53 pF	12 pF
Silicon Nitride	8.81 pF	13 pF

Table 5.11: Capacitance of IDE with / without passivation layer in air.

In Table 5.10 we observe that the experimental and theoretical capacitance values are closely aligned, indicating that the theoretical models are accurately predicting the capacitance for IDEs with different finger counts. As the number of fingers increases from 25 to 100, both the experimental and theoretical capacitance values increase, demonstrating a consistent trend. For the IDE-100 without passivation, the experimental capacitance (8.8 pF) closely matches the theoretical value (8.4 pF). For IDEs with passivation layers, the theoretical capacitance values are always higher than the experimental values. This suggests that the model might be overestimating the dielectric properties of the passivation layers. This model does not take into account the thickness of the passivation layers and works only for IDEs in air.

Chapter 6

Longevity Test

For electrodes to transition successfully from research prototypes to clinical tools, they must undergo extensive pre-clinical testing to confirm their long-term safety and effectiveness. A major concern is the stability of these electrodes once implanted into the body, where they encounter a hostile environment exacerbated by inflammatory responses. To ensure reliable performance, electrodes must withstand various forms of degradation, including corrosion, delamination, swelling, dissolution, and mechanical stress, all while being subjected to continuous electrical stimulation [47]. Ensuring long-term reliability and stability is vital for neuroscience applications such as investigating brain diseases, applying deep brain stimulation, and treating Parkinson's disease, as these fields heavily rely on chronic studies [48].

Creating electrodes that meet these rigorous requirements is challenging, with device failure frequently being the primary issue in neural implant surgeries. This challenge highlights the necessity of developing advanced materials and fabrication methods that can endure the biological environment's demanding conditions. Consequently, studying the aging of interdigitated electrode (IDE) samples is essential. By examining how these electrodes deteriorate over time in conditions that mimic the human body, researchers can gain critical insights into their long-term durability and improve the design of future neural implants [49], [50].

The implants must operate continuously for 10 years or more, collecting data 24/7 for at least 10 hours daily. Ideally, the implant should function seamlessly until it is no longer needed. To assess the long-term durability and performance of the passivation layer, samples are immersed in a solution of 0.01M PBS and subjected to controlled heating. Using a 0.01M PBS solution closely mimics the degradation conditions experienced by the device in vivo.

Increasing the temperature above 37°C accelerates the aging process of the samples. A reliable aging setup not only replicates the natural environment to ensure consistent data collection from living test subjects but also allows for observing and predicting sample progression over extended periods in a short time. To assess the impact of IDE on the longevity of its passivation material within the human body, samples were exposed to PBS at approximately 80°C for long periods of time. The Arrhenius reaction rate function is useful for estimating the device's lifetime at body temperature based on the mean time to failure observed during accelerated aging tests [12]. According to the Arrhenius law, the aging rate doubles for every 10°C rise in temperature. This accelerated aging process, following the Arrhenius law, increases the aging rate by 16 times, aiding in predicting long-term performance evolution of the samples. Hence, the elevated temperature environment simulated the aging process akin to conditions in the human brain.

Data acquisition was performed using an Analog Discovery 2 by Digilent and a custom-made multiplexer. This setup enabled simultaneous data collection across four different ports, ensuring continuous and automated data storage. It aimed to comprehend the aging dynamics and the influence of IDE on material stability. Impedance spectroscopy provided insights into electrical

properties like resistance and capacitance, facilitating the observation of material changes over time.

In this chapter, the focus will be on IDE with and without a passivation layer and its evolution with time to predict performance in chronic applications. Here, IDEs covered with various passivation materials were put to the test and the results were compared.

6.1 Test Setup and Conditions

- **Selection of Samples**

  Before the longevity test, the samples (IDE structures) were tested using the Impedance Analyzer HP-4194A as described in section 4.2 to have a reference of the integrity of the samples' performance. To begin with, some samples were chosen. The samples included IDE-100 without passivation, IDE-100 with SU-8 passivation, IDE-100 with 1 m thick silicon nitride passivation, IDE-100 with 1 m thick silicon dioxide passivation, and IDE-100 with 500 nm thick silicon nitride passivation (IDE-100 without passivation underwent aging in a separate test; however, its results are included here for analysis purposes.)

- **Sample preparation and setup**

  The samples employed for the longevity test were first fitted with a wire via copper tape and to ensure insulation, this assembly was then covered with Kapton tape as described in a previous section. 3D caps made of resin were fabricated via 3D printing and the samples' contact parts were inserted into them. Then the gaps between the electrodes and the resin caps were filled with EXPOXY Glue and left overnight for them to turn solid. This was done so that the contacts of the electrodes were protected and didn't have any liquid seeping into them. The prepared samples were put in a thick glass jar filled with PBS 0.01M and the connecting wires were passed through some small openings made through the caps. PDMS was then poured into the gap so that the whole contact area was encapsulated with PDMS for better hermiticity, this is illustrated in Figure 6.1. This PDMS is typically made in the cleanroom environment by mixing about 40g of liquid silicone elastomer base (2 parts) and a curing agent (1 part) with the ratio being 2:1. The PDMS base and curing agent must be mixed thoroughly to ensure a homogenous mixture and allowed to set for a little more than 24 hours in ambient temperature. A thermocouple was placed in the center of the sturdy glass jar to monitor the temperature throughout each stage of the process.

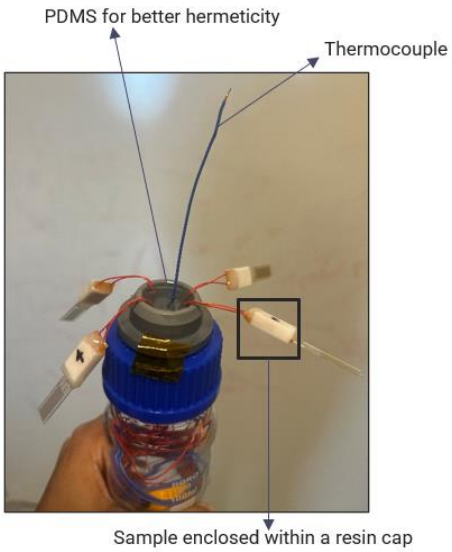

Figure 6.1: Samples prepared for the longevity test in a cleanroom environment.

6.2 Primary Experimental Protocol

The first step was always testing the samples using the HP4194A Impedance Analyzer to have a reference of the integrity of the samples' performance. That involves, conducting the experiment without applying any heat, in ambient temperature. Following were the parameters of the aging test bench: Fmin=100Hz, Fmax=15MHz, Step=20, Vmax=1.0, Avg=20. The initial values of measurement is as shown in Figure 6.2.

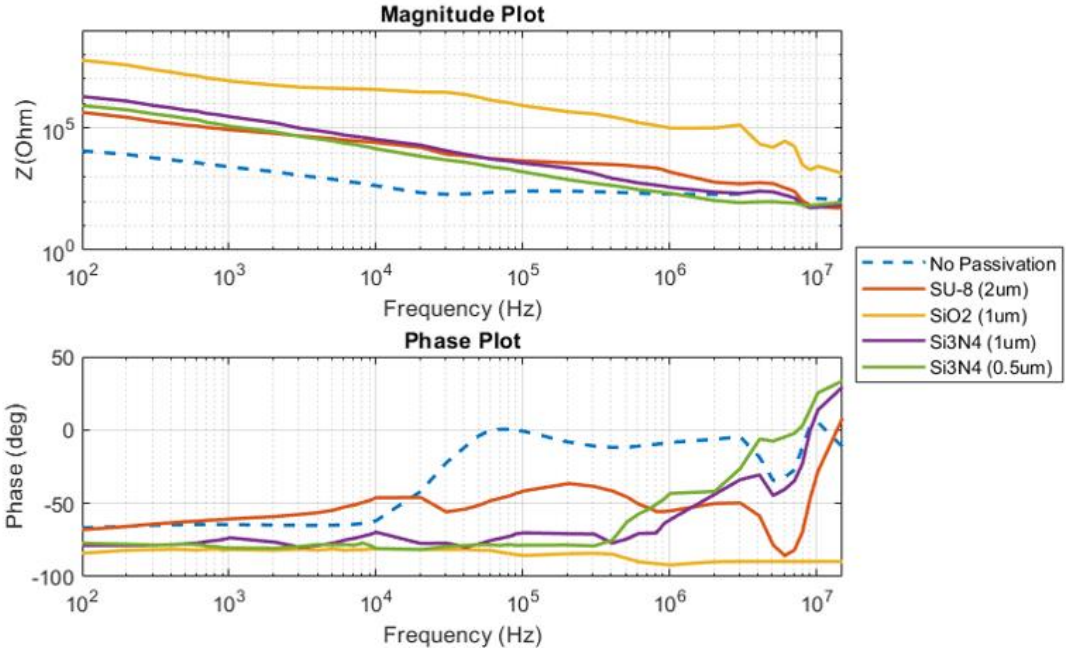

Figure 6.2: Initial values of measurements of the IDE's, before aging.

Figure 6.3 illustrates the experimental setup for longevity testing. The system is housed within a Styrofoam box, which is enclosed on three sides to minimize air disturbance to the experimental

setup. The box can be fully closed to minimize exposure to air currents, drafts, and potential displacement from external movements.

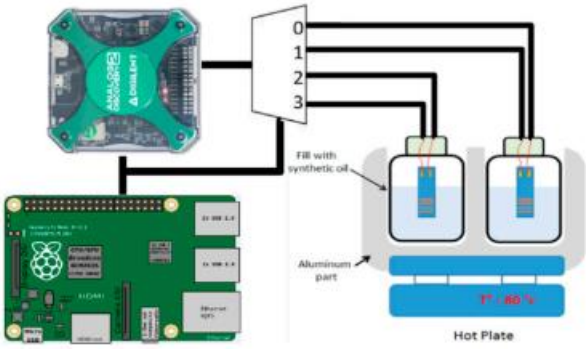

Figure 6.3: Schematic representation of the test setup [10].

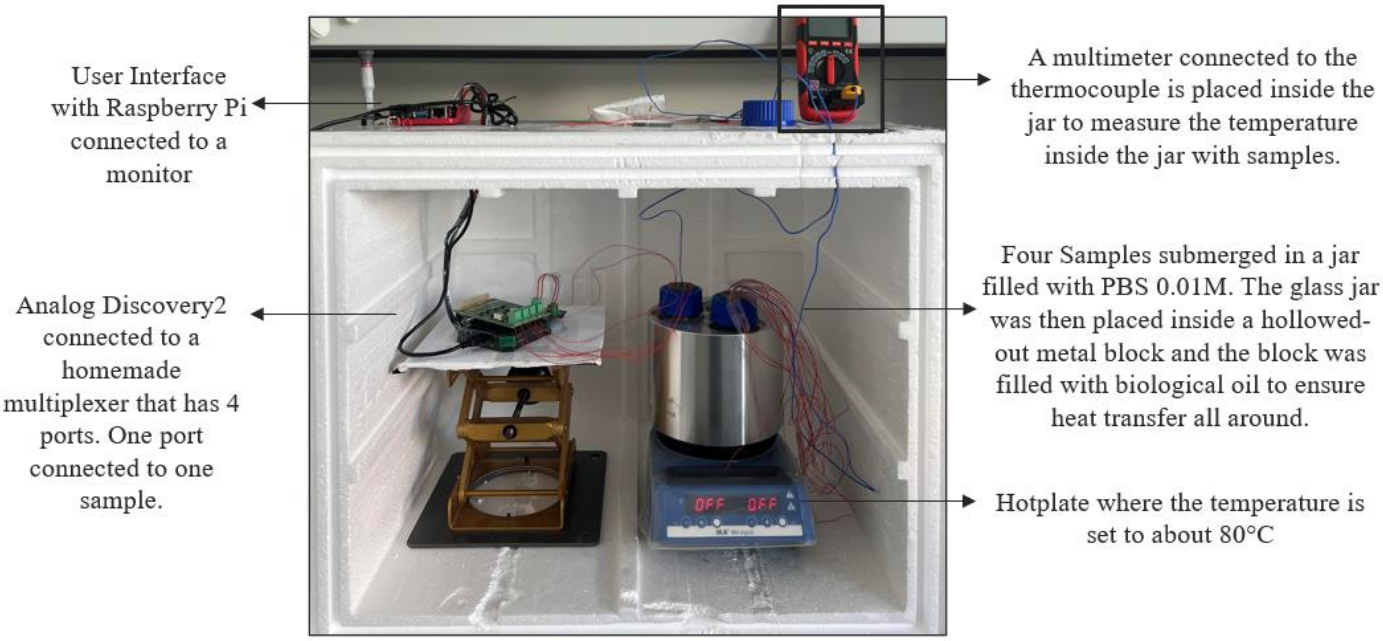

Figure 6.4: System placed inside a Styrofoam box that is fully enclosed in real time.

Once initial measurements were taken, the prepared samples, along with a thermocouple, were placed inside a glass jar. This jar was then placed within a hollowed-out metal block filled with biological oil to ensure uniform heat distribution. The metal block was positioned on a hotplate set to maintain a temperature of 80°C, resulting in an internal experimental environment temperature of 78°C. A temperature display connected to the thermocouple monitored and ensured constant internal temperature.

This method ensured that connected strips displayed stable results over time without drifting due to connectivity issues during experiments. The samples were connected to the four ports of a homemade multiplexer along with an AD2 device. A computer monitor was linked to gather data

from the Raspberry Pi and analyze it further. Results were recorded over a period of 4 weeks, under continuous heating conditions, accelerating the aging process of the samples by 16 times.

6.3 Results from the aging test bench

The sample was put on continuous heat for four weeks (total of 24 days) and hence the aging process of the samples is accelerated by 16 times, as per the Arrhenius law (cite Arrhenius law), which means the samples have suffered an aging effect equivalent to 64 weeks (64 weeks= 1.23 years).

As seen from these results, the results are not stable but aren't as expected.

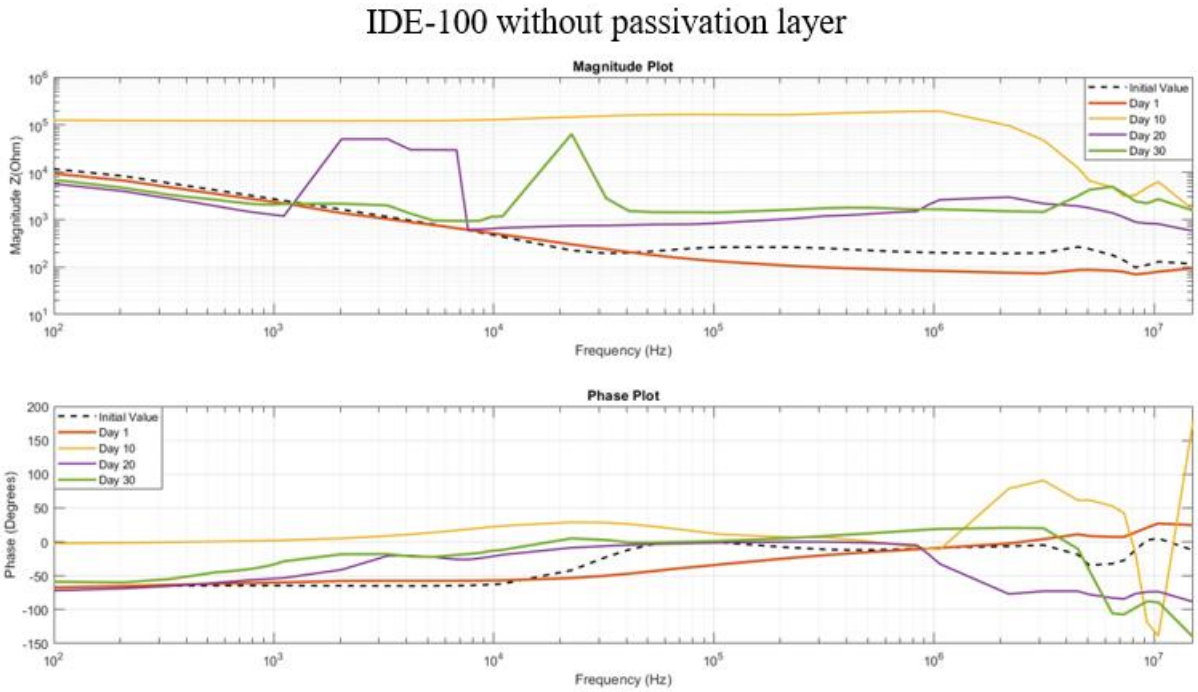

Figure 6.5: Data acquisition using AD2 from the sample without passivation subjected to heating.

The results indicate that the presence of a passivation layer significantly stabilizes the material during four weeks of constant heating. This is evident from the reduced variations observed in the material's evolution compared to the sample without passivation. The data clearly demonstrate the effectiveness of passivation in maintaining the material's integrity and reducing changes over prolonged exposure to heat. This highlights the critical role of passivation in enhancing thermal stability and preserving the material's properties under sustained heating conditions.

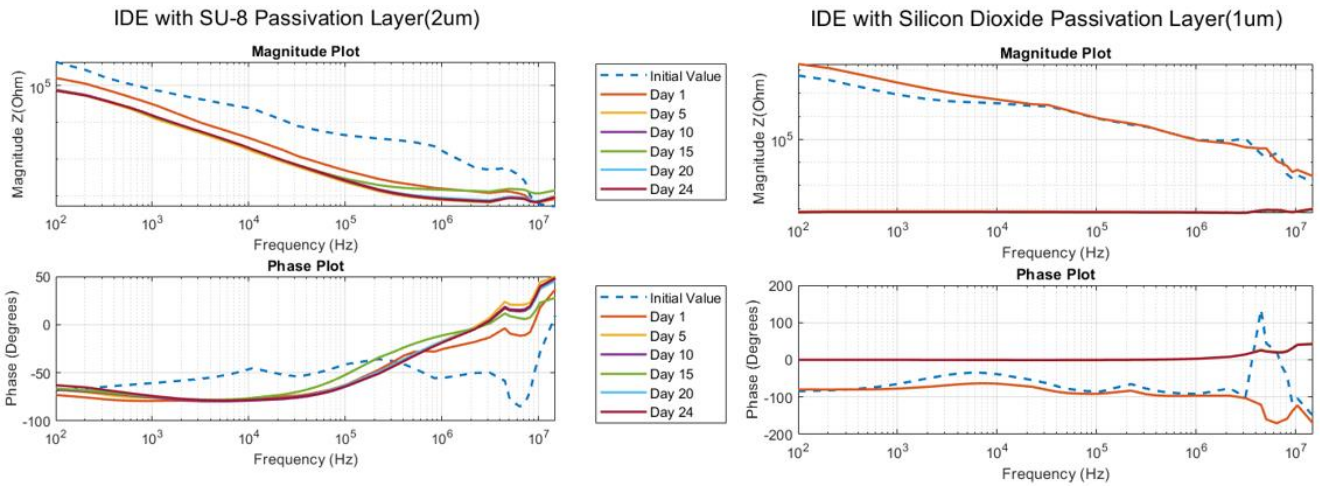

Figure 6.6 : Data acquisition using AD2 from the sample with passivation subjected to heating.

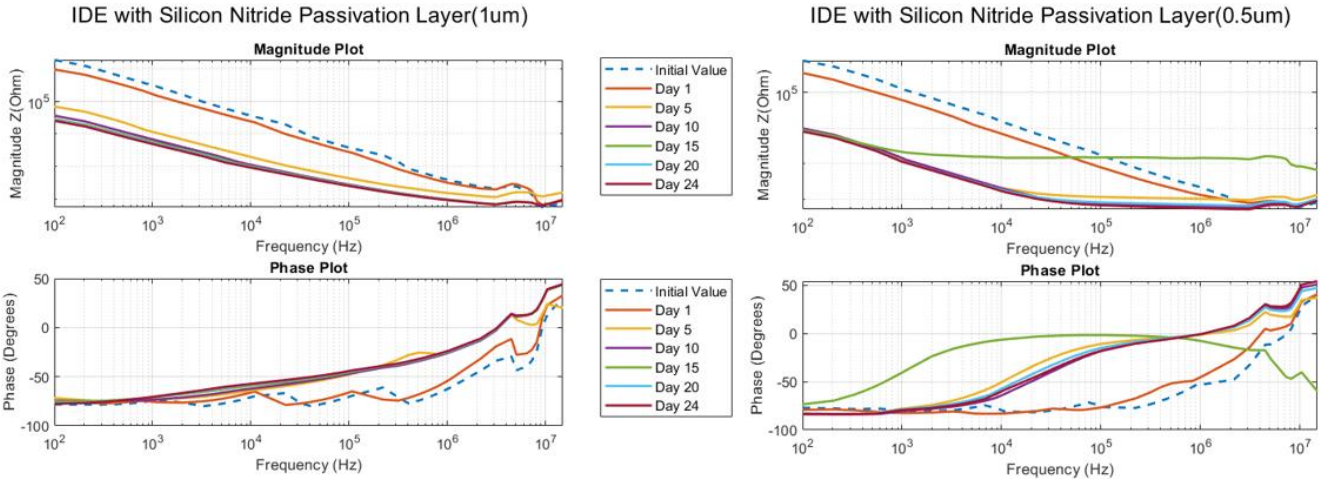

Figure 6.7: Data acquisition using AD2 from the sample with passivation subjected to heating.

In addition to this, it was noted that the sample with silicon dioxide passivation began exhibiting resistive behavior starting from the second day of the aging experiment. Prior to this, the sample had demonstrated consistent capacitive behavior during the initial measurements. The change in behavior from capacitive to resistive after immersion in PBS solution may stem from various factors related to the sealing integrity and contact insulation during sample preparation. It could be primarily attributed to imperfections in the sealing process or unintended shorting of contacts during sample preparation.

6.4 Post-Aging Analysis

Impedance measurements serve as a diagnostic tool for identifying electrode failure modes, establishing EIS as one of the most prevalent tests for evaluating electrode performance. While EIS serves as a tool to detect electrical failures within the device, additional analytical methods are required to support and verify the data. Surface analysis of the electrode arrays before and after stimulation offers insights into the quality and durability of the electrode surfaces. Surface characteristics that can be observed include mechanical wear, metal dissolution, contamination, and corrosion. AFM is frequently employed to assess surface topography and detect anomalies such as insufficient insulation adhesion or material cracks. For deeper analysis of the failure mechanisms affecting thin-film electrodes, scanning electron microscopy (SEM) can visualize structural alterations on the electrode surface, such as delamination and cracking [12].

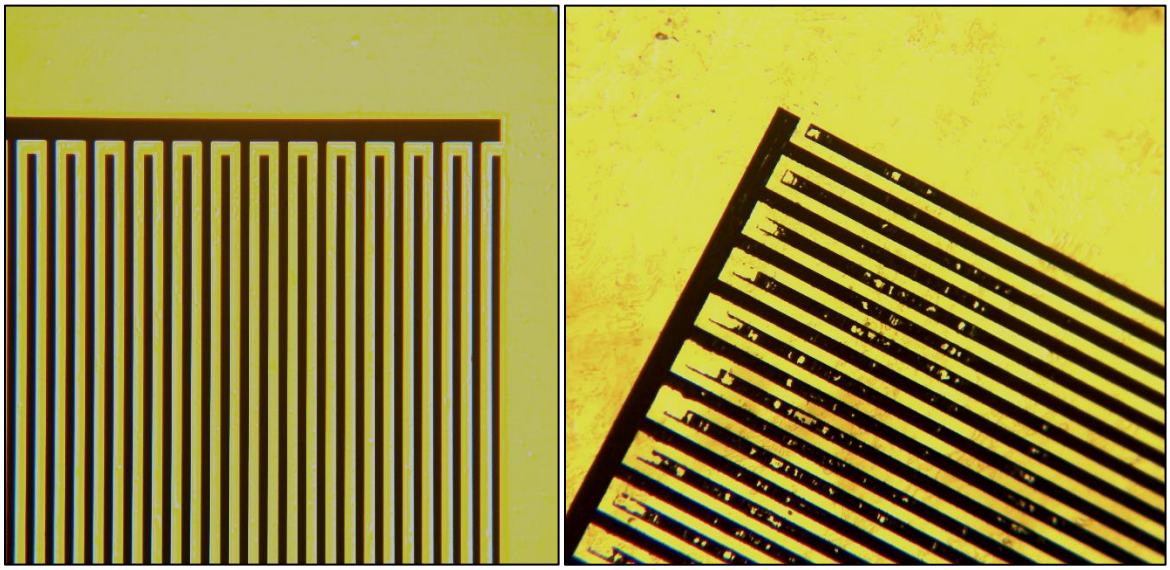

Figure 6.8 : Microscopic observation of IDE's surface before (Left) and After (Right) aging.

Post-aging analysis involves removing the samples from heating and measuring them using an impedance analyser. The figures illustrate the outcome after aging in comparison to before aging.

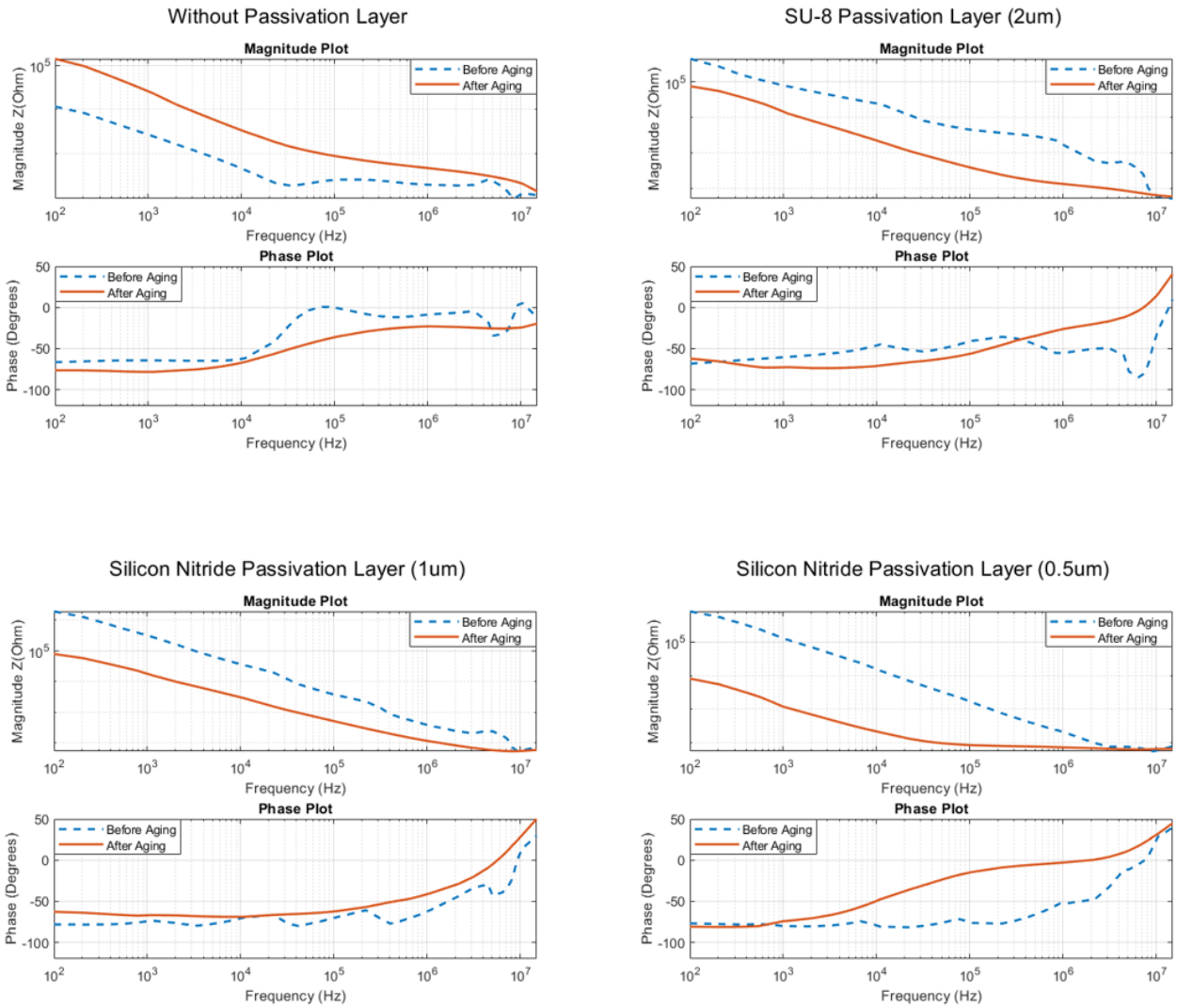

Figure 6.9: Comparison of Results Before and After Aging.

For IDE without passivation layer

An increase in impedance was noted, reflecting a rise in resistance values as evident from the phase plot. Elevated impedance values typically signal electrode damage and contact corrosion. The lack of a passivation layer renders the electrode more vulnerable to corrosion, leading to the formation of non-conductive corrosion products. Additionally, non-conductive molecules from the environment have adhered to the electrode surface.

For IDE with a passivation layer

The behavior observed in IDEs with passivation differed significantly from those without. Following aging, there was a notable decrease in impedance, indicating reduced capacitance compared to initial measurements. According to Kozai et al., low impedance values are characteristic of insulation failures, a trend they observed in correlation with the breakdown of silicon oxide insulation [12].

The percentage difference in impedance values post-aging can be determined by comparing them to pre-aging measurements. This change is illustrated in Table 6.1. Additionally, changes in capacitance can be determined by fitting the aged measurements to an equivalent circuit model. The updated values following ageing are presented in Table 6.2 and Table 6.3.

Impedance Modulus of IDE-100 at 1kHz			
Sample type	**Before Aging**	**After Aging**	**% of Change at 1kHz**
No Passivation	2523.67	23551.86	**733.305 %**
SU-8 (2µm)	75042	12893.52	**82.82 %**
Silicon Nitride (1µm)	286743.03	16238.75	**94.38 %**
Silicon Nitride (0.5µm)	116684.01	1103.83	**99.05 %**

Table 6.1: Percentage change in impedance post aging.

For the IDE without a passivation, the significant increase in impedance indicates substantial degradation, due to direct exposure of the electrodes to environmental factors. The silicon nitride layers exhibit significant degradation over time, with the thicker layer showing a substantial decrease in impedance and the thinner layer experiencing almost a complete drop in impedance. This comparison suggests that while both thicknesses of silicon nitride passivation are prone to degradation, the thinner layer is less effective and degrades more severely. The thicker silicon nitride layer, although also degrading, maintains a higher impedance than the thinner layer, indicating it to be slightly better. Among the aged samples, the sample with SU-8 passivation shows a relatively modest percentage change in impedance at 1kHz, with an 82.82% increase. This smaller change suggests that the sample with SU-8 is more stable and durable in comparison with the other samples.

Capacitance of IDE-100 in Air		
Sample type	**Before Aging (F)**	**After Aging (F)**
No Passivation	8.85 e-12	2.30 e-15
SU-8 (2µm)	8.43 e-12	2.83 e-11
Silicon Nitride (1µm)	8.81 e-12	3.66 e-11
Silicon Nitride (0.5µm)	8.22 e-12	3.36 e-11

Table 6.2 : Capacitance and resistance values of IDE in Air before and after aging.

Table 6.2 presents the capacitance measurements of Interdigitated Electrodes with various passivation materials, both before and after aging, in air. No passivation shows a decrease in capacitance by 3 orders of magnitude, indicating poor performance and stability under aging conditions. This is also reflected in Table 6.3, where, with no passivation, the resistance has increased significantly after aging. The data clearly demonstrates the beneficial effects of using passivation layers which show an increase in capacitance, with Silicon nitride of 1µm thickness exhibiting the highest capacitance among the aged samples. With a passivation layer, we observe

decreased resistance due to potential degradation of the passivation layer, leading to the formation of conductive paths.

Capacitance of IDE-100 in PBS				
Sample type	**Before Aging (F)**		**After Aging (F)**	
	C(F)	**R_{sol} (Ω)**	**C(F)**	**R_{sol} (Ω)**
No Passivation	3.52 e-11	35.91	8.99 e-07	9.94 e+12
SU-8 (2µm)	1.46 e-11	6.74 e+08	2.97 e-09	68.42
Silicon Nitride (1µm)	2.54 e-10	9.60 e+11	1.66 e-09	40.52
Silicon Nitride (0.5µm)	4.89 e-10	5.8 e+13	7.61 e-08	53.04

Table 6.3: Capacitance and resistance values of IDE in PBS before and after ageing.

Chapter 7

Conclusion and Personal Statement

In conclusion, this study undertook a comprehensive analysis of Interdigitated Electrodes (IDEs) and their behavior. Fabrication of IDEs, both with and without passivation using photolithographic processes in a cleanroom environment, was followed by experimental and simulated analyses in various mediums: initially in air, and subsequently in aqueous solutions (DI water, tap water, low salt, high salt, PBS 0.01M), to assess IDE performance. Equivalent circuits were designed based on impedance data obtained from experiments, enabling the identification of key parameters such as geometric capacitance (C_g), double-layer capacitance (C_{dl}), capacitance due to the solution (C_{sol}), and solution resistance (R_{sol}), thereby distinguishing the behavior of different IDE configurations. Additionally, longevity tests were conducted on all IDEs to evaluate their performance before and after aging, providing insights into their durability and long-term functionality.

During the fabrication process, IDEs without passivation and with various passivation layers (SU-8, SiO_2, Si_3N_4) of varying thicknesses (2um, 1um, 0.5um) were successfully fabricated. A comparison between experimental and theoretical analyses indicated that simulations did not fully account for the non-ideal behavior of capacitance and other environmental factors.

Based on detailed experimental and Finite Element Method (FEM) analyses presented in Chapter 4, several conclusions were drawn: IDEs were modeled with three configurations—IDE-25, IDE-50, and IDE-100—based on the number of electrode pairs. It was observed that impedance was significantly influenced by parameters such as relative permittivity (ε_r) and electric conductivity (σ), where higher ε_r decreased impedance and higher σ affected resistive behavior. Simulated Bode plots for IDEs without passivation exhibited distinct capacitive behavior in air and varied resistive and capacitive behaviors in aqueous solutions depending on conductivity. Passivated IDEs predominantly showed capacitive behavior, with impedance slope variations influenced by passivation material thickness and properties.

Experimental analysis involved testing fabricated IDE samples using an HP 4194A impedance analyzer across a frequency range of 100 Hz to 20 MHz. Experimental Bode plots confirmed general simulation trends but highlighted additional complexities such as surface roughness, impurities, and measurement noise, particularly affecting low-frequency regions likely due to real-world imperfections and parasitic effects.

Throughout this thesis, the fitting process was explored using software tools including ZView, EC Lab, and EIS Spectrum Analyzer. These tools facilitated the extraction of circuit parameters through iterative adjustments based on experimental impedance spectra. Chapter 5 elaborated on how this iterative fitting approach was crucial for establishing relationships between the physical and electrical properties of IDEs and their surrounding environments.

Key findings included the characterization of IDEs without passivation layers in both air and aqueous mediums, where impedance spectra primarily reflected substrate capacitances and

solution resistances. The influence of passivation layers on IDE behavior was also investigated, revealing that besides substrate capacitance (C_g), passivation layers introduced additional capacitance (C_{pass}), collectively influencing overall system capacitance. Impedance spectroscopy using tools like ZView enabled quantification of capacitance contributions from different passivation materials, showcasing variations in capacitance across various IDE configurations.
Theoretical models based on conformal mapping techniques provided a robust framework for estimating IDE capacitance, considering geometric parameters and material properties. Comparisons between theoretical evaluations and experimental data demonstrated close agreement across different IDE designs and types of passivation layers. In air, IDEs without passivation exhibited capacitance values closely aligned with theoretical calculations, validating the model's accuracy in predicting electrostatic behavior under ideal conditions.

In conclusion, this thesis underscores the critical role of passivation layers in enhancing IDE durability and reliability under challenging biological conditions, as extensively discussed in Chapter 6. Simulated accelerated aging conditions enabled predictions of long-term performance trends and identification of key factors influencing electrode stability. Results highlighted significant differences in impedance and capacitance between IDEs with and without passivation layers post-aging. IDEs lacking passivation layers exhibited substantial impedance increases, indicative of potential electrode damage and corrosion exacerbated by the absence of protective coatings. Conversely, IDEs with passivation layers demonstrated decreased impedance post-aging, often suggesting reduced capacitance possibly due to insulation failures within the passivation material itself. Protective layers such as SU-8, silicon nitride, and silicon dioxide effectively mitigate corrosion and enhance long-term stability.

Future Work

- For a comprehensive analysis, examining behavior at frequencies below 100Hz is beneficial due to the significant impact of Cdl/Csol at very low frequencies. Additionally, analyzing frequencies above 40MHz is important, especially in PBS solution, which is of particular interest as it mimics device's performance in vivo.

- For better comparison purposes, it would be beneficial to standardize the passivation thickness across all samples.

- Previous work at ESIEE Paris has already established diamond as the optimal passivation material. With a robust COMSOL model developed in this thesis, future work could further optimize the model to analyze its effectiveness.

Bibliography

[1] Y. Lu *et al.*, "Ultralow Impedance Graphene Microelectrodes with High Optical Transparency for Simultaneous Deep Two-Photon Imaging in Transgenic Mice," *Adv. Funct. Mater.*, vol. 28, no. 31, p. 1800002, 2018, doi: 10.1002/adfm.201800002.

[2] C. Hassler, T. Boretius, and T. Stieglitz, "Polymers for Neural Implants," *J. Polym. Sci. Part B Polym. Phys.*, vol. 49, pp. 18–33, Jan. 2011, doi: 10.1002/polb.22169.

[3] S. F. Cogan, "Neural stimulation and recording electrodes," *Annu. Rev. Biomed. Eng.*, vol. 10, pp. 275–309, 2008, doi: 10.1146/annurev.bioeng.10.061807.160518.

[4] W. Yang, Y. Gong, and W. Li, "A Review: Electrode and Packaging Materials for Neurophysiology Recording Implants," *Front. Bioeng. Biotechnol.*, vol. 8, p. 622923, Jan. 2021, doi: 10.3389/fbioe.2020.622923.

[5] J. Lee, "Neural recording and stimulation using wireless networks of microimplants | Request PDF." Accessed: Nov. 21, 2023. [Online]. Available: https://www.researchgate.net/publication/353856276_Neural_recording_and_stimulation_using_wireless_networks_of_microimplants

[6] "Pitt Medical Neuroscience | Neurophysiology and Synaptic Transmission," *The neuron*.

[7] H. An, K. Bai, Y. Yi, H. An, K. Bai, and Y. Yi, "The Roadmap to Realize Memristive Three-Dimensional Neuromorphic Computing System," in *Advances in Memristor Neural Networks - Modeling and Applications*, IntechOpen, 2018. doi: 10.5772/intechopen.78986.

[8] "Action Potential - The Definitive Guide | Biology Dictionary." Accessed: Oct. 25, 2023. [Online]. Available: https://biologydictionary.net/action-potential/

[9] "The NEURODIAM project – NEURODIAM." Accessed: Oct. 20, 2023. [Online]. Available: https://www.neurodiam.eu/about-us/

[10] J. Roy *et al.*, "Stability Study of Synthetic Diamond Using a Thermally Controlled Biological Environment: Application towards Long-Lasting Neural Prostheses," *Sensors*, vol. 24, no. 11, Art. no. 11, Jan. 2024, doi: 10.3390/s24113619.

[11] Umme Sarah Tabassum, "Comparison of Electrodes with Conventional, and Non-Conventional Biomaterials to Novel Full Diamond Electrodes for Biomedical Applications," Université Gustave Eiffel, 2023.

[12] P. Oldroyd and G. G. Malliaras, "Achieving long-term stability of thin-film electrodes for neurostimulation," *Acta Biomater.*, vol. 139, pp. 65–81, Feb. 2022, doi: 10.1016/j.actbio.2021.05.004.

[13] D. T. Brocker and W. M. Grill, "Principles of electrical stimulation of neural tissue," *Handb. Clin. Neurol.*, vol. 116, pp. 3–18, 2013, doi: 10.1016/B978-0-444-53497-2.00001-2.

[14] E. S. Vikulova *et al.*, "Application of Biocompatible Noble Metal Film Materials to Medical Implants: TiNi Surface Modification," *Coatings*, vol. 13, no. 2, Art. no. 2, Feb. 2023, doi: 10.3390/coatings13020222.

[15] "Passivation (chemistry)," *Wikipedia*. Jun. 17, 2024. Accessed: Oct. 20, 2023. [Online]. Available: https://en.wikipedia.org/w/index.php?title=Passivation_(chemistry)&oldid=1229545223

[16] "Passivation," *Wikipédia*. Apr. 07, 2024. Accessed: Oct. 20, 2023. [Online]. Available: https://fr.wikipedia.org/w/index.php?title=Passivation&oldid=214058750

[17] J. C. Barrese *et al.*, "Failure mode analysis of silicon-based intracortical microelectrode arrays in non-human primates," *J. Neural Eng.*, vol. 10, no. 6, p. 066014, Dec. 2013, doi: 10.1088/1741-2560/10/6/066014.
[18] A. Domínguez-Bajo *et al.*, "Nanostructured gold electrodes promote neural maturation and network connectivity," *Biomaterials*, vol. 279, p. 121186, Dec. 2021, doi: 10.1016/j.biomaterials.2021.121186.
[19] M. Tijero *et al.*, "SU-8 microprobe with microelectrodes for monitoring electrical impedance in living tissues," *Biosens. Bioelectron.*, vol. 24, no. 8, pp. 2410–2416, Apr. 2009, doi: 10.1016/j.bios.2008.12.019.
[20] Zarchi Meysam, Shahrokh Ahangarani, and Zare Maryam, "Properties of Silicon Dioxide Film Deposited By PECVD at Low Temperature/Pressure," *Metall. Mater. Eng.*, vol. 20, pp. 89–96, Jul. 2014, doi: 10.5937/metmateng1402089M.
[21] L. Liu, W. Liu, N. Cao, and C. Cai, "Study on The Performance of PECVD Silicon Nitride Thin Films," *Def. Technol.*, vol. 9, no. 2, pp. 121–126, Jun. 2013, doi: 10.1016/j.dt.2013.10.004.
[22] L. Q. Jun, G. W. Bin Djaswadi, H. F. Bin Hawari, and M. A. B Zakariya, "Simulation of Interdigitated Electrodes (IDEs) Geometry Using COMSOL Multiphysics," *2018 Int. Conf. Intell. Adv. Syst. ICIAS*, pp. 1–6, Aug. 2018, doi: 10.1109/ICIAS.2018.8540599.
[23] S. MacKay, P. Hermansen, D. Wishart, and J. Chen, "Simulations of Interdigitated Electrode Interactions with Gold Nanoparticles for Impedance-Based Biosensing Applications," *Sensors*, vol. 15, no. 9, pp. 22192–22208, Sep. 2015, doi: 10.3390/s150922192.
[24] Mohd Syaifudin Abdul Rahman, S.C. Mukhopadhyay, and Pak-Lam Yu, "Novel Planar Interdigital Sensors," in *Novel Sensors for Food Inspection: Modelling, Fabrication and Experimentation*, pp. 11–35. [Online]. Available: https://www.researchgate.net/publication/278692946_Novel_Planar_Interdigital_Sensors
[25] M. R. R. Khan and S.-W. Kang, "Highly Sensitive Multi-Channel IDC Sensor Array for Low Concentration Taste Detection," *Sensors*, vol. 15, no. 6, Art. no. 6, Jun. 2015, doi: 10.3390/s150613201.
[26] S. Saukko and V. Lantto, "Influence of electrode material on properties of SnO2-based gas sensor," *Thin Solid Films*, vol. 436, no. 1, pp. 137–140, Jul. 2003, doi: 10.1016/S0040-6090(03)00509-1.
[27] T. Kremers, M. Tintelott, V. Pachauri, X. T. Vu, S. Ingebrandt, and U. Schnakenberg, "Microelectrode Combinations of Gold and Polypyrrole Enable Highly Stable Two-electrode Electrochemical Impedance Spectroscopy Measurements under Turbulent Flow Conditions," *Electroanalysis*, vol. 33, no. 1, pp. 197–207, 2021, doi: 10.1002/elan.202060105.
[28] J. R. Macdonald and W. B. Johnson, "Fundamentals of Impedance Spectroscopy," in *Impedance Spectroscopy*, John Wiley & Sons, Ltd, 2018, pp. 1–20. doi: 10.1002/9781119381860.ch1.
[29] E. von Hauff and D. Klotz, "Impedance spectroscopy for perovskite solar cells: characterisation, analysis, and diagnosis," *J. Mater. Chem. C*, vol. 10, no. 2, pp. 742–761, Jan. 2022, doi: 10.1039/D1TC04727B.
[30] "Electrochemcal Impedance Spectroscopy (EIS) Basics – Pine Research Instrumentation Store." Accessed: Oct. 23, 2023. [Online]. Available: https://pineresearch.com/shop/kb/theory/eis%02theory/eis-basics/
[31] E. Barsoukov and J. R. Macdonald, "Impedance Spectroscopy: Theory, Experiment, and Applications, 3rd Edition | Wiley," Wiley.com. Accessed: Nov. 05, 2023. [Online].

Available: https://www.wiley.com/en-es/Impedance+Spectroscopy%3A+Theory%2C+Experiment%2C+and+Applications%2C+3rd+Edition-p-9781119074083

[32] P. Kassanos, "Bioimpedance Sensors: A Tutorial," *IEEE Sens. J.*, vol. 21, no. 20, pp. 22190–22219, Oct. 2021, doi: 10.1109/JSEN.2021.3110283.

[33] J. Shepard, "What does electrochemical impedance spectroscopy have to do with Li-ion health?"

[34] M. Ibrahim, J. Claudel, D. Kourtiche, M. Nadi, F. Montaigne, and G. Lengaigne, "Optimization of planar interdigitated electrode array for bioimpedance spectroscopy restriction of the number of electrodes," in *2011 Fifth International Conference on Sensing Technology*, Nov. 2011, pp. 612–616. doi: 10.1109/ICSensT.2011.6137055.

[35] A. Bratov, S. Brosel-Oliu, and N. Abramova, "Label-Free Impedimetric Biosensing Using 3D Interdigitated Electrodes," M. J. Schöning and A. Poghossian, Eds., in Springer Series on Chemical Sensors and Biosensors, vol. 16. Cham: Springer International Publishing, 2017, pp. 179–198. doi: 10.1007/5346_2017_7.

[36] S. Rana, R. H. Page, and C. J. McNeil, "Impedance spectra analysis to characterize interdigitated electrodes as electrochemical sensors," *Electrochimica Acta*, vol. 56, no. 24, pp. 8559–8563, Oct. 2011, doi: 10.1016/j.electacta.2011.07.055.

[37] E.-M. Korek, R. Teotia, D. Herbig, and R. Brederlow, "Electrochemical Impedance Spectroscopy for Ion Sensors with Interdigitated Electrodes: Capacitance Calculations, Equivalent Circuit Models and Design Optimizations," *Biosensors*, vol. 14, no. 5, Art. no. 5, May 2024, doi: 10.3390/bios14050241.

[38] M. S. A. Rahman, S. C. Mukhopadhyay, and P.-L. Yu, *Novel sensors for food inspection: modelling, fabrication and experimentation*. Springer, Springer Nature, 2014. doi: 10.1007/978-3-319-04274-9.

[39] H. S. Magar, R. Y. A. Hassan, and A. Mulchandani, "Electrochemical Impedance Spectroscopy (EIS): Principles, Construction, and Biosensing Applications," *Sensors*, vol. 21, no. 19, p. 6578, Oct. 2021, doi: 10.3390/s21196578.

[40] F. Lisdat and D. Schäfer, "The use of electrochemical impedance spectroscopy for biosensing," *Anal. Bioanal. Chem.*, vol. 391, no. 5, pp. 1555–1567, Jul. 2008, doi: 10.1007/s00216-008-1970-7.

[41] P. A. Anaraki and M. Heidari, "Conductivity Effect on the Capacitance Measurement of a Parallel-Plate Capacitive Sensor System," *Indones. J. Phys.*, vol. 22, no. 4, pp. 107–114, Nov. 2016, doi: 10.5614/itb.ijp.2011.22.4.2.

[42] "Electric Double Layer." Accessed: Oct. 10, 2023. [Online]. Available: https://faculty.kfupm.edu.sa/ME/hussaini/Corrosion%20Engineering/02.05.04.htm

[43] N. E. Tolouei, S. Ghamari, and M. Shavezipur, "Development of circuit models for electrochemical impedance spectroscopy (EIS) responses of interdigitated MEMS biochemical sensors," *J. Electroanal. Chem.*, vol. 878, p. 114598, Dec. 2020, doi: 10.1016/j.jelechem.2020.114598.

[44] A. Guimerà, G. Gabriel, E. Prats-Alfonso, N. Abramova, A. Bratov, and R. Villa, "Effect of surface conductivity on the sensitivity of interdigitated impedimetric sensors and their design considerations," *Sens. Actuators B Chem.*, vol. 207, pp. 1010–1018, Feb. 2015, doi: 10.1016/j.snb.2014.10.134.

[45] J. Wei, "Distributed capacitance of planar electrodes in optic and acoustic surface wave devices," *IEEE J. Quantum Electron.*, vol. 13, no. 4, pp. 152–158, Apr. 1977, doi: 10.1109/JQE.1977.1069319.
[46] D. Mojena-Medina, M. Hubl, M. Bäuscher, J. L. Jorcano, H.-D. Ngo, and P. Acedo, "Real-Time Impedance Monitoring of Epithelial Cultures with Inkjet-Printed Interdigitated-Electrode Sensors," *Sensors*, vol. 20, no. 19, p. 5711, Oct. 2020, doi: 10.3390/s20195711.
[47] D. R. Merrill, M. Bikson, and J. G. R. Jefferys, "Electrical stimulation of excitable tissue: design of efficacious and safe protocols," *J. Neurosci. Methods*, vol. 141, no. 2, pp. 171–198, Feb. 2005, doi: 10.1016/j.jneumeth.2004.10.020.
[48] M. A. Lebedev and M. A. L. Nicolelis, "Brain-machine interfaces: past, present and future," *Trends Neurosci.*, vol. 29, no. 9, pp. 536–546, Sep. 2006, doi: 10.1016/j.tins.2006.07.004.
[49] S. M. Wellman *et al.*, "A Materials Roadmap to Functional Neural Interface Design," *Adv. Funct. Mater.*, vol. 28, no. 12, p. 1701269, Mar. 2018, doi: 10.1002/adfm.201701269.
[50] C. M. Luetje and K. Jackson, "Cochlear implants in children: what constitutes a complication?," *Otolaryngol.--Head Neck Surg. Off. J. Am. Acad. Otolaryngol.-Head Neck Surg.*, vol. 117, no. 3 Pt 1, pp. 243–247, Sep. 1997, doi: 10.1016/s0194-5998(97)70181-5.

Annex

A.1 Comprehensive Guide to FEM Procedures

In this section, we outline a step-by-step procedure for utilizing COMSOL Multiphysics, a FEM method renowned for its capabilities in geometric meshing, modelling, designing, simulating, and analyzing various systems. Here, we employ COMSOL Multiphysics to model and simulate the structure of an IDE, incorporating its geometric parameters through finite element simulations. The IDE 2D layout is first sketched with its dimensions as depicted in Figure A.1. So, once COMSOL Multiphysics is launched, we then create a new 2D model, after which we build the geometry.

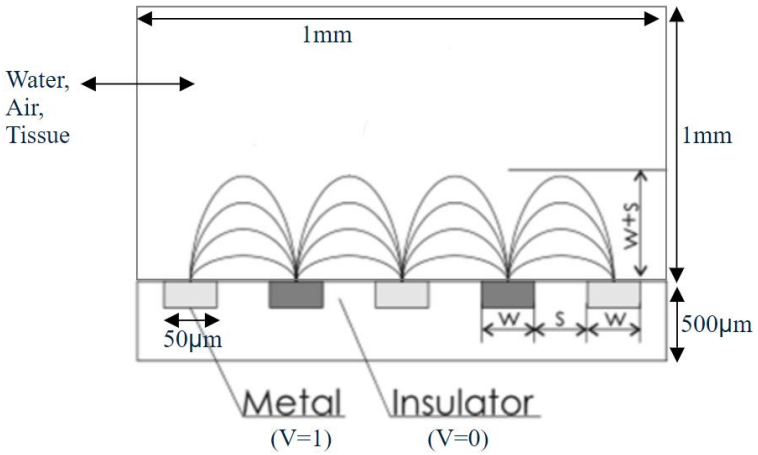

Figure A.1: Cross-section of a planar interdigitated electrode array device [35].

- **Geometry:** The x and y coordinates of the rectangle representing the substrate and infinite boundary, as well as the x and y coordinates of the polygons representing the electrodes are as follows:

  Rectangle1=Infinite boundary: width=90µm, height=1000µm,(position: center)(x=0,y=500µm).

  Rectangle 2=Substrate: width=90µm, height=500µm,(position: center)(x=0,y=-250µm).

  Polygon1=Metal (Electrode): (x,y)=(30,0) and (45,0).

  Polygon2=Insulator (Gnd): (x,y)=(-30,0) and (-45,0).

  Rectangle3=Passivation(with spacing): width=17µm, height=2µm,(position: center)(x=-45µm,y=0).

  Rectangle4=Passivation(with spacing): width=17µm, height=2µm,(position: center)(x=45µm,y=0).

- **Defining Material Properties:** The next step involves selecting the materials from COMSOL library and defining their properties, such as permittivity and conductivity. Table A.1 depicts the permittivity and conductivity of materials derived from literature.

Material	ε_r	σ[S/m]
Air	1	0.0000012μ
DI Water	80	0.055μ
Tap water	80	50μ
Low Saltwater Conc.	69	250μ
High Saltwater Conc.	45	50000μ
PBS 0.01M	80	1.5
SU-8	4	0
Si3N4	7.5	0.000001μ
SiO2	4.5	0.0000000007μ
Diamond	5.7	0.16μ
Quartz(substrate)	4	0.00000001μ

Table A.1: Parameters of materials used in COMSOL simulations.

- **Defining Boundary and Electric currents:** Open boundary conditions like "Electric Insulation" ensure that the current remains confined within the domain, accurately representing the physical scenario without leakage. The top boundary represents an infinite spacing. Typically, this distance should be 10 times the electrode spacing. The "Current Conservation 1" feature ensures that the current is conserved throughout the domain according to Maxwell's equations. "Electric Insulation 1" is applied to surfaces where no current flow is desired, preventing current from leaving the boundaries of the simulation domain. "Initial Values 1" sets the starting conditions for the electric potential and current distribution. The "Electric Potential 1" boundary condition is assigned to one of the polygons, designating it as an electrode with a voltage of 1V, while the "Ground 1" feature sets another polygon to 0V, establishing it as the reference point for the electric potential. Finally, the "Terminal 1" feature is used to define boundaries where electric currents can enter or leave the model. By assigning these conditions, the simulation can accurately model the behavior of the interdigitated electrodes, with one polygon acting as the powered electrode at V=1 and the other as the ground at V=0. This setup allows for the precise calculation of the electric field distribution within the defined geometry. (Except for potential we do not make any other changes in this module.)
- **Meshing:** We select "very fine" meshing as selecting a very fine mesh is crucial for accurately capturing the detailed behavior of the electric field, especially in regions with complex geometries or high gradients, such as around the edges of the interdigitated electrodes.
- **Frequency domain Analysis:** In the settings for the frequency domain study, we specify the range of frequencies for the analysis in order to compute the impedance. This usually involves setting a start frequency, end frequency, and the number of frequency points or the frequency step size. For our simulations Fmin=100Hz,Fmax=40MHz, number of frequency points=47or52, step size=20.

- **Global Evaluation:** We then evaluate the impedance of the IDEs for the total desired pairs of fingers by dividing them by N-1 number of fingers as depicted in Figure A.2, assuming they function as resistors connected in parallel. This evaluation is performed using the Global Evaluation feature. Subsequently, we observe the results using the 2D plots provided in the Results section.

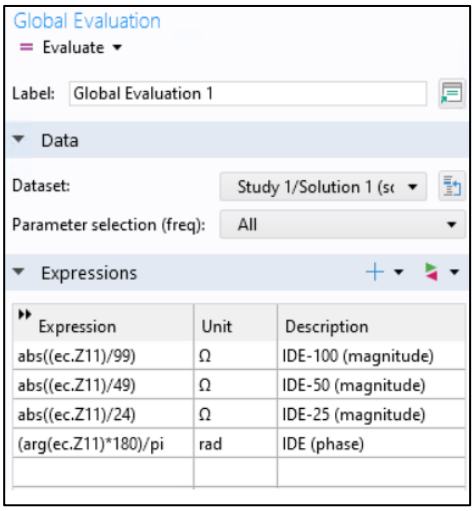

Figure A.2: Simulation modelled for 2 electrodes which is then divided by (N-1) number of fingers to obtain plots for N fingers.